Cholinergic and multiple-circuit mechanisms of hippocampal theta-rhythm generation

Inês Guerreiro

▶ To cite this version:

Inês Guerreiro. Cholinergic and multiple-circuit mechanisms of hippocampal theta-rhythm generation. Neuroscience. Université Paris sciences et lettres, 2021. English. NNT : 2021UPSLE074 . tel-04116901

HAL Id: tel-04116901

https://theses.hal.science/tel-04116901v1

Submitted on 5 Jun 2023

PSL UNIVERSITÉ PARIS

THÈSE DE DOCTORAT

DE L'UNIVERSITÉ PSL

Préparée à École Normale Supérieure

Cholinergic and multiple-circuit mechanisms of hippocampal theta-rhythm generation

Soutenue par

Inês GUERREIRO

Le 9 décembre 2021

École doctorale n°158

Cerveau, cognition, comportement

Spécialité

Neurosciences

Composition du jury :

Dimitri KULLMANN Dr., University College London	*Président du jury*
Laure BUHRY Dr., University of Lorraine	*Rapporteuse*
Michael GRAUPNER Dr., Université Paris Descartes	*Examinateur*
Jerrel YAKEL Dr., NIEHS	*Examinateur*
Zhenglin GU Dr., NIEHS	*Examinateur*
Boris GUTKIN Dr., École normale supérieure	*Directeur de thèse*

ENS | PSL

Preface

This dissertation gathers the work developed throughout my last 4 years as a Ph.D. student at ENS. Many people have crossed paths with me during this time and played an essential part in this journey. I would like to acknowledge them here.

I was fortunate to have a *directeur de thèse* who understands what life in research entails and makes sure his students have the tools they need to have a fulfilling career. I would like to thank Boris Gutkin for entrusting me with such an exciting and challenging research project and for his dedicated support and guidance even (and especially!) during a global pandemic and a total lockdown.

Furthermore, I would like to thank Jerrel Yakel and Zhenglin Gu for guiding me through the mystic world of neurophysiology and for always taking the time to answer my questions. I value our discussions greatly, as well as the time I spent in your laboratory. I extend this acknowledgment to all your team for making me feel so welcome.

I would like to thank the jury members for devoting their time to this project, and Michael Graupner and Karim Benchenane for their insightful feedback and pertinent advice during our yearly thesis committee meetings.

During my degree, I had the chance to work alongside incredible people. I would like to thank my colleagues at the Group of Neural Theory for all the insightful conversations, tea breaks, movie nights, and picnics. Special thanks to Gregory Dumont for his enlightening advice and scientific feedback, and for never acting annoyed when I bothered him even long after he left the lab.

Last but not least, I would like to thank my parents, Fátima and Manuel, my sister, Rita, and Paul, for their unconditional support and for always having my back. I would also like to thank my little niece, Laura, simply for being an unlimited source of joy.

October, 2021

Contents

1 | Introduction

1.1 The hippocampal formation

The hippocampal formation comprises two main structures: the hippocampus and the entorhinal cortex (EC). The hippocampus is organized into subdivisions, namely, the dentate gyrus (DG), the cornu ammonis 3 (CA3), the cornu ammonis 2 (CA2), and the cornu ammonis 1 (CA1). Additionally, each subdivision is divided into layers: stratum oriens (s.o.), stratum pyramidale (s.p.), stratum radiatum (s.r.), and stratum lacunosum-moleculare (s.l.m.). Similarly, the EC presents a laminar organization (layers I, II, III, IV, V, and VI).

The hippocampus and EC are interconnected through the trisynaptic loop. The EC projects to the dentate gyrus via the perforant pathway, granule cells in the dentate gyrus project to CA3 through mossy fibers, and the CA3 pyramidal cells project to CA1 via the Schaffer collateral (SC) pathway. Entorhinal inputs can also reach the hippocampal CA1 field directly through the temporoammonic pathway. Pyramidal cells in CA1 project to the deep layers of the EC, closing the hippocampal-entorhinal loop (see Figure 1.1). This general layout holds across the full range of mammalian species (Li et al., 1994; Amaral and Lavenex, 2007; Amaral and Witter, 1989).

The hippocampal formation receives a vast amount of highly processed sensory information from neocortical areas that converge into the hippocampal formation mainly through the EC. The exchange of information between the hippocampal formation and other cortical areas is fundamental for memory consolidation processes. Based on such extrinsic connectivity, the hippocampal formation exerts control over widespread regions, and it occupies a privileged position to coordinate the activity

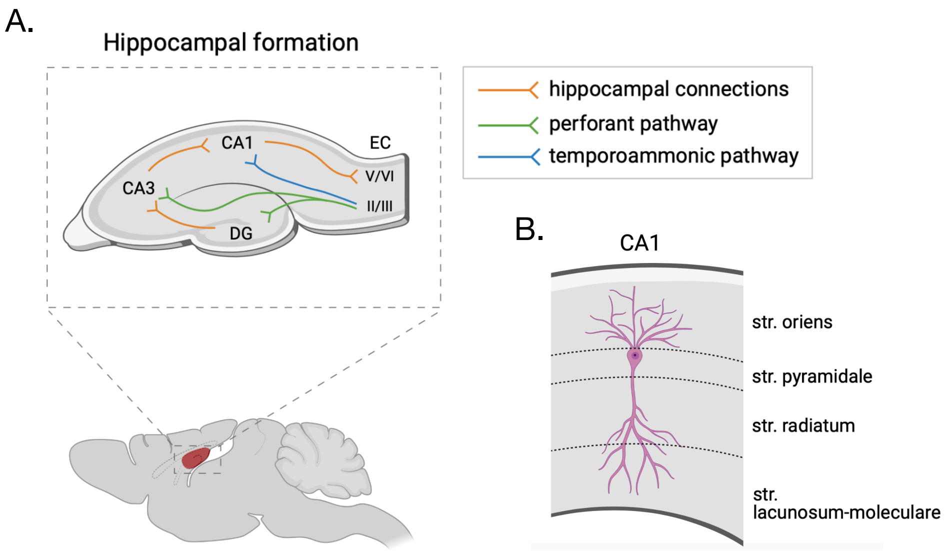

Figure 1.1: Simplified diagram of the hippocampal formation (A) Wiring diagram of the hippocampus and entorhinal cortex. **(B)** Laminar structure of the CA1 region.

of the different brain regions.

1.1.1 Hippocampus: structure and organization

As previously mentioned, the hippocampus is divided into different fields with distinct morphological, anatomical, and cellular profiles. The CA3 region comprises a homogeneous population of pyramidal cells that form extensive recurrent connections with each other, allowing it to function as an auto-associative network (Marr, 1971; McNaughton and Morris, 1987; Treves and Rolls, 1991). CA1 pyramidal cells form remarkably less recurrent connections and are uniformly distributed with the cell body at the pyramidale layer. The CA1 area also comprises populations of highly diverse GABAergic interneurons that form a complex neural network and control the activity of CA1 pyramidal cells by feedback or feedforward inhibition (Knowles and Schwartzkroin, 1981).

The EC is considered the main extrinsic source of excitatory inputs of the CA1 region. The two regions form a closed loop, with entorhinal layer III neurons projecting to the CA1 and pyramidal CA1 neurons targetting entorhinal layer V/VI pyramidal cells. Additionally, CA1 neurons receive substantial cholinergic and GABAergic inputs from the medial septum (MS) [1].

CA1 circuits are fundamental for processes of memory formation (Bartsch et al., 2010), and impairment of CA1 neurons contribute to memory deficits in patients with damages to the hippocampus (Kadar et al., 1998).

CA1 GABAergic interneurons Despite representing only $10-15\%$ of the total hippocampal neural population (Pelkey et al., 2017), the interneurons form a complex local network recurrently connected and target the excitatory pyramidal cells at different dendritic compartments. Thus, they play a crucial role in regulating the activity of pyramidal cells and the excitability of the hippocampal network.

Hippocampal GABAergic interneurons can generally be classified based on morphology, neurochemical markers, or physiological features. Morphologically, hippocampal interneurons are classified by relating their somatodendritic location to the layer specificity of synaptic input and the axonal projections to the postsynaptic target domain. For example, oriens-lacunosum moleculare (OLM) cells refer to interneurons whose soma is on the s.o. layer and whose axons extend to s.l.m.; bistratified interneurons have dendrites and axons that ramify within the s.o. and s.r. layers emerging from the cell body on s.p. (Booker and Vida, 2018). Regarding neurochemical markers, interneurons can be parvalbumin (PV+), somatostatin (SOM+), cholecystokinin (CCK+), or vasointestinal peptide (VIP+) expressing interneurons. Lastly, hippocampal interneurons can have fast-spiking dynamics or present slower dynamics with low-frequency subthreshold oscillations. Please note that this is not an extensive list of all the interneuron types that form the hippocampal network. For example, in the CA1 area of the hippocampus, 21 classes of GABAergic interneurons have been identified to date (Freund and Buzsáki, 1996; Klausberger and Somogyi, 2008; Bezaire and Soltesz, 2013), and this is likely to be an underestimation.

It is unclear whether the current classification methods are adequate, as one GABAergic interneuron often spans different categories. For example, both OLM

---

[1] Connections between septal and CA3 neurons also exist (Amaral and Kurz, 1985), but they go beyond the scope of this project

interneurons with intrinsic low-frequency spiking dynamics and fast-spiking bistratified cells express somatostatin immunoreactivity (Booker and Vida, 2018; Müller and Remy, 2014). It is then challenging to dissect the functional properties of the different interneurons that form the hippocampal microcircuits.

Cholinergic signaling in the hippocampus Cholinergic receptors can be found in hippocampal pyramidal and GABAergic interneurons and can be located pre- or postsynaptically. To complicate matters further, there are various cholinergic receptor subtypes with distinct physiological profiles and dynamics that can modulate the hippocampal circuitry in specific ways.

There are two main classes of cholinergic receptors: muscarinic (mAChR) and nicotinic (nAChR) receptors.

Muscarinic receptors are metabotropic receptors responsive to ACh and muscarine. They act through second messengers and are indirectly linked with ion channels. There are five subtypes (M1-M5) expressed across the CNS. In the hippocampus, M1 and M3 receptors are mainly expressed in principal neurons, while M2 and M4 are present on interneurons (Volpicelli and Levey, 2004). They have been shown to regulate ionic conductances and mobilize calcium (Lanzafame et al., 2003).

Nicotinic receptors are ionotropic channels responsive to ACh and nicotine, consisting of five subunits arranged symmetrically around a pore. Each subunit of hippocampal nAChR can be of type $\alpha2$-$\alpha7$ and $\beta2$-$\beta4$. The combination of subunits that composes the nAChR determines the dynamical and physiological properties of the receptor channel. Notably, while all nAChR subtypes are permeable to Na^+ and K^+, they differ in their permeability to calcium, with the homomeric $\alpha7$ nAChR having the highest calcium permeability (Castro and Albuquerque, 1995).

The $\alpha7$ nAChR is one of the most abundant cholinergic receptors in the hippocampus. They have been subject of great interest as their dysfunction is believed to be at the origin of cognitive deficits and neurodegenerative diseases such as Alzheimer's disease (Guan et al., 2001; Wang et al., 2000). In addition, their high calcium permeability makes them potentially involved in synaptic plasticity (Ji et al., 2001; Gu and Yakel, 2011) and neurotransmitter release mechanisms (Wanaverbecq et al., 2007; Sharma and Vijayaraghavan, 2003, 2001). Another important feature of $\alpha7$ nAChRs is their rapid desensitization. Desensitization is a mechanism where prolonged exposure to the receptor's agnostic drives it into a refractory state where there is no ion flux. It impacts their response to repetitive inputs, but their functional role in generating and maintaining hippocampal rhythms is still unclear. Notably, even though currents mediated by $\alpha7$ nAChRs decline strikingly during activation at theta frequency (Buhler and Dunwiddie, 2001), knockout of these receptors *in vivo* disrupts hippocampal theta oscillations (Gu and Yakel, 2017).

1.1.2 Entorhinal Cortex local circuit

The entorhinal cortex is commonly perceived as the nodal point of cortico-hippocampal circuits. Neurons in the superficial layers (II/III) receive most of their input from cortical areas and constitute a major excitatory input to the hippocampus; neurons in the deep layers receive extensive input from the hippocampus and project to the EC superficial layers (Amaral and Lavenex, 2007).

The EC comprises a mixture of excitatory pyramidal cells, PV+ interneurons, and stellate cells distributed among the different layers. The superficial layers are mainly made up of densely packed excitatory stellate and pyramidal cells. The stellate cells are the most abundant cell type on these layers, and they provide the primary entorhinal excitatory input to the hippocampal region. One of their most striking features is their ability to generate rhythmic subthreshold oscillations (Alonso and Klink, 1993). Connections between stellate cells have rarely been found, and they are believed to communicate with each other through PV+ fast-spiking interneurons that can be found in the same layers (Witter et al., 2017). The deep layers comprise a heterogeneous population of excitatory pyramidal cells with axon collaterals terminating both on the deep and superficial layers of the EC. On the superficial layer, they target mainly pyramidal cells on layer III, generating prolonged excitatory responses. (Hamam et al., 2000; Witter et al., 2017; Canto et al., 2008).

There is a rapidly growing interest in understanding the functional properties of the EC. This is primarily motivated by studies demonstrating that some aspects of memory impairment can be attributed to damage of the EC (Davis et al., 2001; Buckmaster et al., 2004a), and that stellate and pyramidal cells in this brain region act as grid cells, i.e., they represent equally spaced locations in an environment via their firing rates (Tang et al., 2014; Moser et al., 2008).

1.2 Synaptic plasticity

Synaptic plasticity is defined as the ability of neurons to change the strength of the synapses in a neural network (Konorski, 1948; Hebb, 1949). It is considered to be the cellular process underlying learning and storage of information in the hippocampus (Riedel et al., 1999). It implies alterations in the pre-and/or postsynaptic neurons, and it can be expressed as changes in the probability of neurotransmitter release from the presynaptic neuron or in the number and sensitivity of postsynaptic receptors.

Since long-term potentiation (Bliss and Lømo, 1973) and depression (Dudek and Bear, 1991) were first induced in the hippocampus, this remained the region of choice to study the mechanisms of synaptic plasticity, with the CA1 area being the most extensively studied model of activity-dependent plasticity in the mammalian brain. To this day, the SC-CA1 synapse continues to be widely used as a model synapse for the study of LTP and synaptic plasticity in general.

In hippocampal excitatory synapses, long-term synaptic potentiation typically involves a calcium flux mediated by NMDARs (Dudek and Bear, 1991; Lüscher and Malenka, 2012; Cummings et al., 1996; Bear and Malenka, 1994). NMDAR is a ligand of glutamate, highly permeable to calcium. At the resting potential, extracellular Mg^{2+} binds to specific sites of the NMDARs blocking the passage of ions. Postsynaptic depolarization relieves this block allowing calcium (and Na^{+}) to enter the cell. Depolarization of the postsynaptic membrane is typically induced through activation of AMPAR co-localized on the dendritic spine (Lüscher and Malenka, 2012; Collingridge et al., 1983; Muller et al., 1992; Tsien et al., 1996). An elevation of the intracellular calcium concentration mediated by postsynaptic NMDAR can activate protein kinases such as Ca^{2+}/calmodulin-dependent protein kinase II (CaMKII), which ultimately leads to changes in the density of AMPAR on the postsynaptic terminal (Asztely et al., 1992; Kullmann, 1994; Mainen et al., 1998; Perkel et al., 1993; Barria et al., 1997). The calcium response determines the polarity of synaptic modification. Typically, a moderate increase in intracellular concentrations induces LTD while a substantial elevation of intracellular calcium induces LTP (Cummings et al., 1996; Lisman, 1989; Artola and Singer, 1993; Bear and Malenka, 1994).

The depolarization of the postsynaptic membrane is a critical step in the induction of NMDAR-dependent plasticity. Thus, it is not surprising that GABAergic circuits can modulate hippocampal plasticity at excitatory synapses through feed-forward or feedback inhibition. Similarly, activating cholinergic receptors on glutamatergic or GABAergic neurons, located pre or postsynaptically, can regulate the induction of potentiation (or depression) in the hippocampal region.

GABAergic modulation It is firmly established that inhibitory inputs modulate local hippocampal synaptic plasticity (Wigström and Gustafsson, 1983; Meredith et al., 2003; Ormond and Woodin, 2009; Yang et al., 2016). Moreover, selective activation of certain interneuron classes can mediate the induction of plasticity in distinct ways. For example, activation of OLMα2 interneurons facilitates potentiation of SC inputs into proximal dendrites while inhibiting EC inputs into distal dendrites of the CA1 pyramidal neuron (R.Leão et al., 2012), and high-frequency bursts acting on GABAergic interneurons containing $GABA_B$ autoreceptors permits the induction of LTP on the SC-CA1 synapse (Davies et al., 1991).

The different pathways and mechanisms through which GABAergic interneurons modulate plasticity remain elusive despite all the experimental efforts.

Cholinergic modulation Due to the abundance of cholinergic receptors and the complexity of the neural networks in which they are embedded, it is difficult to access the mechanisms through which cholinergic inputs regulate hippocampal activity and synaptic plasticity. The effects of ACh vary depending on which type of cholinergic receptor and neuron is being activated. For example, presynaptic mAChRs can decrease neurotransmitter release reducing synaptic strength (Valentino and Dingledine, 1981; Raiteri et al., 1984), while postsynaptic mAChRs enhance responses of NMDA receptors (Markram and Segal, 1992) and inhibit calcium-activated K^+ currents inducing the opposite effect (Cole and Nicoll, 1983). Presynaptic activation of α7 nAChR enhances synaptic transmission (Radcliffe and Dani, 1998), and postsynaptic α7 nAChRs facilitate LTP at hippocampal excitatory synapses by producing calcium signals that contribute to the induction of LTP (Vernino et al., 1992, 1994; Rathouz et al., 1996; Shoop et al., 2001; Berg and Conroy, 2002). In addition, studies also show that the timing of cholinergic inputs is important in modulating SC-evoked responses (Ji et al., 2001; Gu and Yakel, 2011).

1.2.1 Mechanistic models of calcium-dependent synaptic plasticity

There is a large variety of heuristic models of synaptic plasticity focusing on the timing of inputs (Dan and Poo, 2004; Gerstner et al., 1996; Appleby and Elliott, 2005; Badoual et al., 2006; Bi and Wang, 2002; Burkitt et al., 2007), the correlations in the pre and postsynaptic activity (Hebb, 1949; Kempter et al., 1999; Lisman, 1989) and reflecting the modulatory role of neuromodulators (Ang et al., 2021; Pedrosa and Clopath, 2017; Maki-Marttunen et al., 2020). In this thesis, we focus on mechanistic models, which we review briefly in this section.

Many computational models have been developed to understand the mechanisms of synaptic plasticity. In particular, there are abundant models that focus on the role of calcium signaling, either by detailing the calcium processes of CaMKII phosphorylation and consequent changes in AMPAR density or by directly modeling changes in synaptic efficiency as a function of intracellular calcium concentration. (Lisman, 1989; Holmes and Levy, 1990; Lisman and Zhabotinsky, 2001; Shouval et al., 2002; Abarbanel et al., 2003; Graupner and Brunel, 2012, 2005a; Inglebert et al., 2020).

According to the model developed by Shouval et al. (2002), changes in the synaptic strength of a synapse j, W_j, can be formulated as

$$\frac{dW_j}{dt} = \eta([Ca]_j)(\Omega([Ca]_j) - \lambda W_j) \tag{1.1}$$

where η is a calcium-dependent learning rate, Ω is a function that describes changes in synaptic efficacy induced by calcium, and λ represents a decay constant that stabilizes synaptic growth. A calcium-dependent learning rate η avoids unwanted oscillations in the synaptic weights, while a function Ω accounts for the fact that different levels of intracellular calcium trigger various forms of plasticity (see Figure 1.2).

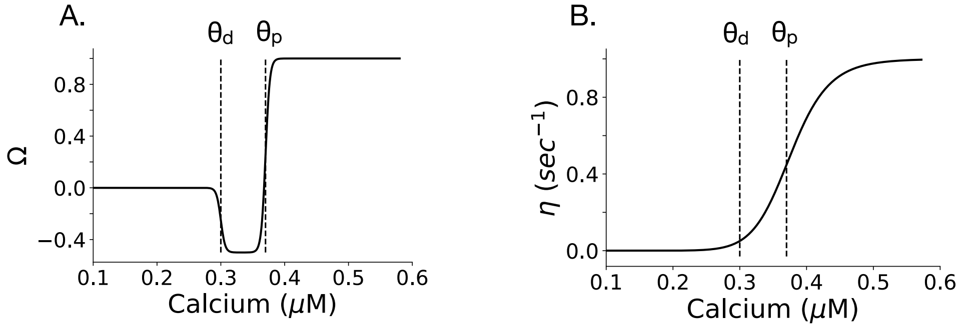

Figure 1.2: Calcium-dependent plasticity functions from Shouval et al. (2002). (A) Synaptic efficacy funtion Ω. When the calcium concentration is bellow a depression threshold Θ_d, Ω remains at its base line value; when calcium is above Θ_d and bellow a potentiation threshold Θ_p ($\Theta_d < Calcium < \Theta_p$) the synaptic weight is reduced; when calcium is above Θ_p, the synaptic weight increases. **(B)** Synaptic plasticity learning rate function η as a function of calcium. Figures reproduced from Shouval et al. (2002)

The model assumes that the primary source of calcium are the postsynaptic NMDAR. The calcium dynamics is then described as follows:

$$\frac{d[Ca]_j}{dt} = I_{NMDA} - \frac{[Ca]_j}{\tau_{Ca}} \tag{1.2}$$

where τ_{Ca} is the calcium's time constant and I_{NMDA} is the current through the NMDAR. The NMDA current is generally described as

$$I_{NMDA} = G_{NMDA} B(V)(V - E_r) \tag{1.3}$$

where G_{NMDA} is the channel's conductance, E_r the reversal potential, and $B(V)(= 1/(1 + exp(-0.062V)\frac{[Mg^{2+}]}{3.57}))$ is a voltage-dependent term that accounts for the presence of a Mg^{2+} block when the cell is hyperpolarized. Please note that although in the original model of Shouval and colleagues, it is considered that calcium ions transport all the current through the NMDAR, that it is not accurate, and the NMDAR are also permeable to other ions such as Na^+. This imprecision can easily be corrected by including a parameter α that accounts the percentage of total current that is carried out by calcium ions ($\frac{d[Ca]_j}{dt} = \alpha I_{NMDA} - \frac{[Ca]_j}{\tau_{Ca}}$).

Following the work of Shouval et al. (2002), Graupner and Brunel (2012) devised a simplified calcium-based model that provides a link between stimulation protocols and evoked synaptic changes, and can reproduce different STDP curves as seen experimentally.

In this thesis, we use the calcium-based model developed by Shouval et al. (2002) to describe changes in the synaptic strength of the SC-CA1 synapse. The model is simple enough to be implemented computationally and to reproduce the experimental results on which we base our modeling work, such as the absence of bistability.

1.3 Hippocampal theta rhythm

The hippocampal theta rhythm consists of an oscillatory pattern with a 4-12 Hz frequency observed in the hippocampal formation and associated structures during active exploration, REM sleep, states of alert immobility, and under anesthesia. Experiments suggest a close relation between hippocampal theta rhythms and learning and memory. Several studies show that the extent to which theta is present in an electroencephalogram is indicative of how quickly animals learn a task of how well they remember (Landfield et al., 1972; Winson, 1978; Berry and Thompson, 1978). While several studies suggest that theta is required for the formation of memories represented by neuronal ensembles (Wang et al., 2015; Skaggs et al., 1996; Dragoi and Buzsaki, 2006; Foster and Wilson, 2007; Feng et al., 2015; Gupta et al., 2012), its role in the formation of memory representations at the single cells level remains unclear. A study shows that place fields are formed by hippocampal place cells of rats when the animal is in a new environment, despite the blockade of theta rhythm and theta entrainment (Brandon et al., 2014). Such observation suggests that theta rhythmicity is not required to form spatial memory representations at the single cell level. On the other hand, there is compelling evidence that theta and synaptic plasticity, a cellular mechanism of information storage, are strongly correlated (Larson et al., 1986; Orr et al., 2001; Hyman et al., 2003; Griffin et al., 2004).

According to their frequency, physiology, and behavioral correlations, the hippocampal theta rhythm can be classified into type 1 or type 2 (Kramis et al., 1975). Type 1 theta (8-12 Hz) occurs during active motor behaviors and REM sleep. It is considered to be atropine resistant, despite studies suggesting that it may have an atropine-sensitive and an atropine-resistant component (Kramis et al., 1975; Vanderwolf and Baker, 1986). Type 2 (4-7 Hz) occurs during states of still alertness and urethane anesthesia. It is abolished by the administration of atropine, and it is therefore considered to be atropine-sensitive (Lee et al., 1994; Vanderwolf and Baker, 1986).

1.3.1 Mechanisms of theta rhtyhm

Neural oscillations can arise on two levels of organization. On the cellular level, it can appear as oscillations in the membrane potential or persistent rhythm action potentials. On the network level, the synchronized activity of large numbers of neurons can give rise to macroscopic oscillations with a well-defined frequency. It is essential to understand the mechanisms through which oscillations are generated and maintained on the different scales as they are most likely complementary.

Some neurons in the hippocampal formation are endowed with intrinsic properties that give rise to slow subthreshold oscillations and resonate at theta frequency. This is the case of OLM interneurons in the hippocampus (Zemankovics et al., 2010), and stellate cells in the EC (Alonso and Klink, 1993). Even though these cells have been implicated in the generation of theta in local hippocampal circuits, their role is still a topic of discussion (Dickson et al., 2000; Kispersky et al., 2012; Fernandez et al., 2013; Wang, 2002; Moser et al., 2008; Rowland et al., 2018; Rotstein et al., 2005a).

On the network level, two brain regions known to be essential to the generation of hippocampal theta rhythm are the medial septum and the entorhinal cortex.

The medial septum The medial septum is composed of cholinergic, GABAergic, and glutamatergic cells, and it mainly targets the hippocampal formation. It is regarded as a crucial brain structure for the generation and maintenance of hippocampal theta activity, a notion that has been corroborated by experimental observations that lesions or inactivation of the medial septum disrupts (or even abolishes) hippocampal theta oscillations (Petsche et al., 1962; Gogolák et al., 1968; Green and Arduini, 1954; Mizumori et al., 1990).

Cholinergic neurons modulate the excitability of hippocampal neurons in a way that promotes theta rhythm, likely through the activation of mAChR on CA1 pyramidal neurons and activation of $\alpha 7$ nAChR on GABAergic interneurons that can inhibit or disinhibition hippocampal pyramidal cells (Gu et al., 2017, 2020). The role of the septal GABAergic neurons is still a topic of discussion. Despite presenting rhythmic activity, there is no direct evidence that they are directly pacing the hippocampal rhythm (Stewart and Fox, 1990; Yoder and Pang, 2005; Gogolák et al., 1968; King et al., 1998).

The entorhinal cortex Even though theta oscillations can be observed in an *in vitro* preparation of the isolated hippocampus (Goutagny et al., 2009), lesions of the EC lead to disruptions of the hippocampal theta rhythm and spatial learning (Chenani et al., 2019; Davis et al., 2001; Buzsáki et al., 1983). Moreover, administration of AMPAR antagonist to the EC in a septo-entorhinal-hippocampal co-culture preparation blocked theta expression in the entire hippocampal formation (Gu and Yakel, 2017). However, it is important to note that the EC may contribute differently to the generation and expression of the two subtypes of theta rhythm (type 1 and type 2) since lesions to the EC abolish type 1 theta while type 2 oscillations remain. Still, lesions to the EC disrupt the behavioral correlates of both types of theta, suggesting that the EC is an integral part of both systems (Montoya and Sainsbury, 1985).

Recent experimental work indicates that the role of EC may go beyond simply responding to external rhythmic inputs and coordinating the activity of the hippocampal regions. Instead, it may be where the theta rhythm is being generated (Gu and Yakel, 2017). Hippocampal excitatory inputs and NMDAR in the EC seem to be two essential components for the generation of theta in EC, but its mechanisms remain elusive (Gu and Yakel, 2017; Gu et al., 2017; Nuñez and Buño, 2021).

1.3.2 Modeling hippocampal theta oscillations

Theoretical and mathematical models are convenient tools for understanding brain circuitry's functional properties and studying the emergence of neural phenomenons on different scales. They rely on experimental data to construct biological approximations and shape their output. Due to the difficulty of recording simultaneously from the septum, hippocampus, and entorhinal cortex, most of the experimental data collected to date focus on the septal-hippocampal network, hippocampal-entorhinal network, or the isolated hippocampus. This is reflected in the models of theta rhythm.

Models that study the interaction between septum and hippocampus often consider the septum to be the pacemaker in the production of hippocampal theta rhythm, with rhythmic cholinergic and GABAergic septal neurons imposing the theta rhythm on the hippocampal neurons and coordinating their activity, in particular on hippocampal GABAergic interneurons (Stewart and Fox, 1990; Denham and Borisyuk, 2000). However, recordings from the medial septum indicate that the theta-locked cells of the region do not fire with a common phase, which is inconsistent with the pacemaker hypothesis (King et al., 1998).

Concerning the role of EC in the generation of theta rhythm, models suggest that rhythmic hippocampal inputs can initiate theta activity in the EC by driving a population of inhibitory interneurons that in turn coordinates the activity of stellate cells (Neru and Assisi, 2021). Recent experimental evidence suggests that EC is not simply responding to external rhythmic inputs, namely from the hippocampus, but it is where the theta oscillations are being generated (Gu and Yakel, 2017; Mitchell and Ranck Jr., 1980), in particular during the exploration of novel environments (López-Madrona and Canals, 2021). However, computational models addressing the origins of theta in the intrinsic circuit of the EC are still lacking.

Whereas theta rhythms are traditionally thought to be imposed extrinsically, the hippocampus contains intrinsic mechanisms that may actively contribute to the rhythm through the resonance of external inputs or as a local phenomenon. Moreover, the hippocampus contains neurons with slow synapses and intrinsic spiking dynamics in the theta range, such as the OLM interneurons, which may contribute to the generation of theta (White et al., 2000; Rotstein et al., 2005b; Kopell et al., 2010). Despite this, there is evidence that the CA1 region can autonomously generate theta oscillations by using mainly a network of pyramidal cells and PV+ interneurons. More specifically, models suggest that spike frequency adaptation and post inhibitory rebound provide the necessary conditions for rhythmic activity to arise in a minimally connected network of CA1 pyramidal cells with fast-spiking PV+ interneurons, where the pyramidal controls the frequency to PV+ neuron connections. (Goutagny et al., 2009; Bezaire et al., 2016; Ferguson et al., 2017). In this scenario, OLM cells regulate the robustness of hippocampal theta rhythms, without affecting their frequency and power (Chatzikalymniou and Skinner, 2018).

1.4 Outline of the work

This thesis investigates the cholinergic and circuit mechanisms underlying the generation of theta rhythm in a septal-entorhinal-hippocampal circuit. We use a quantitative data-based modeling approach based on a unique experimental setup (a septal-entorhinal-hippocampal *in vitro* co-culture preparation) developed by Zhenglin Gu and Jerrel Yakel at the National Institute for Environmental Health Sciences (NIEHS), USA.

The dissertation is divided into two parts:

I. In the first part of this dissertation, we derive a biophysical model of cholinergic induced hippocampal plasticity.

Experimental studies show that the induction of theta in a septal-entorhinal-hippocampal *in vitro* preparation depends on the co-activation of the septal cholinergic and SC pathways. Moreover, repeated co-activation of the two pathways potentiates the EPSCs of CA1 pyramidal cells and facilitates the expression of the theta rhythm, which can then be readily generated through SC stimulation alone (Gu and Yakel, 2017). We show that cholinergic activation of $\alpha7$ nAChR on OLM$\alpha2$ interneurons can disinhibit CA1 pyramidal cells by inhibiting a class of fast-spiking interneurons targetting CA1 pyramidal cells. Repeated disinhibition paired with SC stimulation can upregulate the conductance of AMPA receptors and potentiate the SC-CA1 excitatory synapse.

II. The second part focuses on the entorhinal and hippocampal network properties that permit theta oscillations to arise and propagate in the circuit. We start by deriving an exact mean-field model reduction that we use to describe the macroscopic activity of the entorhinal and hippocampal networks. Next, we examine how increased hippocampal excitatory inputs - a consequence of the increased hippocampal excitability described in part I - can drive the entorhinal network into an oscillatory regime with theta frequency. Finally, we study the response of the hippocampal network to external rhythmic theta inputs before and after hippocampal plasticity is induced.

Part I

Hippocampal synaptic plasticity

2 | Recurrent cholinergic inputs induce local hippocampal plasticity through feedforward disinhibition

2.1 Introduction

The hippocampal networks are characterized by a variety of locally connected GABAergic interneurons exerting robust control on network excitability. Previous work has detailed the importance of inhibitory inputs in modulating local hippocampal synaptic plasticity (Saudargiene and Graham, 2015; Chevaleyre and Piskorowski, 2014; Wigström and Gustafsson, 1983; Meredith et al., 2003; Ruiz et al., 2010). Furthermore, several experimental studies show that disinhibition facilitates the induction of LTP at excitatory synapses (Ormond and Woodin, 2009; Yang et al., 2016). However, how the disinhibition controlling hippocampal excitatory synapses is modulated (e.g., by neuromodulators) is not clearly understood, and the precise circuitry and dynamics underlying this type of plasticity remain an open question.

GABAergic interneurons receive significant cholinergic innervation from the medial septum. They are endowed with various subtypes of nicotinic acetylcholine receptors (nAChRs) that regulate excitability, plasticity, and cognitive functions (Griguoli and Cherubini, 2012; Levin, 2002; Yakel, 2012). Moreover, alterations of cholinergic action on hippocampal GABAergic interneurons have been implicated in cognitive dysfunction in Alzheimer's disease (AD) (Schmid et al., 2016). These studies, among others, furnish clear evidence that cholinergic inputs exert a powerful role in regulating hippocampal activity. Still, due to the abundance of cholinergic receptors (both muscarinic and nicotinic) and the complexity of the networks in which they are embedded, it is difficult to access the exact mechanisms through which cholinergic action on the hippocampus modulates its microcircuits. Previous studies showed that activation of OLMα2 interneurons increases SC to CA1 transmission and suggest that this happens through disinhibition by reducing the activity of stratum radiatum (s.r.) interneurons that in turn provide feedforward inhibition onto pyramidal neurons (R.Leão et al., 2012). Consistent with these studies, Gu and colleagues found that activation of OLMα2 interneurons increased SC to CA1 EPSCs and reduced IPSCs (Gu et al., 2020). However, the mechanisms through which the activation of the inhibitory interneurons OLMα2 regulates the activity of inhibitory interneurons targeting the CA1 pyramidal cell, and how this facilitates the potentiation of SC-evoked EPSPs of the CA1 pyramidal cells remain elusive.

In this chapter, we use a minimal biophysical circuit model, driven quantitatively by *in vitro* data, to show how modulation of OLM cells influences the activity of fast-spiking interneurons whose GABAergic inputs are co-localized with the SC glutamatergic synapses onto a CA1 pyramidal cell dendrite, and how this promotes the induction of plasticity at the SC-CA1 synapse. We seek to determine how cholinergic activation of the OLM cells through postsynaptic α7 nAChRs can down-regulate the GABAergic signaling onto the pyramidal cells, and how recurrent decreased inhibitory inputs can directly induce the plasticity of the excitatory SC-CA1 synapse. We constructed a minimal circuit consisting of a single compartment spiking model of an OLM interneuron with α7 nAChRs, a fast-spiking interneuron with AMPA, and $GABA_A$ receptors, and a pyramidal cell dendritic compartment with AMPA, NMDA, and $GABA_A$ receptors. They are connected as schematically shown in Figure 2.1.

Overwhelming evidence suggests that most types of LTP involve calcium influx through NMDARs and subsequent changes in the properties of postsynaptic AMPARs, namely changes in their number and phosphorylation state (Barria et al., 1997; Collingridge et al., 1983; Lüscher and Malenka, 2012). To reflect these mechanisms, we employ the calcium-based synaptic plasticity model (proposed by Shouval et al. (2002)) to model synaptic plasticity of the SC-CA1 excitatory synapse.

We use a combination of experiments with computational modeling to put together a coherent picture of the multiple mechanisms through which concurrent disinhibition directly induces local SC-CA1 plasticity. More specifically, we show how repeated concurrent disinhibition induces LTP by mediating AMPAR trafficking. Our modeling results also put together all the pieces of the puzzle to lay out how nAChR cholinergic action on OLM interneurons, working through calcium-dependent regulation of GABA neurotransmission, can downregulate the GABAergic signaling onto CA1 pyramidal cells and induce potentiation of the SC-CA1 synapse.

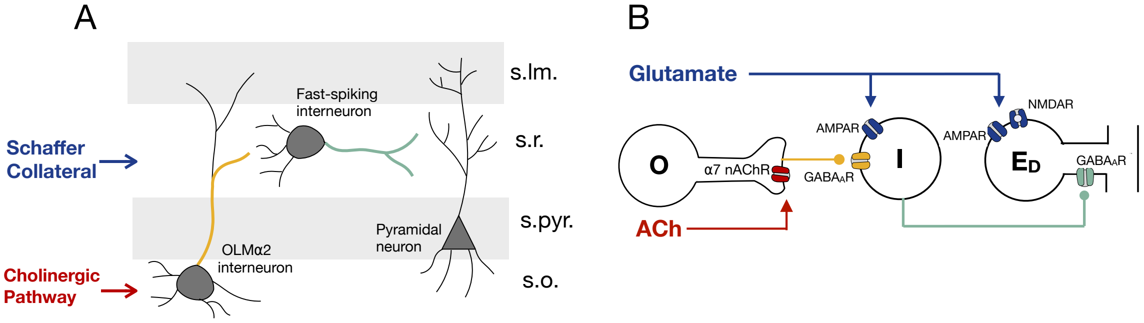

Figure 2.1: Disynaptic disinhibition circuit for nAChR-modulated long-term plasticity in the CA1. **(A)** Simplified wiring diagram of an interneuron network that mediates feedforward inhibition in the CA1 region of the hippocampus. Activating the Schaffer Collateral (SC) pathway leads to the activation of CA1 pyramidal cell dendrites and stratum radiatum (s.r.) interneurons, which provide feedforward inhibition onto the pyramidal cell. Cholinergic activation of OLM$\alpha 2$ interneurons in stratum oriens (s.o.) leads to the inhibition of the s.r. interneurons, counteracting SC feedforward inhibition (R.Leão et al., 2012). **(B)** Minimal network to investigate plasticity induced by the pairing of cholinergic and SC activation. Glutamate activates postsynaptic AMPA and NMDARs at the pyramidal cell dendritic compartment E_D and postsynaptic AMPARs at I-cells, providing feedforward inhibition onto E_D by activating postsynaptic $GABA_A$Rs. Cholinergic inputs act on postsynaptic $\alpha 7$ nAChRs of O-cells, which results in GABA release of the O-cells that it is going to bind to postsynaptic $GABA_A$Rs of the I-cell

2.2 Methods

2.2.1 Animals and materials

All procedures related to the use of mice followed protocols approved by the Institutional Animal Care and Use Committees of the NIEHS. ChAT-cre mice (B6;129S6-Chattm2(cre)Lowl/J), Sst-cre mice (Ssttm2.1(cre)Zjh), and floxed $\alpha7$ nAChR knockout mice (B6(Cg)-Chrna7tm1.1Ehs/YakelJ) were originally purchased from Jackson Laboratory and then bred at NIEHS. OLM 2-cre mice (Tg(Chrna2cre)OE29Gsat/Mmucd) were originally obtained from Mutant Mouse Resource and Research Centers (MMRRC) and then bred at NIEHS. Mice (of either sex) were used for slice culture from day 6 to 8. Culture media were from Sigma and Invitrogen. AAV serotype 9 helper plasmid was obtained from James Wilson at the University of Pennsylvania. The AAV vector containing floxed ChR2 (Addgene #20297) and floxed eNpHR (Addgene #26966) were obtained from Karl Deisseroth (Witten et al., 2010; Gradinaru et al., 2010). AAV viruses were packaged with serotype 9 helper at the Viral Vector Core facility at NIEHS.

2.2.2 Brain slice culture and AAV virus infection

To study the effects of cholinergic co-activation on the plasticity of SC to CA1 synapses in Figure 2.2, coronal septal slices (350 μm) from ChAT-cre mice and horizontal hippocampal slices from floxed $\alpha7$ nAChR mice or OLM$\alpha2$-cre/floxed $\alpha7$ nAChR mice (350 μm) were cut with Leica VT1000S vibratome. Medial septal tissue containing cholinergic neurons was then dissected out and placed next to the hippocampus on a 6-well polyester Transwell insert (Corning) and cultured there for about 2 weeks before being used for experiments, similar as described in Gu and Yakel (2017). AAV viruses containing double floxed ChR2 construct (5 nl) were microinjected to the septal tissue with a micro injector (Drummond Scientific) on the second day of culture. To study the effects of disinhibition on the plasticity of SC to CA1 synapses in Figure 2.4, horizontal hippocampal slices from Sst-cre mice were cultured and AAV viruses containing double floxed eNpHR construct were microinjected to the hippocampus the next day.

2.2.3 Whole-cell patch-clamp recordings

SC to CA1 excitatory postsynaptic currents (EPSCs) were recorded from hippocampal CA1 pyramidal neurons under whole-cell patch-clamp, similar as described in Gu and Yakel (2017, 2011). Briefly, 2-3 weeks after culturing, the slices were removed from transwell inserts and put into a submerged chamber, continuously perfused with 95%O_2/5%CO_2 balanced ACSF (in mM, 122 NaCl, 2.5 KCl, 2 $MgCl_2$, 2 $CaCl_2$, 1.2 NaH_2PO_4, 25 $NaHCO_3$, 25 glucose) at room temperature. EPSCs were recorded at -60 mV under voltage clamp through a glass pipette filled with an internal solution (in mM, 130 potassium gluconate, 2 $MgCl_2$, 3 MgATP, 0.3 Na_2GTP, 10 KCl, 10 HEPES, and 1 EGTA, with pH 7.2-7.3 and osmolarity 280-290 mOsm). Whole-cell patch-clamp recordings were performed with Multiclamp 700B amplifier (Axon Instruments). Data were digitized with Digidata 1550, collected with Clampex. The amplitudes of EPSCs were analyzed with Clampfit and graphs were drawn with Excel. The amplitudes were normalized to the mean of the 10-min baseline recording before cholinergic pairing or disinhibition pairing. Values were presented as mean ± SEM.

EPSCs were evoked every 60 seconds by stimulating the SC pathway with an electrode placed in the stratum radiatum through a stimulator (Grass S88X). The stimulation intensity was 1-10 μA for 0.1 ms. To study the effects of cholinergic co-activation on SC to CA1 synaptic plasticity in Figure 2.2, cholinergic terminals in the hippocampus were optogenetically activated (10 pulses at 10 Hz, 1 sec before SC stimulation) through ChR2 that was selectively expressed in ChAT-cre positive (cholinergic) neurons. ChR2 was activated with 488-nm laser light (5 mW, 20 ms) through a 40× objective over CA1 stratum oriens near the septum with an Andor spinning disk confocal microscope (Andor technology). To examine the effects of disinhibition on SC to CA1 synaptic plasticity in Figure 2.4, Sst positive neurons were inhibited optogenetically through eNpHR which was activated through a 40x objective over CA1 stratum oriens with 530-nm laser light (20 mW) for 1 sec flanking SC stimulation.

The amplitudes of EPSCs were analyzed with Clampfit and graphs were drawn with Excel. The amplitudes were normalized to the mean of the 5-min baseline recording before cholinergic pairing or disinhibition pairing. Values were presented as mean ± SEM. Amplitude changes were compared with baseline before pairing by Student t-test. Recordings were done in 5 slices from 3 individual mice in each group. The sample size was estimated by Student t-test with an expected effect of 40% change, expected standard deviation of 15%, and 80% confidence interval width.

2.2.4 Model

The minimal network used in this study consists of an OLM cell (O), a fast-spiking interneuron (I), and a pyramidal cell. All the cells in the network are modeled as point neurons. Since we are interested in the local changes at the SC-CA1 synapse, the pyramidal cell is represented by a dendritic compartment (E_D). The cells of the network are connected through feedforward connections.

Adding connections between the CA1 pyramidal cell and the OLM interneuron did not significantly alter our results (simulations not shown). Therefore, we did not include synapses between the CA1 pyramidal and the OLM cells in our model. Our modeling choice is further supported by experimental studies showing that the IPSC elicited by an OLM interneuron has a small amplitude at the soma of CA1 pyramidal cells since these synapses are on the distal parts of the dendritic tree (Maccaferru et al., 2000), and that an action potential in CA1 pyramidal cells is insufficient to make the OLM cell membrane potential cross the action potential threshold (Ali et al., 1998).

Neuron dynamics models

The O and I cells are modeled following the Hodgkin-Huxley formalism (Hodgkin and Huxley, 1952) (transient I_{Na}, delayed rectifier potassium I_K, and leak I_{leak}), with synaptic currents I_{syn}. Its membrane potential V_m is described as follows:

$$C_m \frac{dV_m}{dt} = -I_{leak} - I_K - I_{Na} - I_{syn} \tag{2.1}$$

where C_m is the membrane capacitance. The I_{leak}, I_K and I_{Na} currents are given by:

$$I_{leak} = g_{leak}(V_m - E_{leak}) \tag{2.2}$$

$$I_K = \overline{g}_K n^4 (V_m - E_K) \tag{2.3}$$

$$I_{Na} = \overline{g}_{Na} m^3 h (V_m - E_{Na}) \tag{2.4}$$

where $\overline{g}_i$ and E_i are, respectively, the maximal conductance and reversal potential of channel i (i=leak, K, Na), and m, h and n are gating variables that obey the following differential equation:

$$\frac{dx}{dt} = \alpha_x(1 - x) - \beta_x \tag{2.5}$$

where α_x and β_x are voltage-dependent rate constants.

Following (Rotstein et al., 2005b) we included an applied current $I_{app} = -260$ pA, a persistent Na-current I_p, and a hyperpolarization-activated inward current I_h (with a slow and fast component) on the O-cells:

$$I_p = \overline{g}_p p (V_m - E_{Na}) \tag{2.6}$$

$$I_h = \overline{g}_h (0.65 h^f + 0.35 h^s)(V_m - E_h) \tag{2.7}$$

While the gate variable p obeys equation (2.5), h^f and h^s are described by the following equation:

$$\frac{dx}{dt} = \frac{x_\infty(V_m) - x}{\tau_x(V_m)} \tag{2.8}$$

where x_∞ is the voltage-dependent steady state and τ_x the time constant. Definitions for the α_x, β_x, x_∞ and τ_x for each of the dynamic variables are as follows.

For the O-cells:

$$
\begin{aligned}
\alpha_n &= -\frac{0.01(V_m + 27)}{exp(-0.1(V_m + 27)) - 1} \\
\beta_n &= 0.125exp(-\frac{V_m + 37}{80}) \\
\alpha_m &= -\frac{0.1(V_m + 23)}{exp(-0.1(V_m + 23)) - 1} \\
\beta_m &= 4exp(-\frac{V_m + 48}{18}) \\
\alpha_h &= 0.07exp(-\frac{V_m + 37}{20}) \\
\beta_h &= \frac{1}{exp(-0.1(V_m + 7)) + 1} \\
\alpha_p &= \frac{1}{0.15(1 + exp(-fracV_m + 386.5))} \\
\beta_p &= \frac{exp(-\frac{V_m+38}{6.5})}{0.15(1 + exp(-\frac{V_m+38}{6.5}))} \\
h^f_\infty &= \frac{1}{1 + exp(\frac{V_m+79.2}{9.78})} \\
\tau^f_h &= \frac{0.51}{exp(\frac{V_m-1.7}{10}) + exp(-\frac{V_m+340}{52})} + 1 \\
h^s_\infty &= \frac{1}{[1 + exp(\frac{V_m+2.83}{15.9})]^{58}} \\
\tau^s_h &= \frac{5.6}{exp(\frac{V_m-1.7}{14}) + exp(-\frac{V_m+260}{43})} + 1
\end{aligned}
$$

For the I-cells:

$$
\begin{aligned}
\alpha_n &= \frac{0.032(V_m + 52)}{1 - exp(-\frac{V_m+27}{5})}\\
\beta_n &= 0.5exp(-\frac{V_m + 57}{40})\\
\alpha_m &= \frac{0.32(V_m + 54)}{1 - exp(-\frac{V_m+54}{4})}\\
\beta_m &= \frac{0.28(V_m + 27)}{exp(\frac{V_m+27}{5}) - 1}\\
\alpha_h &= 0.128exp(-\frac{V_m + 50}{18})\\
\beta_h &= \frac{4}{exp(1 + exp(-\frac{V_m+27}{5}))}
\end{aligned}
$$

The parameter values used in the simulations are presented in Table 2.1.

Since we are interested in studying local synaptic changes of the SC-CA1 synapse, we use the following equation to describe the activity of the pyramidal cell dendritic compartment:

$$C\frac{dV_{E_D}}{dt} = -I_{leak} - I_{syn} \tag{2.9}$$

The parameters C, g_{leak}, and E_{leak} were set to 100 pF, 1 nS and -68 mV, respectively.

For the simulations of Figure 2.2D, noise was added to the dendritic compartment E_D to allow direct comparison with the experimental results portrait in Figure 2.2C. In addition to E_D, white noise was added to the O and I-cells in Figure S5 to study plasticity induction when these cells show spontaneous spiking. Since we used the Euler method to solve the differential equations describing V_O, V_I, and V_{E_D}, ($V_x[i+1] = V_x[i] + dt\frac{dV_x}{dt}$) noise was incorporated by adding a stochastic term $\sqrt{dt}\zeta$ ($V_x[i+1] = V_x[i] + dt\frac{dV_x}{dt} + \sqrt{dt}\zeta$), where ζ a random Gaussian variable with mean $\mu = 0$ and standard deviation σ(=1.1, 0.1 and 0.3 for the O, I and E_D cells respectively).

Parameter	**Value**
O-cells	
C_m	100 pF
g_{leak}	50 nS
E_{leak}	-70 mV
$\overline{g}_K$	1100 nS
E_K	-90 mV
$\overline{g}_{Na}$	5200 nS
E_{Na}	55 mV
$\overline{g}_p$	50 nS
$\overline{g}_h$	145 nS
E_h	-20 mV
I-cells	
C_m	100 pF
g_{leak}	10 nS
E_{leak}	-67 mV
$\overline{g}_K$	8000 nS
E_K	-100 mV
$\overline{g}_{Na}$	10000 nS
E_{Na}	50 mV

Table 2.1: Parameters of pyramidal cell, OLM interneuron, and fast-spiking interneuron dynamics. All the parameter values and expressions here described were taken from Rotstein et al. (2005b), considering a surface area of $1 \times 10^{-4} cm^2$, except for the reversal potential of the leakage current of the OLM which was set to have the resting potential of the OLM cells at -60 mV, as reported in R.Leão et al. (2012)

Synaptic models

The O-cell model includes a current mediated by $\alpha7$ nAChR channels, that in the real OLM neurons are presynaptic to the O- to I-cell synapse. The description of the current here used is an adaptation of the model proposed in Graupner et al. (2013), and it is given by

$$I_{\alpha7} = \overline{g}_{\alpha7} r_{\alpha7} (V_m - E_{\alpha7}) \tag{2.10}$$

where $\overline{g}_7$ is the maximal conductance of the $\alpha7$ nAChR channel, and $E_{\alpha7}$ the reversal potential. The opening gate variable $r_{\alpha7}$ is described by equation (2.8), with $\tau_{r\alpha7}$ constant and $r_{(\alpha7)\infty}$ given by

$$r_{(\alpha7)\infty} = \frac{[ACh]^n}{EC_{50}^n + [ACh]^n} \tag{2.11}$$

where EC_{50} is the half-maximum concentration and n the Hill's coefficient of activation.

The I-cell has an excitatory AMPA and inhibitory $GABA_A$ synaptic currents, described by the following set of equations:

$$I_{GABA_A} = \overline{g}_G r_G (V_m - E_G) \tag{2.12}$$

$$I_{AMPA} = \overline{g}_{AMPA} r_A (V_m - E_A) \tag{2.13}$$

The gating variables r_x is, as described in Destexhe et al. (1998), given by

$$\frac{dr_x}{dt} = \alpha_x [T](1 - r_x) - \beta_x r_x \tag{2.14}$$

where α_x and β_x are the opening and closing rate of the receptor channel, and $[T]$ the neurotransmitter's concentration available for binding.

The GABA released by the I-cell is described by using the Destexhe et al. simplified neurotransmitter release model (Destexhe et al., 1998), where a stationary relationship between presynaptic voltage and neurotransmitter release is deduced by fitting the model to experimental results. The intervening reactions in the release process are considered fast - a presynaptic action potential elicits a rapid influx of calcium, leading to the activation of transmitter-containing vesicles and neurotransmitter release. The following equation gives the neurotransmitter release as a function of the presynaptic voltage:

$$[GABA]_I = \frac{T_{max}}{1 + exp(-\frac{V_m - V_p}{K_p})} \tag{2.15}$$

where T_{max}= 1 mM is the maximal neurotransmitter concentration, $K_p = 5$ mV gives the function's steepness, and V_p= 2 mV sets the value at which the function is half-activated. These parameters were directly taken from Destexhe et al. (1998).

Concerning the GABA released by the O-cell, we assume that the $\alpha 7$ nAChR current is not strong enough to elicit an action potential directly, but, as the channels are presynaptic to the O-I GABAergic synapses, it can generate an increase in the intracellular calcium concentration sufficient to activate the vesicular release of GABA (Griguoli and Cherubini, 2012). To avoid the detailed computation of the mechanisms whereby calcium leads to exocytosis, we assume a sigmoid relationship between calcium and transmitter concentration given by:

$$[GABA]_O = \frac{T_{max}}{1 + exp(-\frac{Ca_i - Ca_p}{K_{(Ca)_p}})} \tag{2.16}$$

where T_{max}= 1 mM is the maximal neurotransmitter concentration, $K_{(Ca)p} = 1x10^{-6}\ mM$ gives the function's steepness, and $Ca_p = 4 \times 10^{-5}\ mM$ sets the value at which the function is half-activated. These parameters were chosen so that a pulse of calcium elicits GABA release with approximately the same characteristics (amplitude and duration) as the Destexhe et al. (1998) detailed model of transmitter release (see Figure S2).

The passive dendritic compartment of the pyramidal cell E_D is modeled using synaptic $GABA_A$, AMPA, and NMDA currents. The $GABA_A$ and AMPA currents are given by equations (2.12) and (2.13), respectively. The NMDA current is described according to the following equation:

$$I_{NMDA} = \overline{g}_N r_N B(V_m)(V_m - E_N) \tag{2.17}$$

where r_N is the gating variable described by equation (2.14). Due to the presence of a Mg^{2+} block, the NMDA channels a voltage-dependent term, $B(V_m)$, defined as:

$$B(V_m) = \frac{1}{1 + exp(-0.062V_m)\frac{[Mg^{2+}]}{3.57}} \tag{2.18}$$

The parameters α_A, β_A, E_A, α_N, β_N, E_N, $[Mg^{2+}]$, α_G, β_G and E_G were estimated by Destexhe et al. (1998) by fitting the models of postsynaptic $AMPA$, $NMDA$ and $GABA_A$ currents to experimental data. Regarding the synaptic currents of E_D, the AMPA and NMDA receptors maximal conductances were chosen such that at V=-70 mV, a glutamate pulse of 1 mM and 10 msec duration evoked AMPA and NMDA currents with an amplitude of 240 pA and 40 pA, respectively (Andrásfalvy et al., 2003). The maximal conductance of $GABA_A$ receptors was chosen such that at V=0 mV, a pulse of GABA with 1 msec duration and concentration of 1 mM evokes a current with an amplitude of 500 pA (Schulz et al., 2018). For the I-cell, the AMPA receptor maximal conductance value is such that one pulse of glutamate coming from the SC evokes a volley of action potentials. Concerning the $\alpha 7$ nAChR postsynaptic current, the parameters EC_{50}, $\tau_{r\alpha 7}$ and n were taken from Graupner et al. (2013). The parameter $E_{\alpha 7}$ was deduced from Castro and Albuquerque (1995), and $\overline{g}_{\alpha 7}$ was chosen such that activation of the $\alpha 7$ nAChR by a pulse of ACh evokes a current of 35 pA, as seen in R.Leão et al. (2012).

Calcium-induced calcium release (CICR) mechanism

Calcium entry through $\alpha 7$ nAChR cells initiates calcium release from internal stores (Tsuneki et al., 2000; Dajas-Bailador et al., 2002; Griguoli and Cherubini, 2012). The calcium concentration in the cytosol of OLM cells Ca_i is described by the following equation:

$$\frac{dCa_i}{dt} = -\xi'\alpha' I_{\alpha 7} + w_\infty^3 (Ca_{IS} - Ca_i) - \frac{Ca}{\tau_{Ca}} \tag{2.19}$$

where $\xi = 2.1 \times 10^{-6} mM/(msec\ pA)$ is a parameter that converts current into concentration, $\alpha = 0.05$ reflects the 5% calcium permeability of the $\alpha 7$ nAChRs (Vernino et al., 1994), and τ_{Ca} is the calcium decay constant. The parameter ξ was chosen so that the intracellular calcium concentration is of the same order of magnitude as observed experimentally in Sabatini et al. (2002). The parameter τ_{Ca}

was taken directly from the same study. Ca_{IS} represents the calcium concentration of the internal stores given by:

$$\frac{dCa_{IS}}{dt} = -w_{\infty}^{3}(Ca_{IS} - Ca_i) - \frac{Ca_{IS} - 0.4 \times 10^{-3}}{\tau} \tag{2.20}$$

where τ (= 10 msec) is the calcium decay constant, and w_{∞} is the open probability of calcium-permeable channels on the internal store, given by

$$w_{\infty} = \frac{Ca_i}{Ca_i + k_d} \tag{2.21}$$

where $k_d (= 2 \times 10^{-4} mM)$ is the half-activation of the function. The model assumes three calcium-binding sites (Young and Keizer, 1992) and a calcium concentration at the internal stores of 0.4 μM at rest (this value can be different as long as it is bigger than the intracellular calcium concentration Ca_i at rest). Please note that the CICR mechanism described is a simplification of the model proposed by Rinzel (1985), where we limit the model to account for the calcium activation sites of the calcium-permeable IP_3 receptors on the endoplasmic reticulum.

Model of synaptic plasticity

To study plasticity induction at the $SC - E_D$ synapse, we use a calcium-based synaptic plasticity model based on Shouval et al. (2002). We assume that changes in the AMPA receptor conductance reflect changes in the strength of the excitatory SC-CA1 synapse. Our synaptic plasticity model is formulated as follows:

$$\frac{d\overline{g}_{AMPA}}{dt} = \eta(Ca)(\Omega(Ca) - \sigma(\overline{g}_{AMPA} - g_0)) \tag{2.22}$$

where σ is a decay constant and g_0 (= 4 nS) is the value of the maximal conductance of the AMPAR at t=0. The variable η is a calcium-dependent learning rate described by equation (2.23), and Ω determines the sign magnitude of synaptic plasticity as a function of the intracellular Ca levels (equation (2.24)).

Parameter	**Value**	**Reference**
α_A	1.1 $ms^{-1}mM^{-1}$	Destexhe et al. (1998)
β_A	0.19 ms^{-1}	Destexhe et al. (1998)
$\overline{g}_{AMPA}$	$7^{\dagger}$, $4^{\ddagger}$ nS	Andrásfalvy et al. (2003)
E_A	0 mV	Destexhe et al. (1998)
$[Mg^{2+}]$	1 mM	Destexhe et al. (1998)
α_N	0.072 $ms^{-1}mM^{-1}$	Destexhe et al. (1998)
β_N	6.6 $\times 10^{-3}$ ms^{-1}	Destexhe et al. (1998)
$\overline{g}_N$	25 nS	Andrásfalvy et al. (2003)
E_N	0 mV	Destexhe et al. (1998)
α_G	5 $ms^{-1}mM^{-1}$	Destexhe et al. (1998)
β_G	0.18 ms^{-1}	Destexhe et al. (1998)
$\overline{g}_G$	$14^{\dagger}$, $7^{\ddagger}$ nS	Schulz et al. (2018)
E_G	-80 mV	Destexhe et al. (1998)
$E_{\alpha 7}$	0 mV	Castro and Albuquerque (1995)
$\overline{g}_{\alpha 7}$	3 nS	R.Leão et al. (2012)
EC_{50}	80 $\times 10^{-3}$ mM	Graupner et al. (2013)
$\tau_{r\alpha 7}$	5 ms	Graupner et al. (2013)
n	1.73	Graupner et al. (2013)

Table 2.2: Parameter values of synaptic currents I_{AMPA}, I_{NMDA}, I_{GABA_A} and $I_{\alpha 7}$. The values indicated with † refer to the conductance of postsynaptic channels on the fast-spiking interneurons, while the ones noted with ‡ refer to the conductances of the dendritic compartment E_D.

$$\eta(Ca) = (\frac{P_1}{P_2 + Ca_{P_3}} + P_4)^{-1} \tag{2.23}$$

$$\Omega(Ca) = \gamma_{\uparrow} \frac{exp(900(Ca - \theta_{\uparrow}))}{1 + exp(900(Ca - \theta_{\uparrow}))} - \gamma_{\downarrow} \frac{exp(900(Ca - \theta_{\downarrow}))}{1 + exp(900(Ca - \theta_{\downarrow}))} \tag{2.24}$$

The parameters $\theta_{\uparrow}$ and $\theta_{\downarrow}$ define the potentiation and depression onset, i.e., the calcium levels that trigger the removal and insertion of AMPAR in the membrane, respectively, and $\gamma_{\uparrow}$ and $\gamma_{\downarrow}$ represent the maximal insertion and removal rate of the AMPARs from the membrane. Please note that on the original model, the parameters $\theta_{\uparrow}$ and $\theta_{\downarrow}$ are represented by θ_p and θ_d, and define the potentiation and depression threshold, respectively, but, as it will be evident in the Results section, we find that this terminology can be misleading (i.e., we show that crossing these levels is necessary but not sufficient for potentiation). We assume that the primary source of Ca^{2+} in E_D is the calcium flux entering the cell through the NMDA receptor channels. The intracellular Ca^{2+} concentration evolves according to the following equation

$$\frac{dCa}{dt} = -\xi \alpha I_{NMDA} - \frac{Ca}{\tau_{Ca}} \tag{2.25}$$

where ξ is a parameter that converts current into concentration, α=0.1 refers to the fact that only about 10% of the NMDA current is composed of calcium ions (Burnashev et al., 1995), and τ_{Ca} is the calcium decay constant. The parameter ξ was chosen so that the intracellular calcium concentration is of the same order of magnitude as observed experimentally in Sabatini et al. (2002) [1]. The parameter

---

[1] The reversal potential of the compound of all the ionic currents flowing through the NMDARs is employed in the voltage equation (2.1) and the calcium dynamics equation (2.25), even though only the calcium component of the NMDAR total current contributes to the intracellular calcium concentration. We recognize that this is an ad hoc simplification which does not qualitatively affect the model results since V_{E_D} ranges between -30 and -67 mV mV in the simulations.. The model can be modified to account for the calcium component of the NMDA current in the calcium dynamics equation by using the calcium reversal potential of 140 mV to describe the fractional calcium through the NMDARs in equation (2.25), similarly to how it was laid out in Graupner and Brunel (2005b). We note that this would not quantitatively change our results provided the parameter ξ is altered accordingly, i.e., to ensure the resultant calcium magnitude remains in the same order of magnitude as observed experimentally. On the other hand, this simplification becomes important when considering a spiking model for the pyramidal cell where the transmembrane voltage exceeds

τ_{Ca} was taken directly from the same study. P_1, P_2, P_3 and P_4 were chosen to have a calcium-dependent learning rate that increases monotonically with calcium levels (Shouval et al., 2002). The parameters $\theta_\uparrow$ and $\theta_\downarrow$ were determined such that before the co-pairing period the calcium concentration does not cross either while crossing the potentiation onset $\theta_\uparrow$ when pairing starts (with $\theta_\uparrow > \theta_\downarrow$). The parameters σ, $\gamma_\uparrow$ and $\gamma_\downarrow$ were chosen to reproduce the experimental results concerning potentiation of CA1 pyr cell EPSC during co-activation of SC and disinhibition/cholinergic inputs (with $\gamma_\uparrow > \gamma_\downarrow$).

Parameter	**Value**	**Reference**
σ	0.0040	-
P_1	1.5×10^{-6}	Shouval et al. (2002)
P_2	$P_1 \times 10^{-4}$	Shouval et al. (2002)
P_3	13	Shouval et al. (2002)
P_4	1	Shouval et al. (2002)
$\theta_\uparrow$	$0.35^{\S}$, $0.34^{\P}$	-
$\theta_\downarrow$	$0.28^{\S}$, $0.31^{\P}$	-
$\gamma_\uparrow$	$0.0783^{\S}$, $0.0699^{\P}$	-
$\gamma_\downarrow$	0.0375	-
α	0.1	Burnashev et al. (1995)
ξ	$0.006^{\S}$, $0.045^{\P}$ $\mu M/(ms\ pA)$	Sabatini et al. (2002)
τ_{Ca}	12 ms	Sabatini et al. (2002)

Table 2.3: Parameter values for calcium dynamics and synaptic plasticity. The values indicated with § were used to reproduce Figures 2.2, S4, S5, and S7. The values indicated with ¶ were used to reproduce the remaining figures.

---

0 mV and thereby inverting the polarity of the total but not the calcium current.

Parameters of the model: We used experimentally determined values or values from previous modeling studies for most of the parameters. Others that could not be determined experimentally were determined by experimental constraints imposed on the model, namely, the maximal conductances $\overline{g}_x$, and the synaptic plasticity model parameters indicated with a dash on Table 2.3. All the parameter values are defined in Tables 2.1, 2.2, 2.3. With our choice of parameters, all parameters are within the physiological range.

2.3 Results

2.3.1 Co-activation of cholinergic and glutamatergic inputs modifies the SC-CA1 synaptic transmission

Previously, it has been observed that co-activation of hippocampal cholinergic inputs and local SC pathway increases the amplitude of SC to CA1 pyramidal EPSCs (Gu et al., 2020). Moreover, repeated pairing of cholinergic and hippocampal inputs (8 times) increased EPSC amplitudes in pyramidal neurons during the pairing and long after, indicating long-term synaptic plasticity at SC to CA1 excitatory synapses. The induction of potentiation was abolished by a knockout of OLM$\alpha 2$ interneuronal $\alpha 7$ nAChRs, but not by knockout of these receptors on hippocampal pyramidal cells or other interneurons (see Figures 2.2 (A) and 2.2 (C)).

SC stimulation elicits EPSCs in s.r. interneurons and in the CA1 pyramidal cell proximal dendrites (R.Leão et al., 2012). Given the high calcium permeability of the $\alpha 7$ nAChRs, we assume their activation modulates transmitter release through calcium-mediated signal transduction cascades.

We constructed a minimal feedforward circuit with an OLM cell (O), a fast-spiking interneuron (I), and the pyramidal cell s.r. dendritic compartment (E_D) connected as schematically shown in Figure 2.2(B) to examine mechanistically how pairing cholinergic activation of the O-cell with glutamatergic activation of the I-cell and E_D can potentiate the EPSCs of E_D. We look at how the EPSC of E_D, modeled as the sum of the postsynaptic AMPA and NMDA currents (I_{AMPA} and I_{NMDA}), changes when the glutamatergic inputs acting on the I-cell and E_D are paired with the cholinergic inputs that act on the presynaptic $\alpha 7$ nAChR of the O-cell during a co-pairing period of 8 minutes, identical to the experimental protocol. The I-cell and E_D receive one glutamate pulse per minute before, during and after the co-pairing period. During the co-pairing period, the O-cell gets a pulse of ACh per minute, 100 msec before each glutamate pulse. Not much is known about ACh's concentration profile *in vivo*, but it is believed that it can be cleared from the synaptic cleft within milliseconds. After testing different ACh profiles, we decided to model ACh as a square pulse with a duration of 5 msec and concentration of 1 mM, similar to the glutamate, even though similar results were obtained for a variety of profiles of ACh (see appendix B for more details).

From Figure 2.2(D), we see that during the co-pairing period (from t=10 min to t=18 min), the EPSC is increased. This increase in our model is maintained for an extended period after the co-pairing period is over (black line), matching the experimental results. We also see that GABA release from the I-cells, $GABA_I$, decreases significantly (Figure 2.2(D) inset). Before the co-pairing period, glutamatergic inputs activate the I-cell. This results in E_D inhibition, which shows a SC-evoked depolarization immediately followed by hyperpolarization of its membrane potential. During the co-pairing period, activation of $\alpha 7$ nAChRs 100 msec before SC stimulation results in a calcium flux into the OLM cell that will initiate calcium-induced calcium release (CICR) from internal stores, exerting positive feedback. The increase in intracellular calcium concentration induces the release of GABA, as described by equation (2.16). GABAergic inputs from the OLM cell disable the SC-evoked activation of the I-cell. As a result, E_D does not receive GABAergic inputs (see Figure S4).

If we reduce the maximal conductance of the $\alpha 7$ nAChR, $\overline{g}_{\alpha 7}$, from 3 nS to 0.3 nS as an approximation of the effect of $\alpha 7$ knockout, co-pairing no longer potentiates the EPSC of E_D (Figure 2.2 (D), orange line). These observations are in accordance with experimental results that showed that this form of EPSC boost was abolished by knockout of the $\alpha 7$ nAChR in OLM$\alpha 2$ interneurons (Figure 2.2(C)).

We then examined how the key parameters of the co-paring protocol influence the plasticity of the SC-CA1 EPSCs. According to our model, the duration of the co-pairing period, the relative time between the cholinergic and glutamatergic inputs, as well as their frequency during the co-pairing period, can modulate the efficiency and direction of plasticity. Our simulations show that the longer the co-pairing period, the longer the transient duration, where the potentiation transient duration was defined as the time it takes the EPSCs to return to the baseline value once the co-pairing period is over (Figure 2.3(A)). We observe a positive relationship between the frequency of the glutamatergic and cholinergic inputs during a fixed period of paring protocol and the potentiation transient duration (Figure 2.3(B)). Interestingly, our simulations suggested that while changing the co-pairing period and the frequency of stimulation modulates the efficiency of the induction of potentiation, it does not change the direction of plasticity. Only when varying the relative time between the

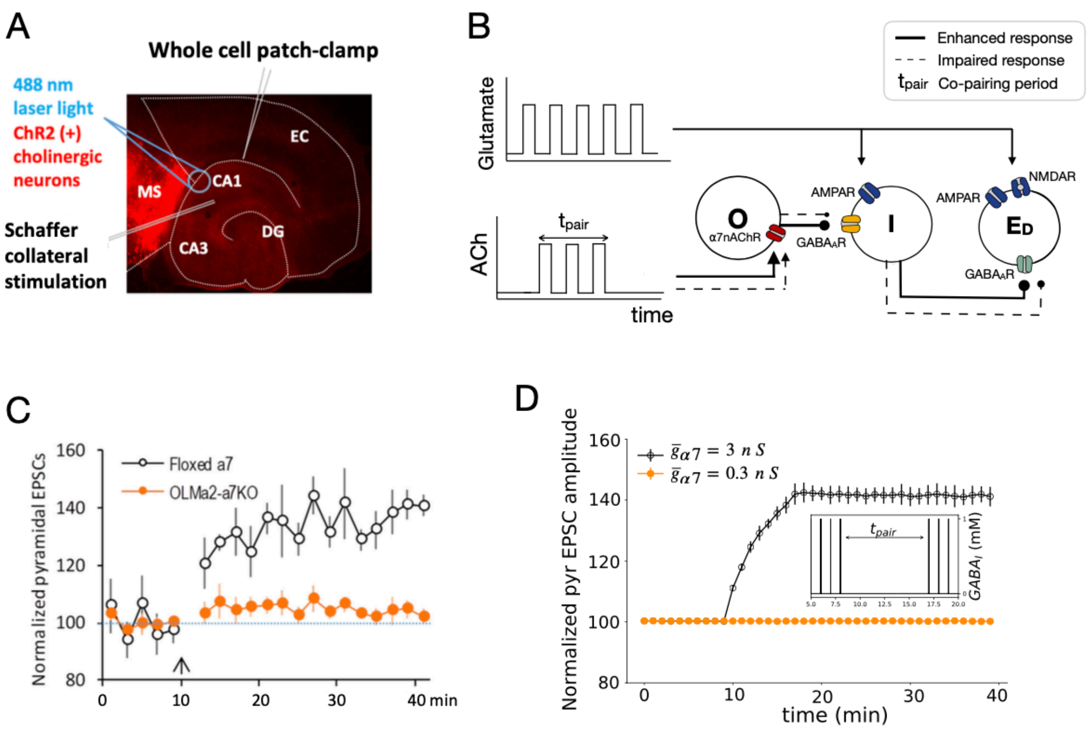

Figure 2.2: Cholinergic activation of OLM interneurons potentiates SC-evoked EPSCs. **(A)** Scheme of *in vitro* induction of cholinergic pairing induced hippocampal synaptic plasticity. EPSCs were recorded from CA1 pyramidal neurons. Cholinergic neurons were activated via channelrhodopsin-2 that was specifically expressed in ChAT-positive neurons. The Schaffer collateral (SC) pathway was activated by a stimulating electrode. Adapted from Gu et al. (2020). **(B)** Scheme of the minimal network used to study the role of cholinergic inputs in the potentiation of SC-evoked EPSCs. Glutamatergic inputs activate the pyramidal cell dendritic compartment (E_D) and the fast-spiking interneuron (I) that projects to it. ACh activates the OLM interneuron (O) during the co-pairing period. **(C)** Normalized SC-evoked EPSC responses from CA1 pyramidal neurons showing that the enhancement of EPSCs was impaired in hippocampal slices from mice with selective $\alpha7$ nAChR knockout in OLM$\alpha2$ interneurons. Adapted from Gu et al. (2020). **(D)** Numerical simulation of normalized EPSC amplitude when glutamatergic inputs acting on the I-cell and E_D are paired with cholinergic inputs acting on the O-cell (from t=10 min to t=18 min). The EPSCs are calculated as the sum of postsynaptic AMPA and NMDA currents, I_{AMPA} and I_{NMDA}, resulting from 10 simulations with white noise on the E_D membrane potential. Normalization of the results was calculated according with the expression $(100 + (EPSC - EPSC_{min}).(150 - 100))/(EPSC_{max} - EPSC_{min})$. The same results are obtained if a noisy background current inducing spontaneous spiking is added to the O and I-cells (see Figure S5). Inset: Concentration of GABA released from fast-spiking interneurons (I), calculated according to equation (2.15)

ACh and glutamate pulses could we induce a change in the plasticity direction. For single pulse pairing, potentiation will be induced if the glutamatergic inputs arrive at I and E_D within $10.3 < \Delta t < 120.5$ msec following the ACh pulse. If $-10.6 < \Delta t < 10.3$ msec or $120.5 < \Delta t < 205$ msec, depression is induced (Figure 2.3(C)). The time-dependent plasticity curve does not change shape if we pair doublets of glutamate and ACh with a θ frequency (4 Hz) instead of single pulses. Still, it changes the potentiation and depression windows. The potentiation window is of $10.3 < \Delta t < 299.3$ msec, while the depression window is $-10.7 < \Delta t < 10.3$ msec and $299.3 < \Delta t < 375$ msec (see Figure 2.3(D) and Figure S7). These results agree with experimental findings by Gu and Yakel (2011) showing that activation of cholinergic inputs 100 msec and 10 msec prior to SC stimulation induced SC to CA1 long-term potentiation and short-term depression, respectively.

2.3.2 Disinhibition of the CA1 pyramidal cell dendritic compartment enables potentiation of the SC-CA1 synaptic transmission.

Our model shows a decrease in GABA release from I-cells during the co-pairing period (Figure 2.2 (D), inset). To study the role of disinhibition of E_D in the potentiation of the SC-CA1 excitatory synapse, we use a model where E_D receives a pulse of glutamate followed by a pulse of GABA, except during a disinhibition period when it only receives pulses of glutamate.

According to our model, the rise and decay time of GABA concentration release that results from the spiking of the I-cells is almost instantaneous (see Figure S6). Therefore, in this section, GABAergic inputs into E_D are modeled as a square pulse. For simplicity, both glutamate and GABA release pulses are modeled as square pulses with a duration of 1 msec and 1 mM of amplitude. It is important to note that pulses with amplitudes and durations different from those considered here would reproduce the same results, as long as the duration and amplitude of glutamate and GABA are similar (simulations not shown). Thus, E_D receives one pulse of glutamate per minute, followed by a pulse of GABA 2 msec after, except during a disinhibition period when it only receives pulses of glutamate. We note that this simulated stimulation and pairing choice directly follows the experimental protocol

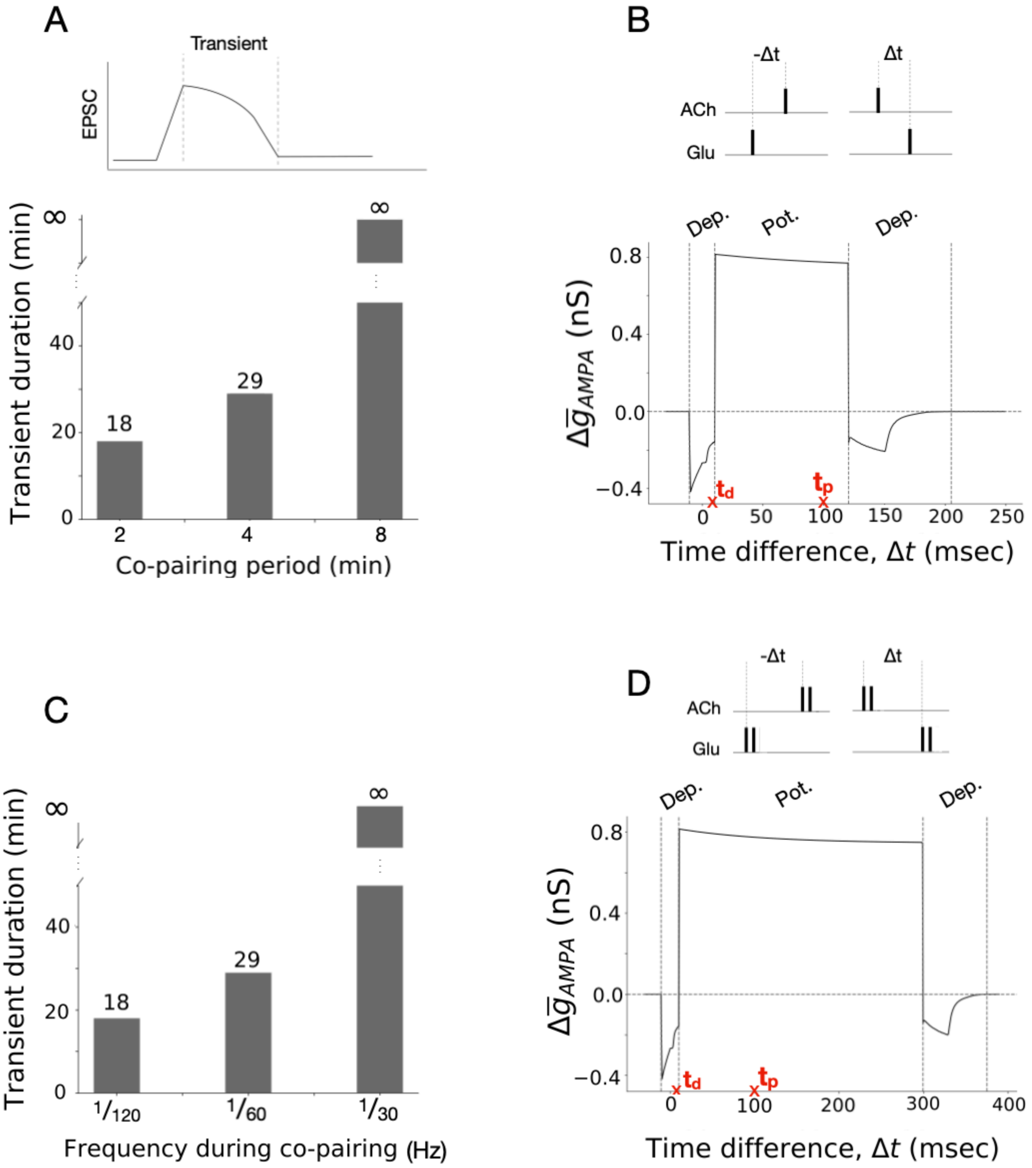

Figure 2.3: Co-pairing temporal parameters determine the duration and polarity of synaptic plasticity: relative timing between cholinergic and glutamatergic stimulation, the extent of the co-pairing period, and the frequency of stimulation. **(A)** Synaptic strength transient duration is proportional to the extent of the pairing period. Here, the transient duration is defined as the time it takes the EPSC to go back to baseline after co-pairing is over. The I-cell and E_D receive a pulse of glutamate per minute. During the co-pairing period, the O-cell receives a pulse of ACh per minute, 10 msec before the glutamate pulses. **(B)** Synaptic strength transient duration is proportional to the ACh and glutamate pulses frequency during the co-pairing period. Before and after the co-pairing period, the I-cell and E_D receive a glutamate pulse per minute. During the co-pairing period (4 minutes), the frequency changes to $\frac{1}{120}$, $\frac{1}{60}$ or $\frac{1}{30}$ Hz, and the O-cell receives a pulse of ACh 10 msec before the glutamate pulses with the same frequency. (*caption continues on next page*)

(C) Relative paring timing provides a window of opportunity for plasticity. If glutamatergic inputs are administrated within 10.3 msec $< \Delta t <$ 120.5 msec, the E_D excitatory synapse is potentiated. If glutamatergic inputs are administrated within -10.7 msec $< \Delta t <$ 10.3 msec or 120.5 msec $< \Delta t <$ 205 msec, depression is induced. The change in the AMPAR conductance $\Delta \overline{g}_{AMPA}$ is measured 60 msec after one pairing. **(D)** Pairing multiple pulses of glutamate and ACh can change the window of opportunity for plasticity. Two pulses of glutamate and ACh with a frequency of 4 Hz are paired. If glutamatergic inputs arrive within -10.7 msec $< \Delta t <$ 10.3 msec or 299.3 msec $< \Delta t <$ 375 msec of the cholinergic inputs, depression is induced. If glutamatergic inputs are administrated within 10.3 msec $< \Delta t <$ 299.3 msec, the E_D excitatory synapse is potentiated. The change in the AMPAR conductance $\Delta \overline{g}_{AMPA}$ is measured 60 msec after one pairing. The pairing times of cholinergic and SC inputs found by Gu and Yakel to induce short-term depression and long-term potentiation at the SC-CA1 synapse (indicated with the red cross) are within our range of depression and potentiation (Gu and Yakel, 2011).

(see Methods).

We observed that before the disinhibition period, there were no changes in the EPSC amplitude of E_D. During the disinhibition period, the EPSC amplitude increases, and the longer the disinhibition period lasts, the longer these changes last. More specifically, for a disinhibition period of 5 minutes, the EPSC returns to baseline once the disinhibition period is over. For a longer disinhibition period of 8 minutes, the EPSC remains potentiated long after the disinhibition period is over (Figure 2.4(D)). After 5 minutes of E_D disinhibition, the EPSC amplitude was increased from 169.40 pA to 285.34 pA. After 8 minutes of disinhibition, the EPSC amplitude increased to 361.33 pA. These results hold for different values of $\gamma_\uparrow$ and $\gamma_\downarrow$ (see Figure S8). This is in accordance with experimental results, where inhibition of Sst interneurons projecting to CA1 pyramidal cells was paired with SC stimulation for a short and long period (Figure 2.4(C)). Inhibition of Sst interneurons via eNpHR resulted in increased SC-CA1 EPSC amplitude not only during the Sst inhibition but also after the end of Sst inhibition. The EPSC enhancement after the Sst inhibition lasted about 10min after 5 minutes of Sst inhibition and more than 30 min after 8 minutes of Sst inhibition. After 5 times of Sst inhibition, the EPSC amplitude was significantly increased at 5min after the end of Sst inhibition (31.8% increase compared with baseline, $p = 0.0003$) but returned to baseline at 30 min after Sst inhibition (2.8% increase compared with baseline, $p = 0.79$). After 8 times of Sst inhibition, the EPSC amplitude was significantly increased at both 5min after the end of Sst inhibition (37.3% increase compared with baseline, $p < 0.0001$) and 30 min after Sst inhibition (32.5% increase compared with baseline, p

< 0.0001). Experiments showed that inhibition of OLMα2 interneurons via eNpHR did not change the amplitude of SC-CA1 EPSC, indicating that the Sst interneurons inducing potentiation do not include OLM (Figure 2.4 (C), grey line).

AMPARs are known to play an important role in regulating and expressing synaptic plasticity in the hippocampus (Barria et al., 1997). From Figure 2.5 we see that there is an increase of $\overline{g}_{AMPA}$ during the disinhibition period. The longer the disinhibition period, the more significant the increase. For a disinhibition period of 5 minutes, there is an increase of $\overline{g}_{AMPA}$ from 4 to 6.9 nS during disinhibition. Afterward, $\overline{g}_{AMPA}$ gradually goes back to its baseline value (Figure 2.5(A)). For a disinhibition period of 8 minutes, $\overline{g}_{AMPA}$ increases from 4 to 8.83 nS. When the disinhibition period is over, $\overline{g}_{AMPA}$ remains potentiated (Figure 2.5(B)). It is important to note that without regular synaptic stimulation, $\overline{g}_{AMPA}$ decays back to its resting value after the disinhibition period, i.e., $\overline{g}_{AMPA}$ has only one stable fixed point and it is not bistable. In this study, we focused on a calcium-based synaptic plasticity model to describe changes in the excitatory SC-CA1 synapse. To gain a more detailed understanding of how the evolution of the calcium levels relates to the changes in the synaptic weights, we can examine the calcium dynamics before, during and after the disinhibition period. Figures 2.5(C) and (D) show that the calcium concentration increases significantly during the disinhibition period, crossing the potentiation onset $\theta_{\uparrow}$ with a significant margin. Immediately after the end of the disinhibition period, the calcium levels decrease, yet they remain above $\theta_{\uparrow}$. We can see a clear difference in calcium dynamics for the short and the long disinhibition periods. In the case of a short disinhibition period, each pairing of GABA and glutamate after the disinhibition period will elicit a calcium pulse with a smaller amplitude than the previous one. Eventually, at t=25 min, the calcium concentration from the pairing is not enough to cross the potentiation onset $\theta_{\uparrow}$. By the time t=30 min, calcium does not cross either the potentiation ($\theta_{\uparrow}$) or the depression onset ($\theta_{\downarrow}$), having a similar amplitude as before the disinhibition period. In the case of a long disinhibition period, each pairing performed after the disinhibition period evokes a calcium pulse with a constant amplitude. In other words, long-disinhibition periods ensure that the consequent pairings yield calcium responses that do not drop below the onset thresholds. To better visualize the synaptic and calcium dynamics immediately after the disinhibition period in both cases, we plot the system's trajectory in

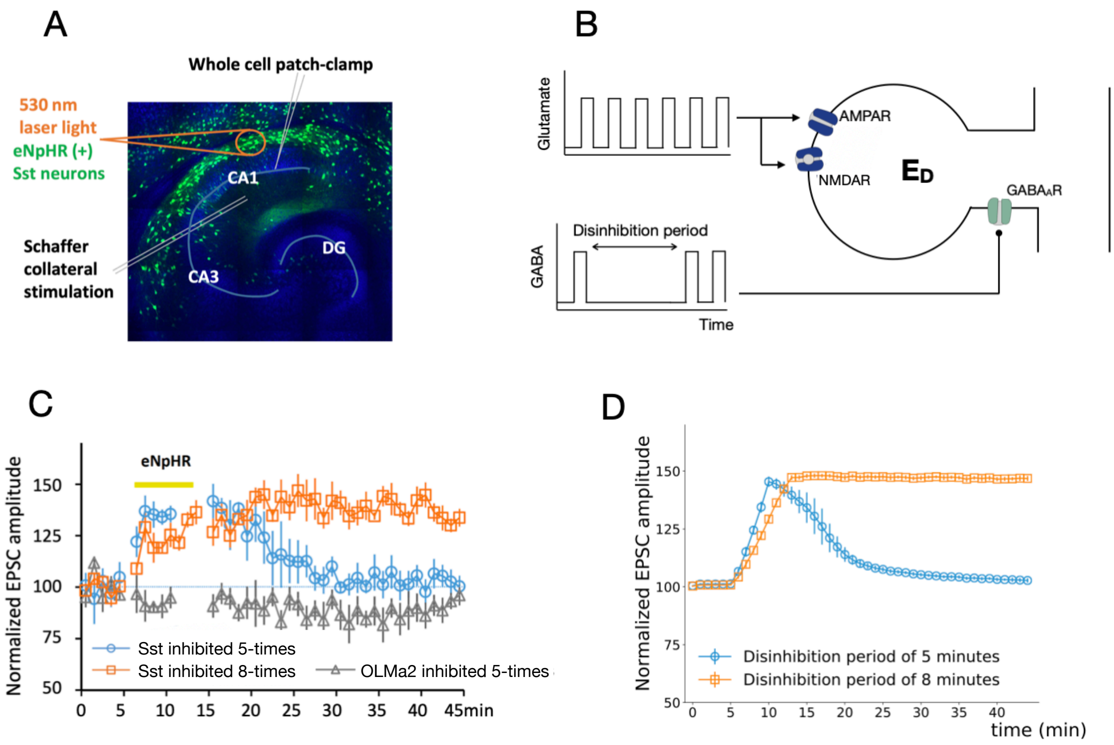

Figure 2.4: Disinhibition of CA1 pyramidal cell facilitates induction of hippocampal synaptic plasticity. (A) Scheme of *in vitro* induction of hippocampal synaptic plasticity through concurrent Sst inhibition. EPSCs were recorded from CA1 pyramidal neurons. Sst neurons were inhibited via eNpHR that was specifically expressed in Sst-positive neurons. The Schaffer collateral (SC) pathway was activated by a stimulating electrode. **(B)** Schematic representation of a CA1 pyramidal neuron dendritic compartment E_D with postsynaptic $GABA_A$, AMPA and NMDA receptors used to study the disinhibitory mechanisms for induction of plasticity at the SC-CA1 excitatory synapse. The pyramidal cell's dendritic compartment receives one pulse of both glutamate and GABA per minute, except during the disinhibition period, where it only receives pulses of glutamate. Glutamate binds to the excitatory AMPA and NMDA receptors, while GABA binds to the inhibitory $GABA_A$ receptor. **(C)** Experimental measurements showing the effects of inhibition of Sst and OLMα2 interneurons in s.o. on SC-evoked EPSCs. Inhibition of Sst interneurons from t=5min to t=10min enhanced the SC-evoked EPSC amplitude of the CA1 pyramidal cell, followed by a return to the baseline after the inhibition period (blue line). Inhibition of Sst interneurons from t=5min to t=13min increased SC-evoked EPSCs amplitude, which remained potentiated after the inhibition period (orange line). **(D)** Numerical simulation of normalized EPSCs of E_D for a disinhibition period of 5 minutes (from t=5 min to t=10 min) and 8 minutes (from t=5 min to t=13 min). Normalization of the results was calculated according with the expression $(100 + (EPSC - EPSC_{min}).(150 - 100))/(EPSC_{max} - EPSC_{min})$.

the Ca-$\overline{g}_{AMPA}$ plane. We do so for $\overline{g}_{AMPA}(t_{init})$=6.9 nS and for $\overline{g}_{AMPA}(t_{init})$=8.83 nS (Figure 2.5(E)), which are the values of $\overline{g}_{AMPA}$ at the end of the disinhibition period for the short- and long- disinhibition durations. For $\overline{g}_{AMPA}(t_{init})$=6.9 nS, the calcium concentration crosses the potentiation onset $\theta_{\uparrow}$ ($Ca_{max} = 0.353$ μM), but there is a decrease of $\overline{g}_{AMPA}$ from 6.9 to 6.8 nS. For $\overline{g}_{AMPA}(t_{init})$= 8.83 nS, the calcium concentration crosses $\theta_{\uparrow}$ to a larger extent ($Ca_{max} = 0.389$ μM) and there is an increase of $\overline{g}_{AMPA}$ from 8.83 to 8.92 nS. These results suggest that it is necessary but not sufficient for calcium concentration to cross the potentiation onset to induce potentiation. To verify this, we looked at changes in maximal conductance of the postsynaptic AMPAR, $\Delta\overline{g}_{AMPA}$, as a function of the amplitude of the intracellular calcium, Ca_{max}. From Figure 2.5(F), we see that as Ca_{max} increases we only start to have potentiation ($\Delta\overline{g}_{AMPA} > 0$) when Ca_{max} crosses not the potentiation onset $\theta_{\uparrow}$, but a higher level, that we term as the potentiation threshold θ_{pot}, 0.36 μM.

We do note that the fixed potential threshold θ_{pot} is not an ideal indicator of potentiation, as it may need to be re-calculated depending on a specific case of calcium dynamics time scales and/or the induction protocol. As seen in Figure 2.5, the dynamics of calcium is important in the induction of plasticity. Therefore, changing these by, for example, changing the calcium decay rate, can alter the θ_{pot} by changing the time calcium spends in the depression/potentiation onset region. This kind of analysis can also fail to identify mechanisms of induction of potentiation. As shown in Figure 2.6(B), if we consider a second calcium source that becomes activated at t = 80 msec, none of the 2 pulses of calcium generated crosses θ_{pot}; however, the synapse is potentiated. These examples suggest that it is not the peak calcium concentration that is a key indicator of potentiation but a measure based on the total amount of calcium that exceeds the onset levels. We suggest that a better quantity that can be used more generally as an indicator of plasticity is the ratio between the integral of calcium when its concentration is above the potentiation onset $\theta_{\uparrow}$, which we will call the area of AMPAR insertion (orange area in Figure 2.6), and the integral of calcium when its concentration is above the depression onset $\theta_{\downarrow}$ and bellow the potentiation onset $\theta_{\uparrow}$, which we will call the area of AMPAR removal (grey area in Figure 2.6), weighted by the calcium-dependent learning rate η, which we named $(\frac{A_{\uparrow}}{A_{\downarrow}})_w$ (see appendix A for more details). If this ratio is below 3.0, depression is induced in our model; if the ratio is above 3.0, potentiation is induced

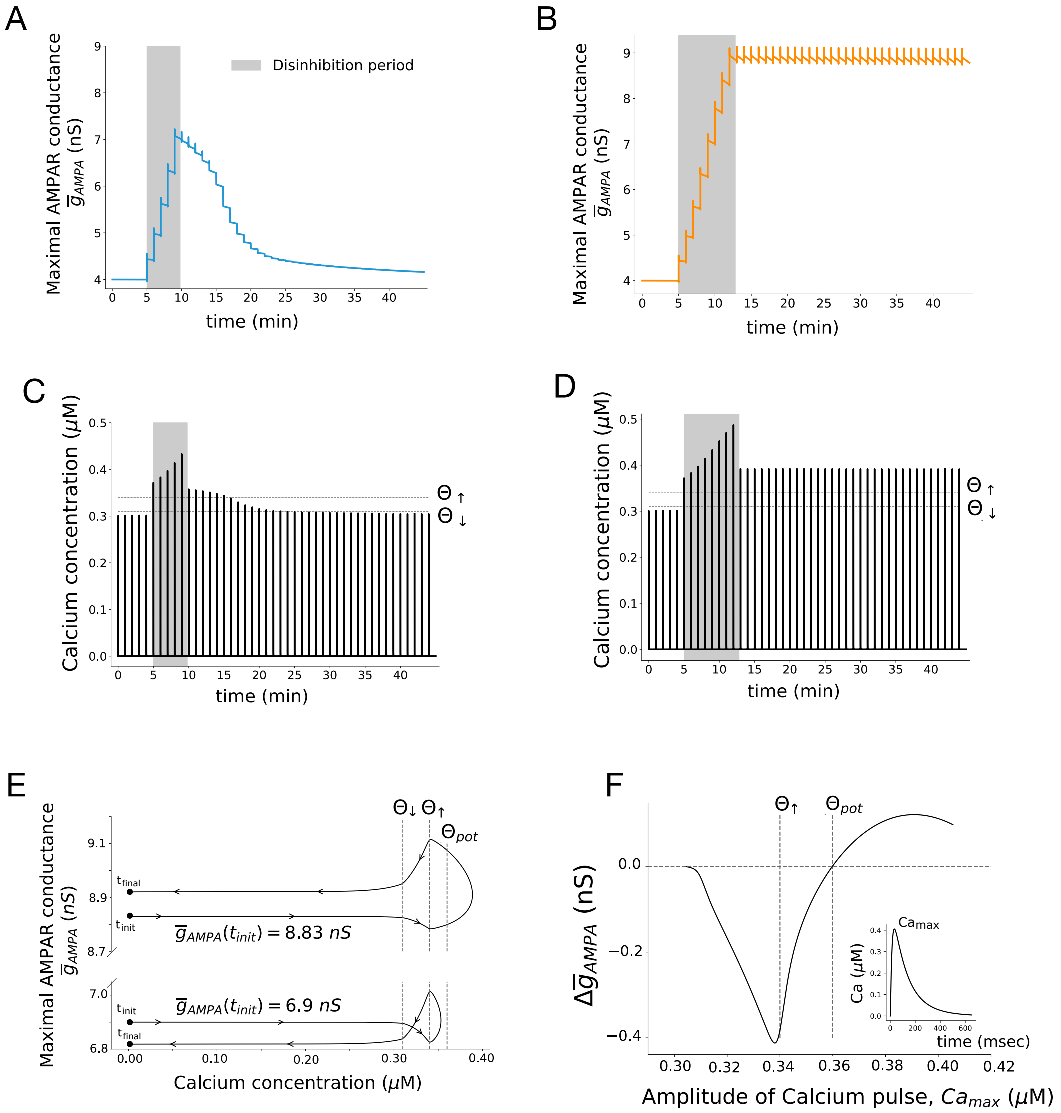

Figure 2.5: Calcium dynamic is key for the induction of synaptic plasticity. **(A)** Time course of maximal AMPAR conductance, $\overline{g}_{AMPA}$, when the dendritic compartment is disinhibited for a short period (from t=5 min to t=10 min). The maximal AMPAR conductance increases from its initial value $\overline{g}_{AMPA}$= 4 nS to $\overline{g}_{AMPA}$=6.9 nS during the disinhibition period. **(B)** Time course of $\overline{g}_{AMPA}$ when the dendritic compartment is disinhibited for a long period (from t=5 min to t=13 min). It increases from $\overline{g}_{AMPA}$= 4 nS to $\overline{g}_{AMPA}$=8.83 nS during the disinhibition period. Changes in the AMPAR conductance $\overline{g}_{AMPA}$ are described by equation (2.22). **(C)** Time course of intracellular calcium concentration when dendritic compartment E_D is disinhibited for a short period (from t=5 min to t=10 min), where $\theta_\downarrow$ is the depression onset, and $\theta_\uparrow$ the potentiation onset. **(D)** Time course of intracellular calcium concentration when the dendritic compartment is disinhibited for a long period (from t=5 min to t=13 min). The calcium dynamics is described by equation (2.25) (see Methods). **(E)** Trajectories of the system in the $\overline{g}_{AMPA}$-Ca plane when a pulse of glutamate is paired with a pulse of GABA for $\overline{g}_{AMPA}$=6.9 nS and $\overline{g}_{AMPA}$=8.83 nS, where θ_{pot} is the potentiation threshold as defined in Shouval et al. (2002). (*caption continues on next page*)

(F) Changes in the maximal AMPAR conductance, $\Delta\overline{g}_{AMPA}$, as a function of the amplitude of intracellular calcium pulse, Ca_{max}. Each point of the graph was obtained by submitting E_D to a glutamate pulse for different initial values of $\overline{g}_{AMPA}$. This induced different depolarization levels and, consequently, different activation levels of NMDARs and calcium pulses of different amplitudes.

(see Figure 2.6).

2.3.3 GABA amplitude and Glu-GABA pairing timing control membrane potential

Disinhibition of the pyramidal cell, i.e., reduction of GABAergic inputs, can facilitate the depolarization of the cell, which can control plasticity, as we have shown in the previous section. Therefore, we hypothesize that the amplitude of the GABA pulse, $GABA_{max}$, and the relative time between the glutamate and GABA pulses, $\Delta t_{(GABA-Glu)}$, can modulate plasticity. To explore this hypothesis, we pair glutamatergic inputs with GABAergic inputs into E_D. We vary the relative time between the inputs, $\Delta t_{(GABA-Glu)}$, and the amplitude of the GABAergic inputs, $GABA_{max}$, to measure changes induced in $\overline{g}_{AMPA}$. Simulations were repeated for different values of $\overline{g}_{AMPA}$ to understand why pulses of glutamate and GABA with the same characteristics (same amplitude and same duration) have different outcomes when administered after the short or long disinhibition periods. Simulations were done with three initial values of $\overline{g}_{AMPA}$: $\overline{g}_{AMPA}$= 4 nS, $\overline{g}_{AMPA}$= 6.9 nS and $\overline{g}_{AMPA}$= 8.83 nS. We identified well-defined regions of potentiation and depression in the $\Delta t_{(GABA-Glu)}$-$GABA_{max}$ parameter space (see Figure 2.7). We also saw that the regions change with the value of $\overline{g}_{AMPA}$. More specifically, the depression region moves towards the right of the plot as $\overline{g}_{AMPA}$ increases. In other words, as $\overline{g}_{AMPA}$ increases, the GABAergic inputs need to arrive with a longer delay relative to the glutamatergic inputs to induce depression. It is important to note that the level of potentiation or depression induced also changes as we increase $\overline{g}_{AMPA}$. Generally, the magnitude of potentiation decreases, and the magnitude of depression increases. This is because the system saturates as $\overline{g}_{AMPA}$ increases, i.e., $\overline{g}_{AMPA}$ cannot increase indefinitely. This is a restriction imposed by the model. These results suggest that the same induction protocol may induce either potentiation or depression, more or less efficiently, depending on the current phosphorylation state of the AMPA receptors, i.e. $\overline{g}_{AMPA}$, and on the decrease of GABA during disinhibition. In other words, the net effect of a pairing protocol is state-dependent.

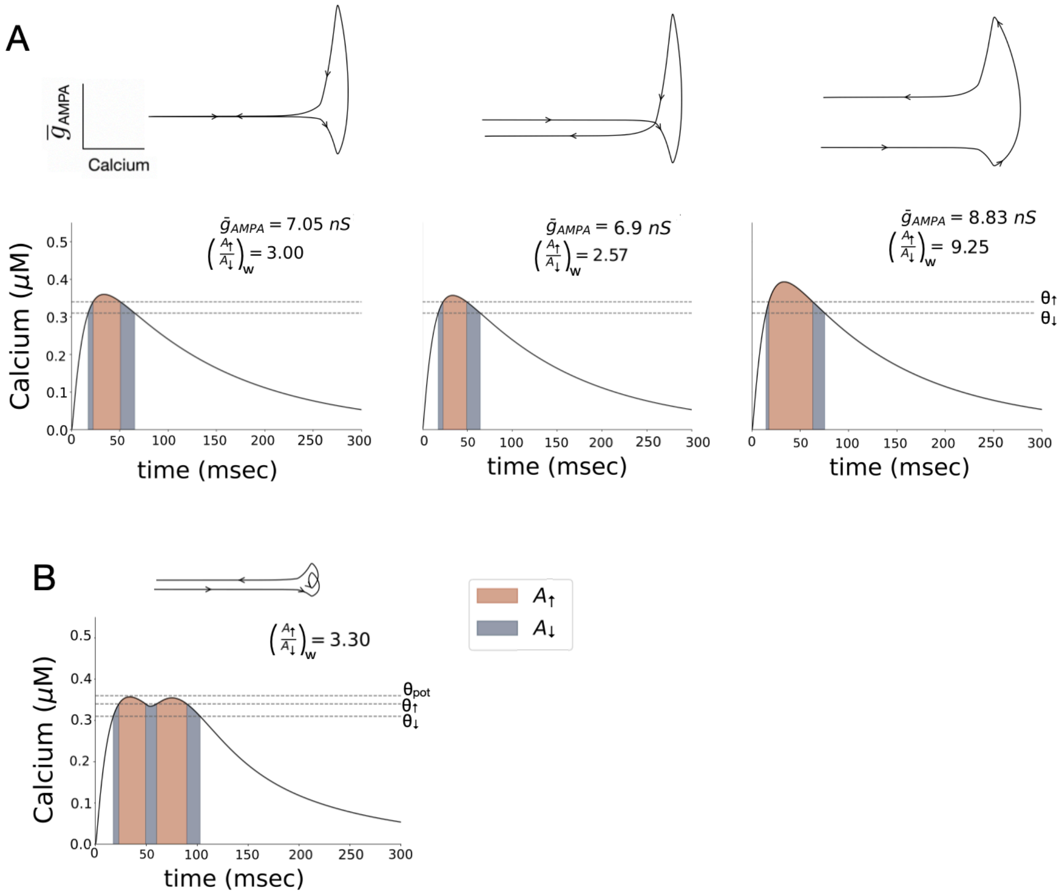

Figure 2.6: The weighted ratio $(\frac{A_\uparrow}{A_\downarrow})_w$ can accurately be used as a predictor of induction of depression or potentiation. **(A)** Different values of $\overline{g}_{AMPA}$ evoke different levels of depolarization and, consequently, different intracellular calcium concentrations. For a weighted ratio between the calcium area of AMPAR insertion and removal below 3.00, depression is induced. For a value above 3.00, potentiation is induced. **(B)** By adding a second source of calcium that becomes activated at t=80 msec, it is possible to have situations where the calcium never crosses the potentiation threshold θ_{pot} but potentiation is induced. The normalized ratio $(\frac{A_\uparrow}{A_\downarrow})_w$ accurately identifies these cases as potentiation. In these numerical simulations, E_D receives a pulse of glutamate followed by a pulse of GABA 2 msec after, each with an amplitude of 1mM and duration of 1 msec.

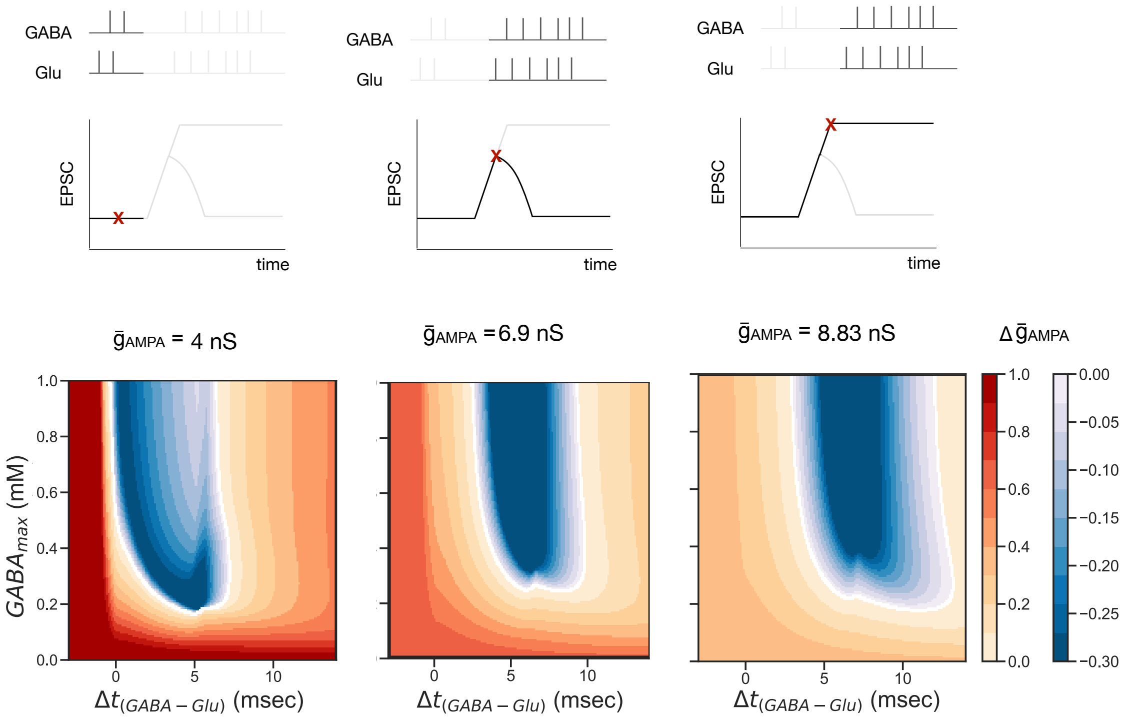

Figure 2.7: Amplitude of GABA pulse, $GABA_{max}$, and relative time between GABA and glutamate pulses, $\Delta t_{(GABA-Glu)}$, control direction and efficiency of induction of synaptic plasticity. **(A)** Depression and potentiation regions for $\overline{g}_{AMPA}$= 4 nS. This is the AMPAR's maximal conductance value used in our simulations before the disinhibition period starts. **(B)** Depression and potentiation regions for $\overline{g}_{AMPA}$= 6.9 nS, which represents the state of phosphorylation of the AMPAR at the end of the short disinhibition period. **(C)** Depression and potentiation regions for $\overline{g}_{AMPA}$= 8.83 nS, which is the state of phosphorylation of the AMPAR at the end of the long disinhibition period. For each plot (A), (B), and (C) we pair one pulse of glutamate (with a concentration of 1 mM and 1 msec of duration) with one pulse of GABA with a duration of 1 msec and varying concentrations and initial time, and measure the resultant change in $\overline{g}_{AMPA}$ for each case.

Model Predictions and implications:

Results of model simulations and analysis make several testable predictions. First, while experiments so far have not identified precisely the exact type of s.o. interneuron that provides feedforward inhibition to the CA1 pyramidal cell, our model predicts that it should be an interneuron with fast dynamics, i.e. with dynamics comparable to the pyramidal cells. More specifically, we expect hippocampal PV+ interneurons EPSCs in the stratum radiatum would decrease during cholinergic pairing due to the inhibition provided by the OLM neurons. Consequently, $GABA_A$-mediated IPSCs on the proximal dendrites of CA1 pyramidal cells would also decrease.

In this work (both in modeling and experimentally), modulation of the OLM cells is due to cholinergic activation of $\alpha7$ nAChRs. Our model more specifically suggests that the GABA release by the OLM cells is regulated by activating $\alpha7$ nACh receptors without necessarily altering the OLM firing. However, GABA release can also be controlled by the depolarization of the OLM cells and/or by modulation of their spiking activity by somatic nAChRs.

Our model predicts a relationship between the relative timing of the septal and hippocampal stimulus paring and the synaptic plasticity direction at the SC-PYR synapse. According to our simulations, increasing the frequency of septal and hippocampal paired stimulation can induce plasticity more efficiently, i.e., fewer pairings would be required to induce LTP. At the same time, we predict that changing the relative time between septal and hippocampal activation can induce LTD instead of LTP.

Finally, our modeling results suggest that for the plasticity to be induced, the excitatory NMDA and AMPA receptors and the inhibitory $GABA_A$ receptors should be located sufficiently proximal to each other in the pyramidal dendritic compartment.

2.4 Discussion

This work set out to explain how nicotinic cholinergic modulation of hippocampal OLM interneurons paired with hippocampal stimulation can potentiate CA1 pyramidal cell EPSC responses. Our modeling results suggest that co-pairing cholinergic activation of $\alpha7$ nAChRs on OLM interneurons results in the disinhibition of CA1 pyramidal cells. We also show by mathematical analysis how synaptic plasticity is controlled by the disinhibition of the postsynaptic pyramidal membrane through a disynaptic GABAergic circuit. To our knowledge, this is the first report to reveal how repeated disinhibition can directly induce LTP (both experimentally and computationally). It is also the first computational study that explicitly shows how cholinergic action on OLM interneurons can directly induce SC-CA1 plasticity through disinhibition.

OLM cells are a major class of GABAergic interneurons located in the stratum oriens hippocampal layer that inhibit pyramidal cells dendritic compartment located in the stratum lacunusom-moleculare layer, reducing the strength of EC inputs. OLM cells also target bistratified interneurons, expressing parvalbumin (PV) and somatostatin (Sst), that receive feedforward excitatory inputs from the Schaffer collaterals (Müller and Remy, 2014). Recent findings show that activation of OLM cells can facilitate LTP in the SC-CA1 pathway, likely by inhibiting s.r. interneurons that synapse on the same dendritic compartment as the SC, counteracting SC feedforward inhibition (R.Leão et al., 2012). We found that repeated pairing of cholinergic inputs with hippocampal stimulation can induce plasticity if the inputs are tightly timed. The time window for potentiation depends significantly on the dynamics of the O-cells, I-cells, and calcium dynamics. This agrees with experimental findings showing that activating cholinergic inputs to the hippocampus can directly induce different forms of synaptic plasticity depending on the hippocampus's input context, with a timing precision in the millisecond range (Gu and Yakel, 2011). Our model also shows that the longer the co-pairing period and the higher the frequency of stimulation during the co-pairing period, the longer lasting is the potentiation of the synapse.

According to our model, the key mechanism behind paired cholinergic induction of synaptic plasticity is the disinhibition of the pyramidal cell dendritic compartment. Cholinergic activation of the O-cell synapses inhibits the fast-spiking I-cell that projects to the dendritic compartment E_D. The disinhibition of E_D paired with glutamatergic stimulation allows for the depolarization of the pyramidal dendritic compartment. This increases NMDAR activation and intracellular calcium concentration sufficient to upregulate postsynaptic AMPAR permeability and potentiate the excitatory synapse.

Our model puts together the elements to give the following sequence of events: SC stimulation results in the activation of CA1 fast-spiking interneurons, I, and the subsequent release of GABA. At the same time, it evokes an EPSP mediated by AMPAR on the CA1 pyramidal cell dendritic compartment E_D. Since I and E_D have comparable dynamics, the EPSP is closely followed by a $GABA_A$-mediated IPSP. Because of slow kinetics and voltage-dependence, at that time, the NMDAR receptors are not in the open state and there is no influx of calcium. When the SC inputs are tightly timed with cholinergic inputs acting on OLM interneurons, GABA release from I-cells is suppressed. The pyramidal cell membrane at (or sufficiently near to) the glutamatergic synapse can depolarize enough to relieve the Mg^{2+} block from the NMDA receptors, allowing calcium to permeate through the receptor channel (Figure 2.8). Therefore, every time the pyramidal cell receives a glutamate pulse during the disinhibition period, the intracellular calcium concentration crosses the potentiation outset $\theta_{\uparrow}$, and $\overline{g}_{AMPA}$ increases.

Down-regulation of the GABAergic signaling during disinhibition leads to increased NMDAR activation. We see that when we reduced GABA concentration, glutamatergic activation of E_D results in postsynaptic NMDA currents with 7.90 pA of amplitude – with depolarization of -58.25 mV -, as opposed to the 6.75 pA that results from the pairing of glutamate and GABA inputs – with depolarization of -63.56 mV (see Figure S9). Because of the receptor's high calcium permeability, there is an elevation in intracellular calcium concentration large enough to initiate molecular mechanisms that result in the insertion/phosphorylation of the AMPAR. In our model, this translates into an increase in the AMPAR maximal conductance $\overline{g}_{AMPA}$. Moderate calcium concentrations, on the other hand, result in the removal of AMPARs. Because changes in calcium concentration are not instantaneous, the potentiation/depression of the synapse results from a balance between the insertion/removal of AMPARs during the period in which Ca concentration is above the

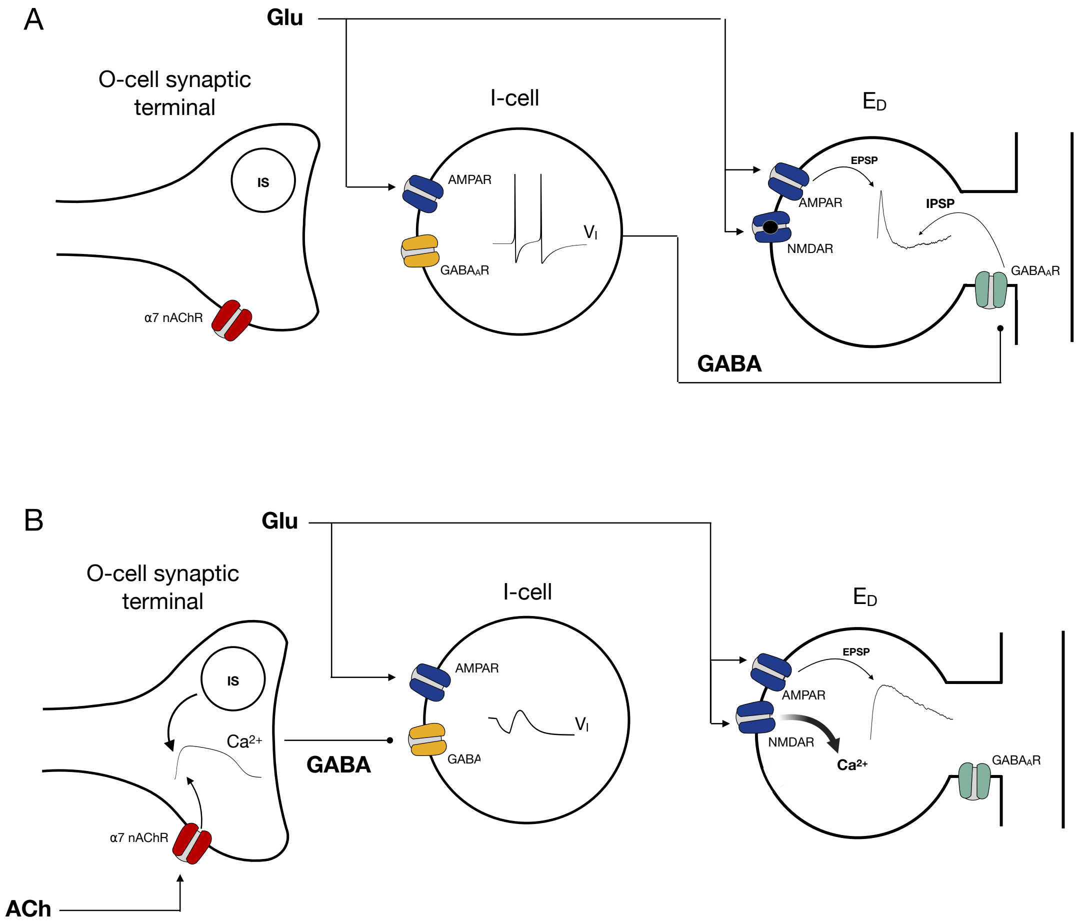

Figure 2.8: Scheme of the cholinergic and disinhibitory mechanisms that drive SC-CA1 potentiation. (A) Glutamatergic activation of I-cells lead to spiking activity and consequent GABA release. Subsequently, glutamate inputs acting on E_D evoke an EPSP mediated by AMPAR immediately followed by an IPSP mediated GABA acting on $GABA_A$ receptors. **(B)** Cholinergic activation of 7 nAChR on OLM interneuron initiates a CICR process mediated by calcium internal stores (IS). This results in GABA release that inhibits the I-cell. The dendritic compartment does not receive GABAergic inhibition. The dendritic compartment can depolarize enough - and remain depolarized for long enough - to relieve Mg^{2+} block from NMDA receptors, allowing calcium to permeate through the receptor channel.

potentiation/depression threshold. During disinhibition, this balance is positive and there is a total increase in $\overline{g}_{AMPA}$. The more times we pair disinhibition with SC stimulation, i.e., the longer the disinhibition period, the higher the value of $\overline{g}_{AMPA}$ by the end of the disinhibition period. After the disinhibition period, if the increase of $\overline{g}_{AMPA}$ was large enough, the calcium resultant from glutamatergic and GABAergic stimulation is such that there is a balance between potentiation and depression close to zero. That is, $\overline{g}_{AMPA}$ stabilizes by oscillating around the value of $\overline{g}_{AMPA}$ at the end of the disinhibition period (8.83 nS). Therefore, the synapse remains potentiated long after the disinhibition period is over. If there is no stimulation after the disinhibition period, $\overline{g}_{AMPA}$ slowly decays to its initial value (i.e., its value before the disinhibition period). Supposing that the increase of the AMPAR permeability is high enough, the potentiation of the excitatory synapse is maintained when the disinhibition period is over through repeated stimulation of the SC that keeps a balance between the down and upregulation of the AMPARs. This is in accordance with experimental results that show that repeated pairing of inhibition of Sst interneurons (that were not OLM) that target the CA1 pyramidal cell with SC stimulation can induce plasticity. Our model is robust to changes of parameters that maintain the same ratio of insertion/removal of AMPARs. Thus, for example, for different values of the $\gamma_{\uparrow}$, there is (at least) a pair of $\gamma_{\downarrow}$ for which our results remain the same (Figure S9). It is worth noting that the type of synaptic plasticity induced depends on the value of maximal conductance of the postsynaptic AMPAR, $\overline{g}_{AMPA}$, as shown in Figure **??**. Therefore, our model indicates that future changes in synaptic strength depend on previous plasticity events and how these changed $\overline{g}_{AMPA}$. This explains why, after the disinhibition period, pairs of glutamate and GABA pulses with the same characteristics will induce different results when the disinhibition period is short or long.

Earlier studies pointed out that reduced inhibition (disinhibition) can facilitate LTP induction under various conditions (Ormond and Woodin, 2009; Yang et al., 2016; Wigström and Gustafsson, 1983). Our results show that repeated temporally precise disinhibition can directly induce SC to CA1 LTP, providing a novel mechanism for inhibitory interneurons to modify glutamatergic synaptic plasticity directly. This expands the original spike-timing dependent plasticity that concerns the concurrent activation of two excitatory pathways to include the interneuron network.

Furthermore, our modeling work implies that GABAergic neurotransmission should control the local pyramidal voltage in the vicinity of the glutamatergic synapses. Thereby, the inhibitory synapses critically modulate excitatory transmission and the induction of plasticity at excitatory synapses. This points towards the importance of dendritic GABA and glutamate co-location in shaping local plasticity rules. Our work also suggests a cholinergic mechanism for controlling GABA release at the pyramidal dendrites and the subsequent potentiation of excitatory synapses, unraveling the intricate interplay of the hierarchal inhibitory circuitry and cholinergic neuromodulation as a mechanism for hippocampal plasticity.

Previous work by Gu and Yakel (2017) showed that co-paired activation of the cholinergic input pathway from the septum to the hippocampus with stimulation of the Schaffer collateral pathway could readily induce theta oscillations in a co-culture septal-hippocampal-entorhinal preparation. Moreover, after performing co-paired activation several times, not only was the SC-PYR synapse potentiated, but it became easier to evoke the theta rhythm in the preparation (one pulse stimulus of the SC is sufficient to generate theta oscillations in the circuit with the same characteristics as before). Therefore, induction of hippocampal plasticity, particularly potentiation of the CA1 EPSPs, appears to facilitate the generation of the theta rhythm. Moreover, recent studies directly linked OLMα2 interneurons to theta oscillations (Mikulovic et al., 2018), and suggest that OLM cells can regulate the robustness of the hippocampal theta rhythm (Chatzikalymniou and Skinner, 2018). Thus, we may speculate that the action of ACh on the α7 nAChRs at the OLMα2 neurons potentiates the SC-CA1 synapses to close the critical link in the synaptic chain of events, enabling recurrent reverberation of excitation in the hippocampal-entorhinal theta generating circuit. Understanding the mechanisms underlying the induction of hippocampal plasticity by this co-pairing mechanism will allow future studies of how changes on the synaptic level can propagate to the network level and change theta generation's mechanisms.

Our results are also relevant to understanding the neural circuit origins of pathological conditions and uncovering potential targets for therapeutic intervention in disorders linked to memory deficits. For example, the hippocampus is one of the earliest brain structures to develop neurodegenerative changes in Alzheimer's disease (AD) (Arriagada et al., 1992). Furthermore, numerous studies suggest that cognitive deficits in AD, such as memory impairment, are caused in part by cholinergic dysfunction action on hippocampal GABAergic interneurons (Schmid et al., 2016; Haam and Yakel, 2017). Here, we have shown that a decrease in the conductance of cholinergic $\alpha7$ nAChRs on OLM interneurons caused the impairment of induction of hippocampal synaptic plasticity.

A Calculating the weighted potentiation/depression area ratio $(A_\uparrow/A_\downarrow)_w$

While the calcium concentration is above the depression onset $\theta_\downarrow$ (but bellow the potentiation onset $\theta_\uparrow$), the maximal conductance of the AMPARs $\overline{g}_{AMPA}$ is decreasing. On the other hand, when the calcium concentration is above $\theta_\uparrow$, $\overline{g}_{AMPA}$ is increasing. The induction of plasticity at the excitatory synapse depends on the net result of these changes of $\overline{g}_{AMPA}$. The more time calcium spends above $\theta_\uparrow/\theta_\downarrow$, the more likely it is that potentiation/depression is induced at the synapse. Furthermore, the more time calcium spends above $\theta_\uparrow/\theta_\downarrow$, the bigger the area underneath the calcium curve in this region of insertion/removal of AMPARs. Therefore, the ratio between the area of insertion and the area of removal $(A_\uparrow/A_\downarrow)$ can be used as a measure of induction of plasticity. There is an optimal ratio for which the decrease of $\overline{g}_{AMPA}$ resultant from time spent in the removal region and the increase of $\overline{g}_{AMPA}$ resultant from time spent in the insertion region will cancel each other and no plasticity is induced. If the ratio $A_\uparrow/A_\downarrow$ is below this value, depression is induced; if the ratio is above this value, potentiation is induced. The ratio is $A_\uparrow/A_\downarrow$ is given by the following expression:

$$\frac{\int_{t_1}^{t_2} Cadt}{\int_{t_0}^{t_1} Cadt + \int_{t_2}^{t_3} Cadt} \qquad (26)$$

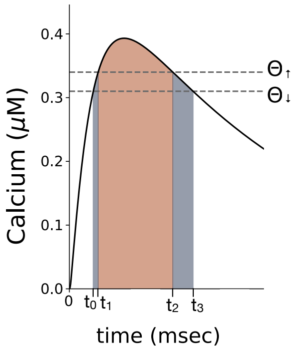

Because the decrease and increase of $\overline{g}_{AMPA}$ is not the same in the whole removal and insertion region, we need to calculate the calcium integral weighted by the calcium-dependent learning rate η. The normalized ratio $(A_\uparrow/A_\downarrow)_w$ is then given by $\frac{\int_{t_1}^{t_2} Ca.\eta dt}{\int_{t_0}^{t_1} Ca.\eta dt+\int_{t_2}^{t_3} Ca.\eta dt}$. To calculate $(A_\uparrow/A_\downarrow)_w$, we use the trapezoidal rule to perform numerical integration of the potentiation and depression area.

B A qualitative study of the synaptic profile of ACh

Not much is known about the ACh profile in the synaptic cleft upon release from cholinergic neurons; more specifically, not much is known about the time it decays for ACh to be broken down into choline and therefore, available to bind to cholinergic receptors. We have considered two different types of profiles for the ACh concentration in the synaptic cleft, and explored their validity for different parameters (amplitude, duration and decay time constant). We take into account the observations made by Gu and Yakel (2011) that pairing cholinergic inputs 10 msec prior to SC stimulation induces depression of the SC-CA1 synapse, while if the cholinergic inputs are activated 100 msec prior to SC stimulation, potentiation is induced. We pair one pulse of ACh with a square pulse of glutamate with a relative time of 10 and 100 msec, and measured the resultant changes in AMPAR conductance.

A square pulse of ACh followed by a pulse of glutamate 10 and 100 msec after will induce, respectively, depression and potentiation if the duration of the ACh pulse is equal or greater than the glutamate (even if the amplitude of ACh is smaller than the one of glutamate).

If Ach is described by an alpha function with an instantaneous rise time, the smaller the amplitude of the ACh pulse, the longer the decay time needs to be for the results to be in agreement with Gu and Yakel (2011) (for a same pulse duration of glutamate). If the duration of the glutamate pulse increases (decreases), we must also increase (decrease) the decay time of ACh (simulations not shown).

Please note that the decay and duration times, as well as the amplitude, of both the ACh and glutamate pulses serve merely as a guide as what types of neurotransmitters profiles we should consider. They are qualitative, and not quantitative, predictions of the synaptic profile of ACh.

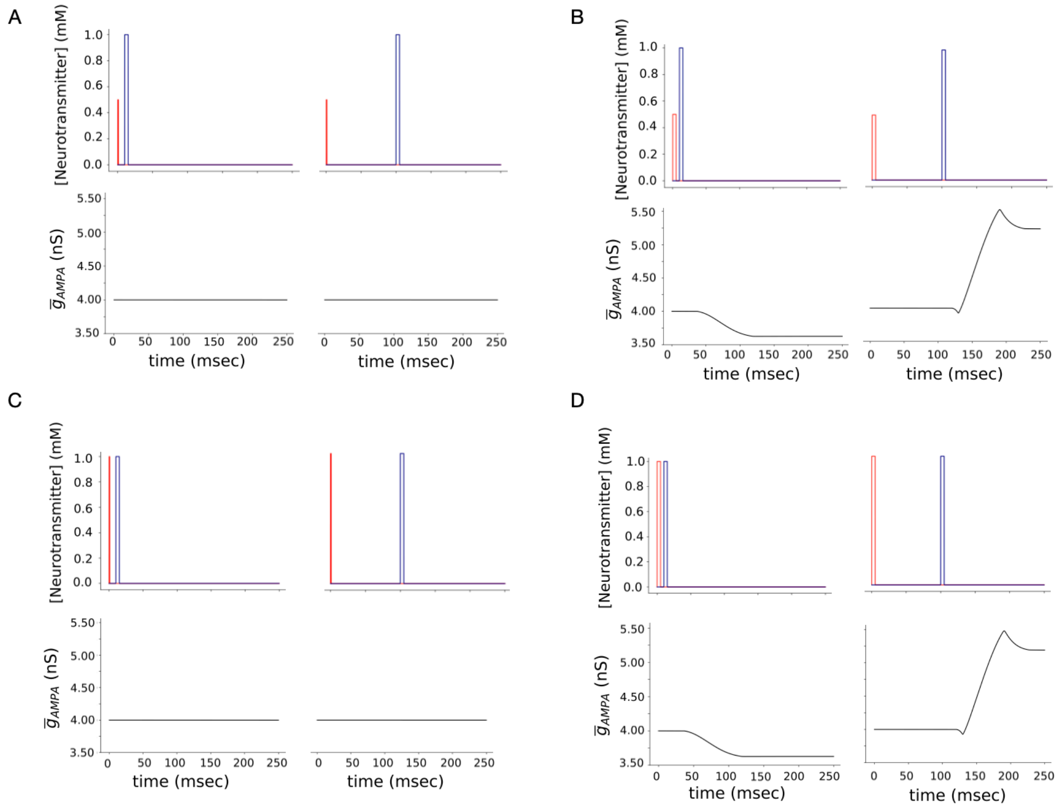

Figure S1: **(A)** One square pulse of ACh with a duration of 1 msec and concentration of 0.5 mM followed 10 msec after by a a square pulse of glutamate with a duration of 5 msec and an amplitude of 1 mM produces no changes in the maximal conductance of AMPAR, $\overline{g}_{AMPA}$ (left panel). Similarly, If the pulse of glutamate arrives 100 msec after, no changes are induced (right panel). **(B)** One square pulse of ACh with duration of 5 msec and concentration of 0.5 mM followed 10 msec after by a pulse of glutamate with a duration of 5 msec and 1 mM of concentration decrease $\overline{g}_{AMPA}$ (left panel). If the pulse of glutamate arrives 100 msec after, potentiation is induced (right panel). **(C)** One square pulse of ACh with a duration of 1 msec and concentration of 1 mM followed 10 msec after by a a square pulse of glutamate with a duration of 5 msec and an amplitude of 1 mM produces no changes in $\overline{g}_{AMPA}$ (left panel). Similarly, If the pulse of glutamate arrives 100 msec after, no changes are induced (right panel). **(D)** One square pulse of ACh followed 10 msec after by a pulse of glutamate with the same characteristics (duration of 5 msec and 1 mM of concentration) decrease $\overline{g}_{AMPA}$ (left panel). If the pulse of glutamate arrives 100 msec after, potentiation is induced (right panel).

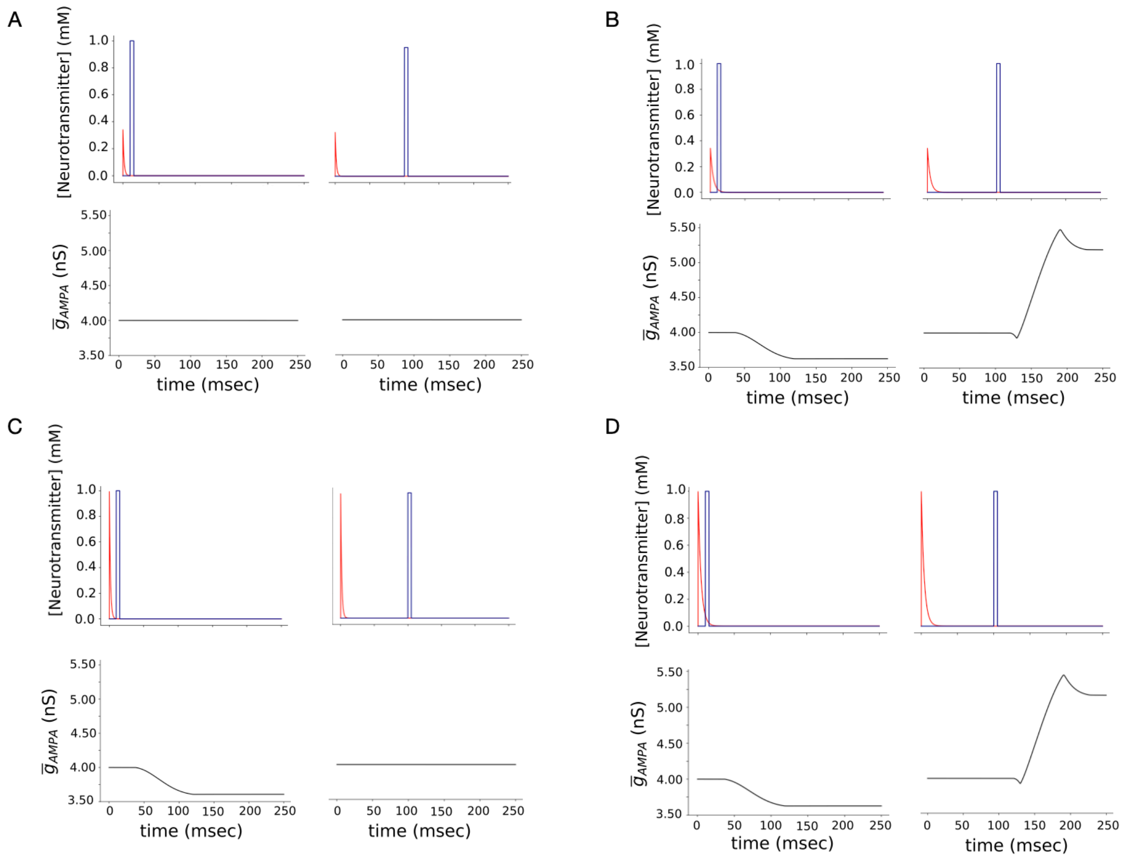

Figure S2: **(A)** One pulse of ACh with an amplitude of 0.39 mM, an instantaneous rise time and a decay time constant of 1 msec followed 10 msec after by a a square pulse of glutamate with 1 mM of amplitude and a duration of 5 msec induces no changes in $\overline{g}_{AMPA}$ (left panel). Similarly, if the pulse of glutamate arrives 100 msec after, no changes are induced (right panel). **(B)** One pulse of ACh with an amplitude of 0.39 mM, an instantaneous rise time and a decay time constant of 4 msec followed 10 msec later by a square pulse of glutamate depresses $\overline{g}_{AMPA}$ (left panel). If the pulse of glutamate arrives 100 msec after, potentiation is induced (right panel). **(C)** One pulse of ACh with an amplitude of 1 mM, an instantaneous rise time and a decay time constant of 1 msec followed 10 msec later by a square pulse of glutamate with the same amplitude and duration of 5 msec provokes a decrease in $\overline{g}_{AMPA}$ (left panel). If the pulse of glutamate arrives 100 msec after, no changes are induced (right panel). **(D)** One pulse of ACh with an amplitude of 1 mM, an instantaneous rise time and a decay time constant of 4 msec followed 10 msec later by a square pulse of glutamate depresses $\overline{g}_{AMPA}$ (left panel). If the pulse of glutamate arrives 100 msec after, potentiation is induced (right panel).

C Supplementary Figures

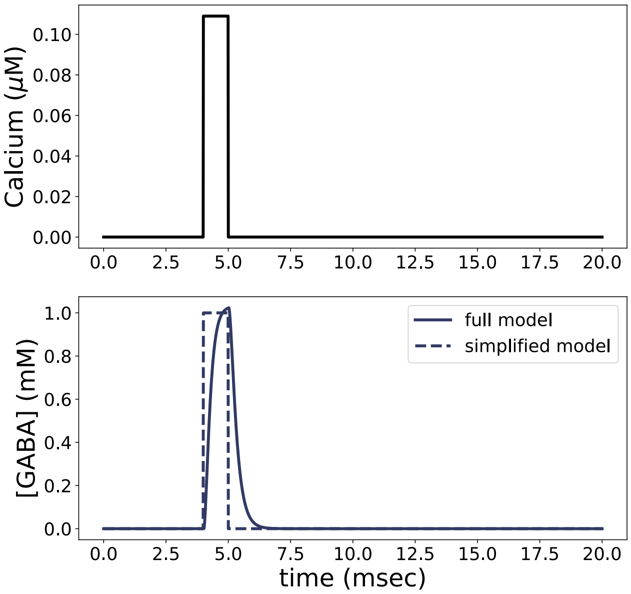

Figure S3: GABA concentration elicited by a calcium pulse of 0.10 μM of amplitude and 1 msec of duration computed using the detailed model of transmitter release described in Destexhe et al. (1998) and using equation (2.16).

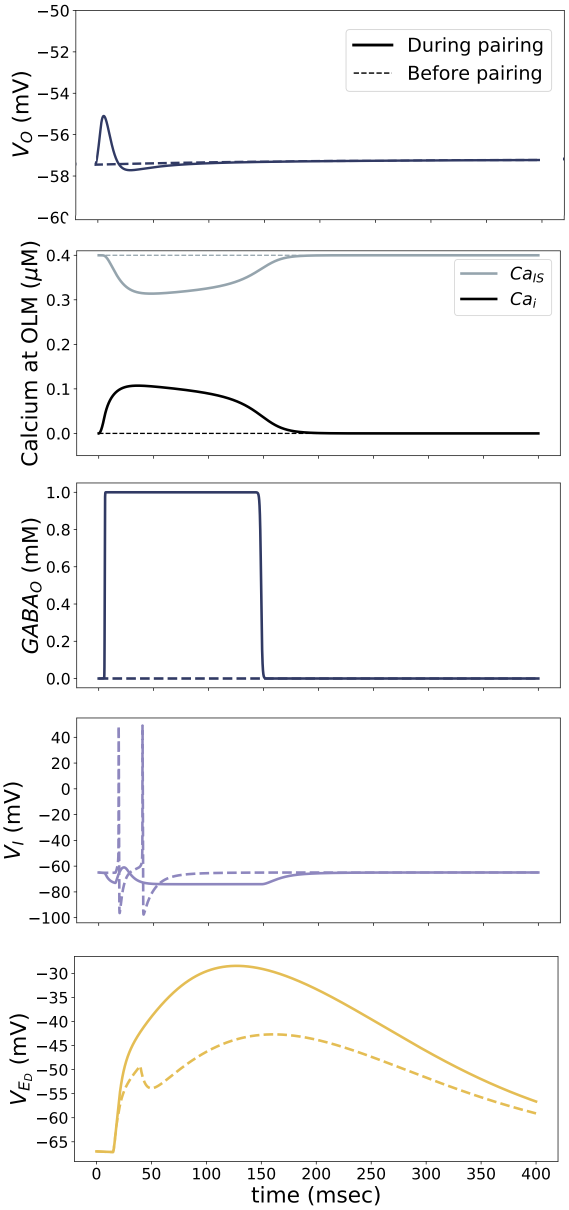

Figure S4: Before co-pairing, the network only receives one pulse of glutamate. The $\alpha7$ nAChR at OLM are not activated, there are no changes in the intracellular calcium concentration (Ca_i) and, consequently, no GABA is released ($GABA_O$). Glutamatergic activation of the I-cell result in two spikes, and the I-cell inhibits E_D that cannot depolarize enough. During co-pairing, $\alpha7$ nAChR activation increases the intracellular concentration Ca_i. $GABA_O$ is released from the OLM cell and inhibits the I-cell. E_D does not receive inhibition, only excitation from glutamatergic stimulation and depolarizes.

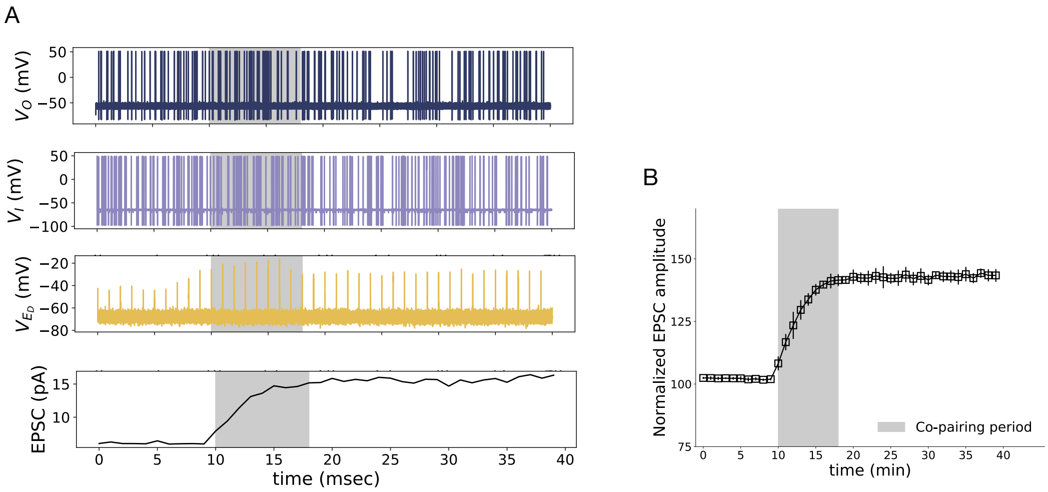

Figure S5: **(A)** Time evolution of of the membrane potential of the O-cell, I-cell and E_D with white noise when cholinergic inputs are paired with SC inputs, and resultant EPSC. **(B)** Mean trace of normalized EPSC after 10 simulations. Adding a noisy background current to the O and I-cell induces spontaneous spiking. Co-pairing cholinergic and glutamatergic inputs from t=10 min to t=18 min induces potentiation of the pyramidal cell EPSC. In this simulations the parameter ξ’ was adjusted from 2.1 × 10^{-6} mM/(msec pA) to 3× 10^{-6} mM/(msec pA), keeping the intracellular calcium concentration in the O-cell within the physiological range. The O-cell releases GABA when the intracellular calcium concentration is high enough (see equation (2.16)), and when the cell spikes (see equation (2.15)). All the remaining parameters are identical to the ones used to produce Figure 2.2. Noise was incorporated by adding a stochastic term $\sqrt{dt}\zeta$, where ζ a random Gaussian variable with mean $\mu = 0$ and standard deviation σ(=1.1, 0.1 and 0.3 for the O, I and E_D cells respectively), to the Euler equations describing the evolution of the membrane potential V_x. Normalization of the results was calculated according with the expression (100 + (EPSC - $EPSC_{min}$).(150-100))/($EPSC_{max}$ - $EPSC_{min}$).

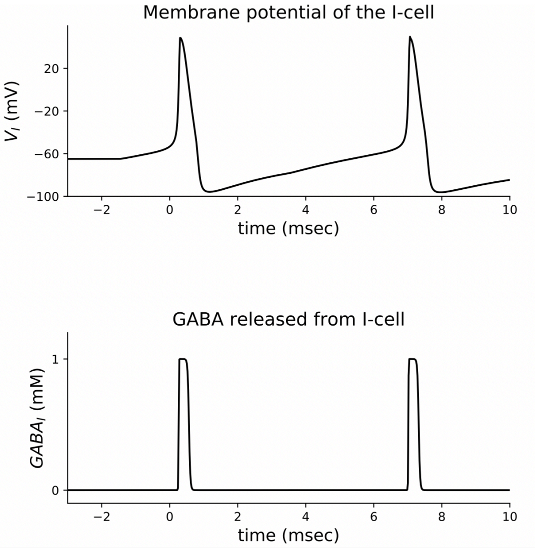

Figure S6: Membrane potential of the I-cell when it receives two pulses of glutamate (with amplitude 1mM and duration of 3 msec) with a frequency of 0.2 $msec^{-1}$, and respective GABA release. GABA concentration can be described by a square function.

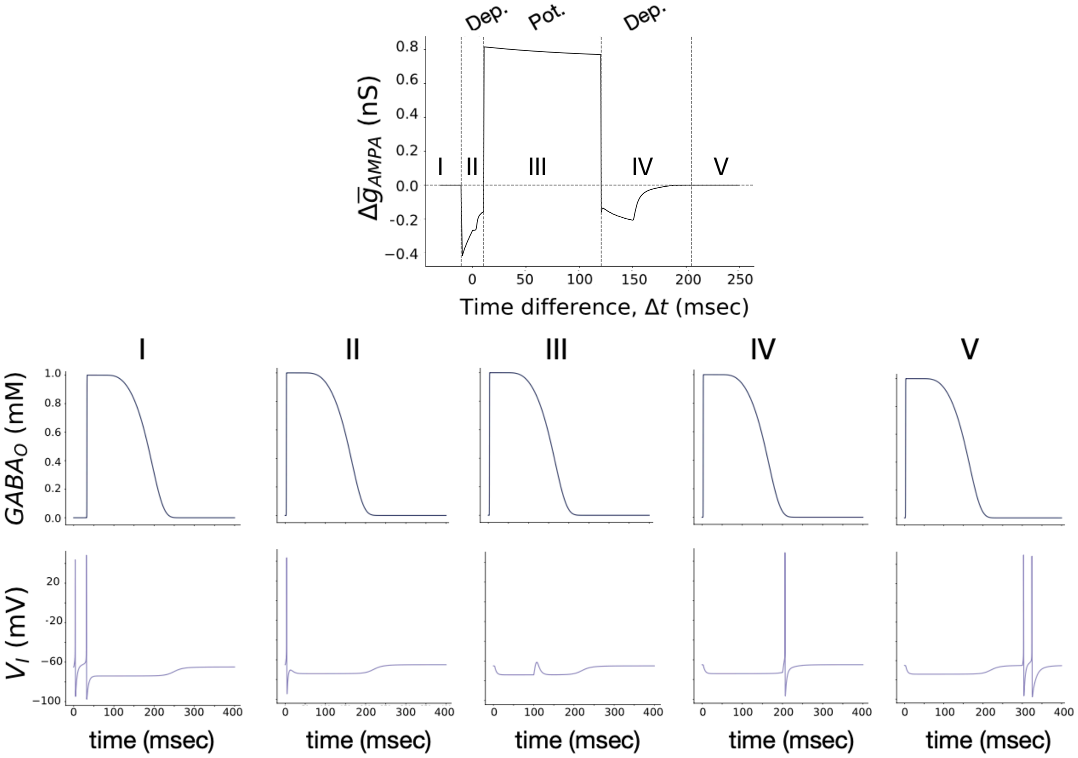

Figure S7: Tightly timed pairing of cholinergic to glutamatergic inputs can cancel the I-cell feedforward inhibition. For Δt = -30 msec (Region I), a pulse of glutamate activates the I-cell. When the OLM cell receives a pulse of ACh 30 msec after and releases GABA, the I-cell already emitted two spikes and inhibit E_D − no plasticity is induced. . For Δt =0 msec (Region II), the I-cell and OLM receive a pulse of glutamate and ACh, respectively, simultaneously. Due to its fast dynamics, the I-cell manages to emit one spike before being inhibited by $GABA_O$. The I-cell inhibits E_D only moderately – depression is induced. For Δt = 100 msec (Region III), OLM receives an ACh pulse at t=0 msec and releases $GABA_O$ into the I-cell. When the I-cell receives glutamate 100 msec after, it is hyperpolarized and cannot spike – potentiation is induced. For Δt = 200 msec (Region IV), the hyperpolarization of the I-cell is starting to wear off and the cell manages to emit one spike, sending moderate inhibition to E_D – depression is induced. For Δt = 300 msec (Region V), the I-cell can emit two spikes when it receives glutamate 300 msec after cholinergic activation – no plasticity is induced.

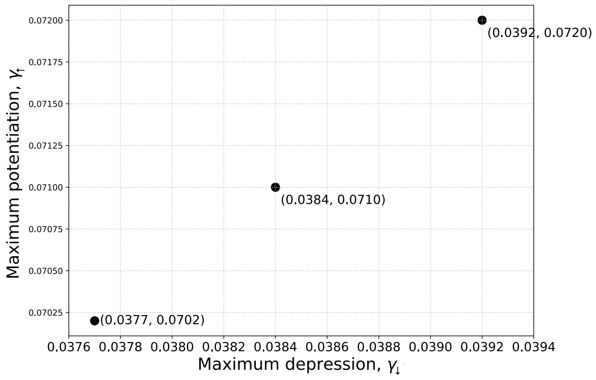

Figure S8: Sets of parameters for which we obtain the same results as the ones shown in Figure 2.4

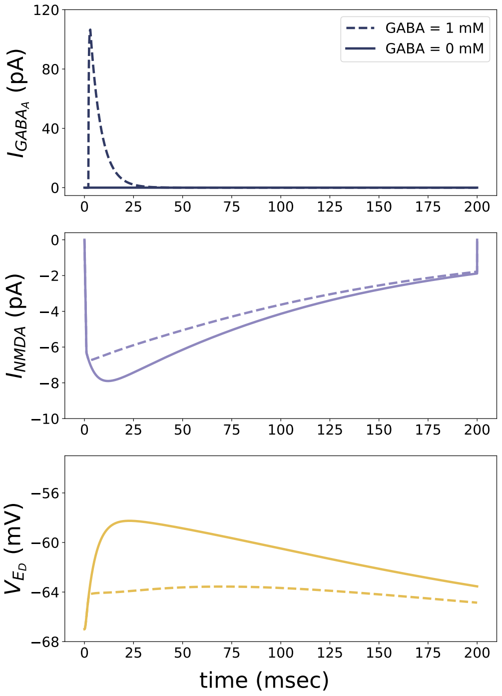

Figure S9: One pulse of GABA with 1 mM of amplitude and 1 msec of duration evokes an inhibitory $GABA_A$ current at E_D (I_{GABA_A}). Glutamatergic activation of E_D only evokes a depolarization of -63.56 mV and, consequently, an NMDA current I_{NMDA} of 6.75 pA. When E_D does not receive GABA inputs, glutamate inputs evoke a depolarization of -58.25 mV, and the resultant NMDA current has an amplitude of 7.90 pA.

Part II

Theta rhythm generation

3 | Exact reduction for networks of neurons with complex dynamic phenotypes

3.1 Introduction

For decades, neuroscientists have been using mean-field theory to reduce the description of neural circuits composed of many interacting neurons to a low-dimensional system that describes the macroscopic dynamical states of the network. This approach generates a reduced picture of the neural population that can be used to study how brain functions arise from the collective behavior of spiking neurons.

Montbrió et al. (2015) pioneered an exact mean-field approach to link the microscopic dynamics of the individual neurons to the macroscopic state of large neural networks in terms of the firing rate and mean voltage. However, this approach was limited to networks of one-dimensional quadratic integrate-and-fire (QIF) neurons that cannot account for complex spiking and bursting dynamics.

Two-dimensional quadratic integrate-and-fire models (e.g., the Izhikevich neuron model (Izhikevich, 2003)) reproduce a wide variety of spiking and bursting behaviors. An exact mean-field reduction of such neuron models will enable us to derive the macroscopic dynamics of populations of neurons with any kind of spiking properties. In other words, it would allow us to use techniques of dynamical systems theory to study the underlying mechanisms that lead to the emergence of specific population behaviors, such as neural oscillations. Despite recent advances (di Volo et al., 2019; Nicola and Campbell, 2013), exact analytical mean-field reduction methods for two-dimensional QIF are still lacking.

In this chapter, we derive a macroscopic exact-reduction (ER) description for large networks of conductance-based interacting Izhikevich neurons. We start by presenting the two-dimensional QIF neuron model we will use to describe the neurons in our population. We then show how a separation of time scales of the variables describing the state of the neurons allows us to explicitly solve the continuity equation of the system, which represents the evolution of the state of the neural population. By doing so, we obtain a system of two coupled variables, the firing rate and the mean voltage, which together describe the evolution of the macroscopic system. We support our findings with extensive numerical evidence involving simulation of finite-size networks of neurons with different spiking properties compared with the respective reduced system. This approach opens the possibility of generating realistic mean-field models from electrophysiological recordings of individual neurons and can be used to relate the biophysical properties of neurons with emerging behavior at the network scale.

3.2 Methods

3.2.1 Population model of coupled QIF neurons

We derive a mean-field model for populations of coupled Izhikevich neurons. Each neuron i from a population W is described by a fast variable representing the membrane potential, V (mV), and a slow variable representing the recovery current, u (pA):

$$C_m \frac{dV_i^W}{dt} = a(V_i^W - V_r)(V_i^W - V_t) - u_i^W + I_i \tag{3.1a}$$

$$\frac{du_i^W}{dt} = \alpha(\beta(V_i^W - V_r) - u_i^W) \tag{3.1b}$$

where the onset of an action potential is taken into account by a discontinuous reset mechanism:

$$If\ V_i^W > V_{peak} \Rightarrow V_i^W \leftarrow V_{reset},\ u_i^W \leftarrow u_i^W + u_{jump}$$

The parameteres are as follows: C_m stands for the membrane capacitance, V_r is the resting potential, V_t the threshold potential, a is a scaling factor, α the time constant of the recovery variable u, β modulates the sensitivity of the recovery current to subthreshold oscillations, and I_i is the total current acting on neuron i. We consider $I_i = \eta_i + I_{ext} + I_{syn,i}$. The parameter η_i represents a background current. To account for the network heterogeneity, the parameter η_i is randomly drawn from a Lorentzian distribution with half-width Δ centered at $\overline{\eta}$, $g(\eta) = \frac{1}{\pi}\frac{\Delta}{(\eta-\overline{\eta})^2+\Delta^2}$. I_{ext} is an external current acting on population W (identical to all neurons). $I_{syn,i}$ is the total synaptic current acting on neuron i given by:

$$I_{syn,i} = \sum_Z s_{WZ}(E_r^Z - V_i^W) \tag{3.2}$$

where E_r^Z is the reversal potential of the synapse, and s_{WZ} the synaptic conductance. If we assume that all neurons of population W are connected to all neurons of population Z, the synaptic conductance s_{WZ} can be described according to the following equation:

$$\frac{ds_{WZ}}{dt} = -\frac{s_{WZ}}{\tau_s} + \frac{p_{WZ}}{N_Z} \sum_{k=1}^{N_Z} \sum_f \delta(t - t_f^k) \tag{3.3}$$

where δ is the Dirac mass measure and t_f^k is the firing time of neuron k. The parameter τ_s represents the synaptic time constant, N_Z is the number of neurons of population Z, and p_{WZ} is the coupling strength of population Z on population W.

3.3 Results

3.3.1 Adiabatic approximation of the two-dimensional QIF neuron model

We exploit the time scales difference between the dynamics of the membrane potential V and the recovery variable u to reduce the dimensionality of the neural network. If the time scale of the recovery variable is much slower than the other variables, we can invoke an adiabatic approximation by considering that all neurons of population W receive a common recovery variable u^W. This results in the modified Izhikevich QIF model:

$$C_m \frac{dV_i^W}{dt} = a(V_i^W - V_r)(V_i^W - V_t) - u^W + I_i \tag{3.4}$$

$$\frac{du^W}{dt} = \alpha(\beta(\langle V \rangle^W - V_r) - u^W) + u_{jump} \sum_{k=1}^{N_W} \sum_f \delta(t - t_f^k) \tag{3.5}$$

where $\langle V \rangle^W$ is the mean membrane potential of the population W, described as follows:

$$\langle V \rangle^W = \frac{\sum_{k=1}^{N_W} V_k^W}{N_W} \tag{3.6}$$

Note that we have incorporated the resetting mechanism of the variable u^W in the last term of equation (3.5). The onset of an action potential is now described by:

$$V_i^W > V_{peak} \Rightarrow V_i^W \leftarrow V_{reset}$$

From now on we will consider equation (3.4) written in terms of the parameters $b = a(-V_r - V_t)$ and $c = aV_rV_t$:

$$C_m \frac{dV_i^W}{dt} = a(V_i^W)^2 + bV_i^W + c - u^W + \eta_i + \sum_Z s_{WZ}(E_r^Z - V_i^W) + I_{ext} \tag{3.7}$$

The main consequence of the adiabatic approximation is the reduction in the number of state variables describing a neuron in the population from (V_i^W, u_i^W) to (V_i^W). This is a crucial step in our method since it enables us to solve the continuity equation of the system analytically, as we demonstrate in the next section.

3.3.2 Mean-field reduction

In the mean-field limit, a population of neurons is well represented by its probability density function, ρ. This function represents the proportion of neurons that are in a particular state at time t. In our case, the state of a neuron is fully described by its membrane potential. We denote $\rho(V^W|\eta, t)$ as the probability of finding a neuron from population W with voltage V at time t, knowing that its intrinsic parameter is η. Defining the flux $J(V|\eta, t)(= \frac{dV}{dt}\rho(V|\eta, t))$ as the net fraction of trajectories per time unit that crosses the value V, we can write the continuity equation

$$\frac{\partial}{\partial t}\rho(V|\eta, t) = -\frac{\partial}{\partial V}J(V|\eta, t) \tag{3.8}$$

which expresses the conservation of the number of neurons. Note that in integrate-and-fire models, the number of trajectories is not conserved at $V = V_{reset}$ and $V = V_{peak}$. By taking V_{reset} and V_{peak} to infinity, we ensure that the boundary conditions are the same and that the number of trajectories is conserved [1].

According to the Lorentzian ansatz (LA) (Montbrió et al., 2015), solutions of the

---

[1] By considering V_{peak} = - $V_{reset} = \infty$, the resetting rule still captures the spike reset as well as the refractoriness of the neurons.

continuity equation (3.8) for a population of QIF neurons converge to a Lorentzian-shaped function with half-width $x(\eta, t)$ and center at $y(\eta, t)$ of the form:

$$\rho(V^W|\eta, t) = \frac{1}{\pi} \frac{x(\eta, t)}{[V - y(\eta, t)]^2 + x(\eta, t)^2} \tag{3.9}$$

We discuss the validity of the LA here applied in appendix A. Here, $x(\eta, t)$ and $y(\eta, t)$ are statistical variables that represent the low dimensional behavior of the probability density function ρ. Adopting the LA, we obtain the low dimensional system:

$$C_m \frac{\partial x(\eta, t)}{\partial t} = (b - \sum_Z s_{WZ})x + 2axy \tag{3.10}$$

$$C_m \frac{\partial y(\eta, t)}{\partial t} = -ax^2 + ay^2 + (b - \sum_Z s_{WZ})y + c - u^W + I_{ext} + \sum_Z s_{WZ} E_r^Z + \eta \tag{3.11}$$

that can be written in the complex form as:

$$C_m \frac{\partial w(\eta, t)}{\partial t} = i(-aw^2 + c - u + I_{ext} + \sum_Z s_{WZ} E_r^Z + \eta) + (b - \sum_Z s_{WZ})y)w \tag{3.12}$$

with $w(\eta, t) = ix(\eta, t) + y(\eta, t)$

3.3.3 The macroscopic variables: firing rate and mean voltage

The firing rate is obtained by summing the flux for all η at $V = V_{peak}$. Taking $V_{peak} \to \infty$ the firing rate of a population W is defined as follows

$$r_W(t) = lim_{V\to\infty} \int J(V^W|\eta, t)g(\eta)d\eta \tag{3.13}$$

The mean voltage of the population is obtained by integrating the probability density function ρ for all V and η values:

$$v_W(t) = \int \int \rho(V^W|\eta, t) g(\eta) dV^W d\eta \tag{3.14}$$

Adopting the solution for the continuity equation (3.9) and inserting it into equations 3.13 and 3.14 we have that the phenomenological variables x and y relate with the firing rate, r, and mean voltage, v, as follows:

$$r_W(t) = \frac{a}{C_m \pi} \int x(\eta, t)(g(\eta)) d\eta \tag{3.15}$$

$$v_W(t) = \int \int \frac{x(\eta, t)}{\pi} \frac{V^W(t)}{(V^W(t) - y(\eta, t))^2 + x(\eta, t)^2} g(\eta) dV^W d\eta \tag{3.16}$$

To avoid indeterminancy of the improper integral, we resort to the Cauchy principal value to evaluate the integral 3.16 ($p.v. \int_{-\infty}^{+\infty} h(x)dx = lim_{R\to\infty} \int_{-R}^{R} h(x)dx$). In the case of a Lorentzian distribution, the principal value is given by $p.v. \int_{-\infty}^{+\infty} \frac{\sigma}{\pi} \frac{x}{(x-x_0)^2+\sigma^2} dx = x_0$. We then have that the mean voltage is given by:

$$v_W(t) = \int g(\eta) p.v. \int \frac{x}{\pi} \frac{V^W}{(V^W - y)^2 + x^2} dV^W d\eta \tag{3.17}$$

$$= \int g(\eta) y d\eta \tag{3.18}$$

As previously mentioned, in the mean-field limit, the probability distribution function $g(\eta)$ is given by

$$g(\eta) = \frac{1}{\pi} \frac{\Delta}{(\eta - \overline{\eta})^2 + \Delta^2} = \frac{1}{\pi} \frac{\Delta}{(\eta - (\overline{\eta} + i\Delta))(\eta - (\overline{\eta} - i\Delta))}$$

The distribution $g(\eta)$ has poles at $\eta - i\Delta$ and $\eta + i\Delta$, and can be written as

$$g(\eta) = \frac{1}{2\pi i} \left(\frac{1}{\eta - (\overline{\eta} + i\Delta)} - \frac{1}{\eta - (\overline{\eta} - i\Delta)}\right)$$

The integrals in equations 3.15 and 3.18 are evaluated by closing the integral contour in the complex η plane and using the residue theorem. We then have that the firing rate and mean potential relate to the Lorentzian coefficients x and y according to the following expression:

$$r_W(t) = \frac{a}{C_m \pi} x(\overline{\eta} \pm i\Delta, t) \tag{3.19}$$

$$v_W(t) = y(\overline{\eta} \pm i\Delta, t) \tag{3.20}$$

Given equations 3.19 and 3.20 and noting that

$$C_m \frac{dx(\overline{\eta} \pm i\Delta, t)}{dt} = (b - \sum_Z s_{WZ})x + 2axy - (\pm\Delta) \tag{3.21}$$

$$C_m \frac{dy(\overline{\eta} \pm i\Delta, t)}{dt} = -ax^2 + ay^2 + c - u + (b - \sum_Z s_{WZ})y + I_{ext} + \overline{\eta} \tag{3.22}$$

we have that the continuity equation reduces to the low-dimensional macroscopic dynamical system:

$$C_m \frac{dr}{dt} = (b - \sum_Z s_{WZ})r_X + 2arv - (\pm\Delta)\frac{a}{C_m \pi}$$

$$C_m \frac{dv}{dt} = -\frac{C_m^2 \pi^2}{a} r^2 + av^2 + c - u + bv_X + I_{ext} + \overline{\eta}$$

Since the firing rate always has to be non-negative, we needed to evaluate the closed integral contour containing the pole of $g(\eta)$ in the lower half of η plane, i.e., $\overline{\eta} - i\Delta$. Until now, we considered the integral contour in both the upper and lower half of the η. This is because the Lorentzian variables x and y have no physical meaning. Therefore we could not make any conclusions regarding which contour to consider when using the residue theorem to solve (3.15) and (3.18) until now.

We have that an exact mean-field reduction of a population of interacting conductance-based Izhikevich two-dimensional QIF neurons is given by :

$$
\begin{aligned}
C_m \frac{dr_W}{dt} &= (b - \sum_Z s_{WZ}) r_W + 2a r_W v_W + \Delta \frac{a}{C_m \pi} && \text{(3.23a)} \\
C_m \frac{dv_W}{dt} &= -\frac{C_m^2 \pi^2}{a} r_W^2 + a v_W^2 + c - u^W + (b - \sum_Z s_{WZ}) v_W + \\
&\qquad I_{ext} + \sum_Z E_r^Z + \overline{\eta} && \text{(3.23b)} \\
\frac{du^W}{dt} &= \alpha(\beta(v^W - V_r) - u^W) + u_{jump} r_W && \text{(3.23c)} \\
& && \text{(3.23d)}
\end{aligned}
$$

with

$$
\frac{ds_{WZ}}{dt} = -\frac{s_{WZ}}{\tau_s} + p_{WZ} r_Z \qquad (3.24)
$$

3.3.4 Numerical simulations

The Izhikevich two-variable QIF model can, with the adequate choice of parameters, reproduce many of the key features of firing patterns observed in neurons, such as tonic spiking, subthreshold oscillations, and bursting (Izhikevich, 2003). We apply the exact reduced system 3.23 described in the previous section to populations of neurons with different firing dynamics and compare the resultant population activity with direct simulations of QIF neurons to explore the versatility of the model.

Figure 3.1 illustrates a comparison of the dynamics of the full network of Izhikevich QIF neurons with its corresponding reduced system. Regarding the full system, each population is made up of $N = 3000$ neurons. The neurons are described by the two-dimensional QIF model 3.1, with the respective parameters specified in Table 3.1. The firing rate is calculated according to:$r(t) = \frac{1}{N} \sum_{k=1}^{N} \sum_f \delta(t - t_f^k)$. For the reduced system, the firing rate is calculated according to equation 3.23a. The reduced description closely follows the firing activity of the full network for all populations.

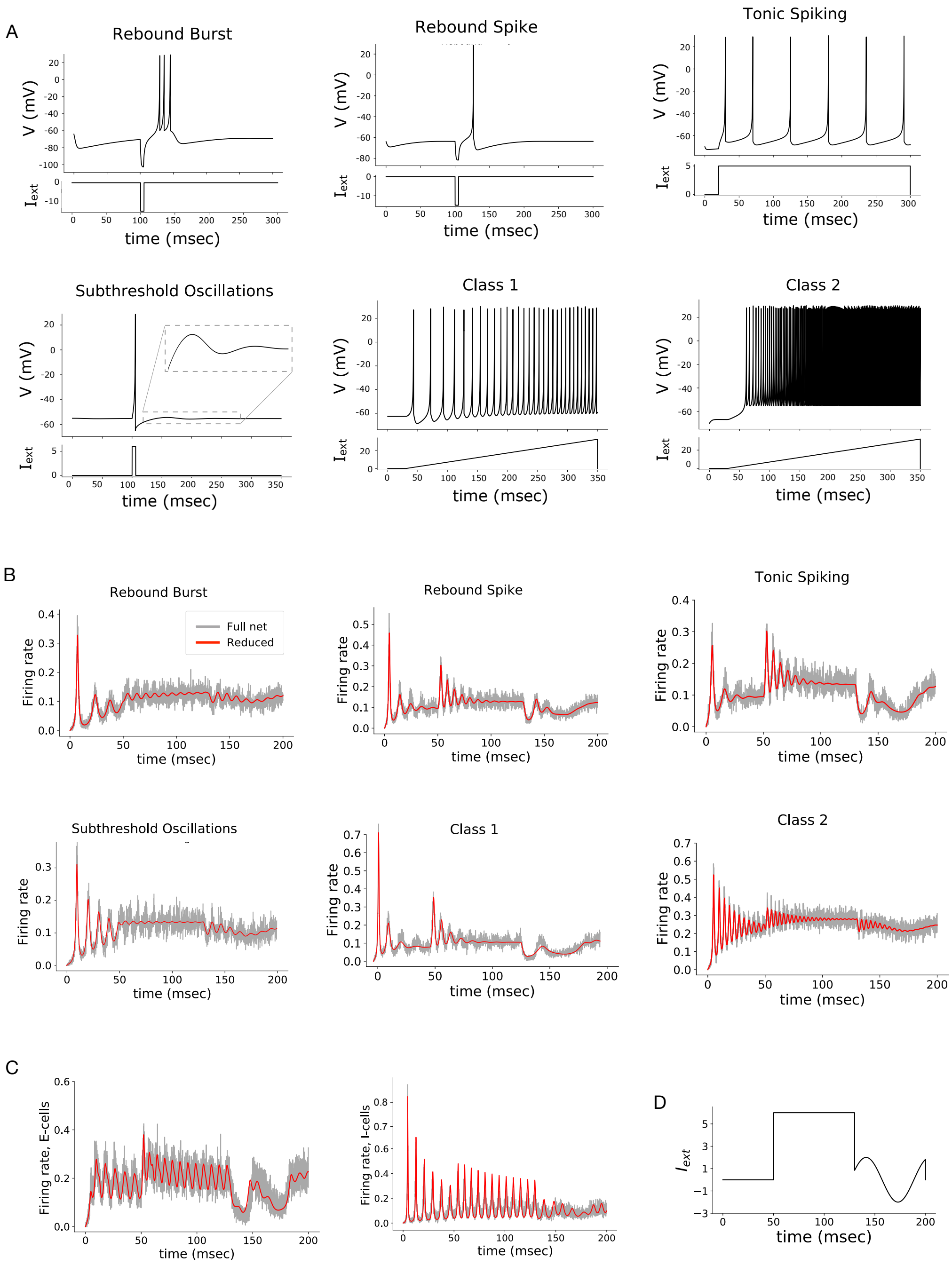

Figure 3.1: Comparison between the full network and exact reduced system for networks of neurons with distinct dynamics. (A) Membrane potential of spiking neurons with different spiking features. Results were obtained using the Izhikevich two-dimensional QIF neuron model Izhikevich (2003) with the adequate choice of parameters (see Table 3.1). **(B)** Firing rate of populations of uncoupled neurons with different dynamics obtained from simulations of the full and reduced system, and respective external current. (*caption continues on next page*)

(C) Firing rate of a population of recurrently connected excitatory tonic spiking cells (E) and inhibitory neurons with subthreshold oscilations (I). **(D)** External current acting on all neuronal populations. Parameters: $\Delta = 1$, $\overline{\eta} = 15$, $N = 3000$, $p_{EE} = 1$, $p_{EI} = p_{IE} = 1$, $p_{II} = 2$, $\tau_s = 1$.

	Rebound		**Tonic**		**Class**		
	Burst	**Spike**	**Bursting**	**Spiking**	**1**	**2**	**Sub. Osc.**
a (mS/cm^2mV)	0.04	0.04	0.04	0.04	0.04	0.04	0.0454
b (mS/cm^2)	5.3	4.99	4.88	4.93	4.96	4.98	5.02
c $(mS/(cm^2mV))$	174	154	148.2	152	154	155	137.76
C_m $(\mu F/cm^2)$	1	1	1	1	1	1	2
V_r (mV)	-65	-56	-65	-60	-65	-65	-60
α $(msec^{-1})$	0.01	0.03	0.02	0.02	0.02	0.2	0.05
β (mS/cm^2)	0.9	0.25	0.32	0.2	0.1	0.26	1.1
u_{jump} $(\mu A/cm^2)$	0	4	0	2	4	0	0
V_{peak} (mV)	30	30	30	30	30	30	30
V_{reset} (mV)	-60	-60	-55	-60	-60	-55	-55

Table 3.1: Parameter values of two-dimensional QIF neuron model for neurons displaying different firing properties. Parameters adapted from Izhikevich (2003).

3.3.5 Limitations of reduction formalism

One crucial assumption of the mean-field reduction formalism here presented is the slow dynamics of the recovery variable u. However, every time a neuron reaches V_{peak}, the membrane potential V is reset to V_{reset} and the recovery variable u is instantaneously increased by u_{jump}, adding a discontinuity to the system. Given that the adiabatic approximation made in section 3.3.1 relies on the assumption that the variable u is the slowest variable in the system and that therefore we can consider that all the neurons in the population receive a variable u with approximately the same value, adding an instantaneous jump invalidates the approximation made. The highest the jump, the more evident this is. In the examples considered in Figure 3.1, u_{jump} is small enough to describe the activity of all populations accurately. This means the reduced system here derived can be used to study the activity of populations with any of the spiking dynamics portrayed in Figure 3.1. Still, it may not be adequate to describe the activity of specific populations of neurons found in the brain that require a big u_{jump} value to describe their dynamics accurately. This is the case for rat spiny projection neurons of the neostriatum and basal ganglia.

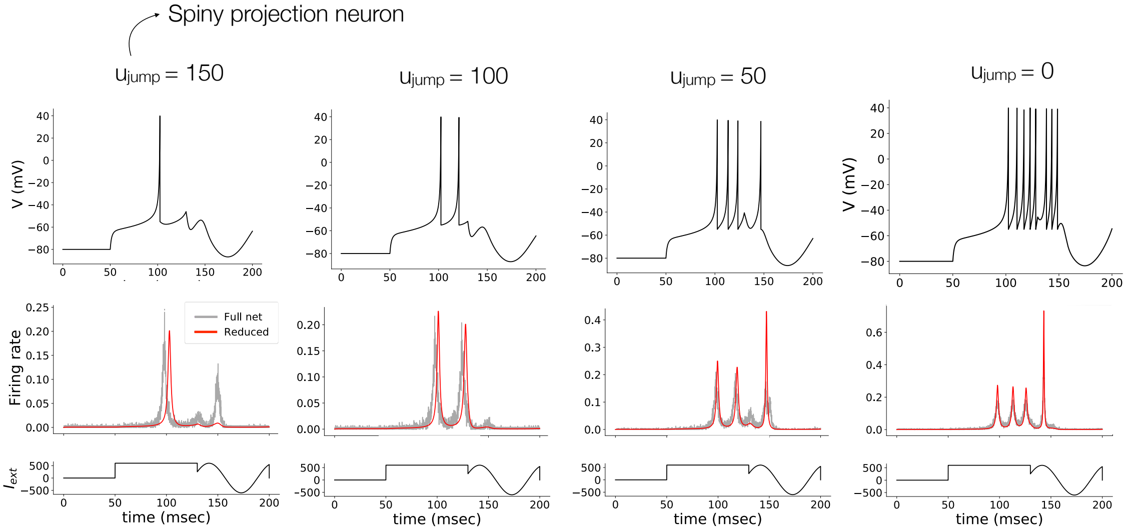

Figure 3.2: Comparison between full and reduced system for a population of spiny projection neurons. Spiny projection neurons of the neostriatum and basal ganglia can be described by the two-dimensional QIF neuron model with $a = 1\ nS/mV$, $b = 105\ nS$, $c = 2000\ nSmV$, $C_m = 50\ pF$, $V_r = -80\ mV$, $\alpha = 0.01\ msec^{-1}$, $\beta = -20\ nS$, $V_{peak} = 40\ mV$, $V_{reset} = -55\ mV$ and $u_{jump} = 150\ pA$ (Izhikevich, 2007d). Decreasing the value of u_{jump} improves representation of the population activity.

In Figure 3.2 we compare the full and reduced system for a population of uncoupled spiny projection neurons ($u_{jump} = 150$ pA). We then systematically decrease the value of u_{jump} we see how that changes the accuracy between dynamics of the full and reduced system. All the neurons receive an external current as described in Figure 3.1 (D). We see that there is not a perfect agreement between the full and reduced system for a population of spiny projection neurons (left panel). Decreasing the value of u_{jump} notably improves the agreement between the full and reduced system significantly, confirming that the high u_{jump} is at the origin of the mismatch observed. For $u_{jump} = 150$, one way to improve the representation of the population activity would be to decrease Δ. By decreasing the variance Δ of the intrinsic variable η, we decrease the heterogeneity of the network. As a result, we can consider again that all the neurons in a population W are receiving the same variable u at any given time (simulations not shown).

The particular case of bursting neurons

A critical point of the derivation of our reduced mean-field model is the assumption that the firing rate of a population is defined as the flux at infinity. In other words, we consider $V_{peak} \to \infty$. Similarly, we assume that $V_{reset} \to -\infty$. While moving V_{peak} towards infinity does not change the intrinsic spiking properties of the neurons that constitute the population, moving V_{reset} in the direction of $-\infty$ changes the microscopic behavior of bursting neurons.

Figure 3.3 (B) depicts the phase portrait of an intrinsically bursting neuron. Starting at point A, we are on the V-nullcline, where by definition $\frac{dV}{dt} = 0$, and the dynamics is going to be governed by the u-component. Since we are on the left of the u-nullcline, the trajectory follows a downward flux. As u slowly decreases, we reach point B below the V-nullcline, and the fast dynamics in the V direction pushes the system towards V_{peak}, at which point the system is reset to V_{reset}. This last process repeats while u slowly increases until it reaches point C, where a voltage reset takes the system to a point above the V-nullcline. In this region, the flux is directed towards the left, which brings the system back to point A.

By decreasing the value of V_{reset}, we lose the bursting dynamics, and the neuron model now shows tonic spiking instead (see Figure 3.3 (C)). One way to preserve the bursting dynamics of the microscopic system would be to move the V and u-nullclines by the same amount as the V_{reset} (Figure 3.3 (D)). We do so by decreasing the values of V_r and V_t (remember that $b = -a(V_r + V_t)$ and $c = aV_rV_t$). From

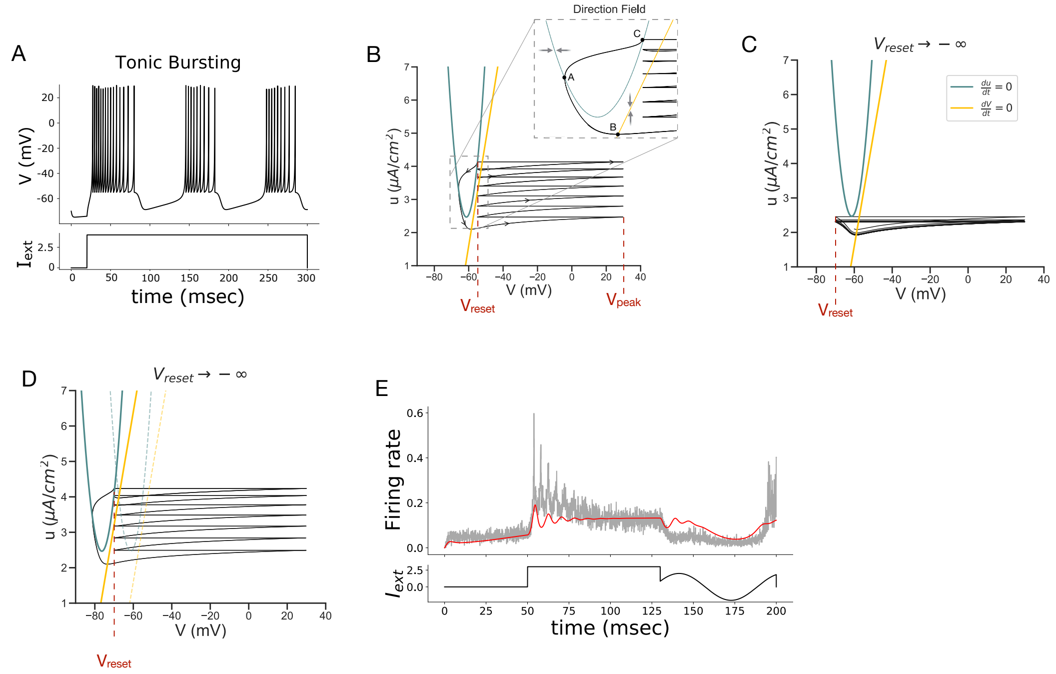

Figure 3.3: Comparison of reduced and full system for a class of bursting neurons. (A) Voltage trace of a bursting neuron using the Izhikevich QIF neurons model. Parameters: $a = 0.04$, $b = 5$, $c = 150$, $C_m = 1$, $V_r = -65$, $\alpha = 0.02$, $\beta = 0.32$, $u_{jump} = 0$. **(B)** Nullclines, $\frac{dV}{dt} = 0$ (green line) and $\frac{du}{dt} = 0$ (yellow line), for a system of a bursting neuron and respective trajectory (black line) on the phase plane. **(C)** Nullclines and trajectory of the system when V_{reset} decreases from -55 to -70 mV on the phase plane. The trajectory of the system no longer shows a bursting behavior. **(D)** Nullclines and trajectory of the system on the phase plane when $b = 6$, $c = 232$, $V_r = -80$ and $V_{reset} = -70$. As a result of the changes in b, c and V_r the nullclines moved to the left of the phase plane and we recover the trajectory of bursting neurons. **(E)** Comparison between full and reduced system for a population of bursing neurons (with $b = 6$, $c = 232$, $V_r = -80$ and $V_{reset} = -70$). The reduced system captures some but not all of the structure of the full bursting system.

Figure 3.3 (E), we see that by adopting this change the full and reduced system activity have approximately the same shape, but that they do not perfectly agree. It is important to note, however, that this method presents important faults: it implies that at $V_{reset} \to -\infty$, the resting and threshold potential, V_r and V_t, should also move to $-\infty$. This is not only a problem from the biological point of view, but it can also invalidate some mathematical results adopted during the derivation of the mean-field reduction; namely, when solving explicitly the integrals that define the firing rate and mean voltage of the population (equations (3.15) and (3.16)).

3.4 Discussion

In this chapter, we presented a reduction formalism that allows us to predict the collective dynamics of large networks of conductance-based interacting spiking neurons with different spiking properties. Starting with a population of two-dimensional QIF neurons, we considered an adiabatic approximation of a slow recovery variable, which enabled us to reduce the dimension of variables that describes the state of a neuron in the network. By doing so, we simplified the continuity equation describing the evolution of the state of our population, and we could directly apply the Lorentzian ansatz to solve the continuity equation and reduce our full network to a low-dimensional macroscopic system.

This mean-field formalism provides a paradigm to bridge the scale between population dynamics and the microscopic complexity of the physiology of the individual cells, opening the perspective of generating biologically realistic mean-field models from electrophysiological recordings for a variety of neural populations.

A similar idea appears in di Volo et al. (2019) and Nicola and Campbell (2013). Di Volo and colleagues propose a mean-field model of spiking neurons with recovery variable by calculating the transfer function in a semi-analytical way. This approach, however, is limited to cases where the neuron dynamics has a stationary firing rate, and it cannot be used to study populations of neurons whose transfer function cannot be well-defined di Volo et al. (2019). Similar to our approach, Nicola and Campbell use moment closure and a steady-state approximation of the recovery variable to write an expression for the population firing rate, defined as the integral of the population density function. However, they can't apply the Lorentzian ansatz to solve the integral because they don't consider the heterogeneity of the population. Therefore, for some types of networks won't be possible to be evaluated explicitly the firing rate integral (Nicola and Campbell, 2013).

Sufficient requirements for our approach to be valid are that the recovery variable u is the slowest in the system and that u_{jump} is relatively small. This means that even though it is possible to describe any class of spiking dynamics, the reduced model might be unable to describe the activity of specific neural populations, such as spiny projection neurons of the neostriatum and basal ganglia.

It is important to note that even though the original QIF neuron model for tonic bursting neurons fills all the requirements, the mean-field system seems to be inadequate to describe the population's behavior. Since, in the Izhikevich two-dimensional QIF model, the bursting mechanism depends on the position the system acquires in the phase-plane (V,u) upon reset, when moving V_{reset} to $infty$ will alter the behavior of the microscopic system. Therefore, despite having a good agreement between the full and reduced system, the population at study is no longer a population of tonic bursting neurons but of tonic spiking neurons. A solution found was to move the u and V-nullclines with V_{reset}, so that an action potential will reset the system to the same position in the phase-plane relative to the nullclines and preserve the bursting mechanisms of the original model. We do so by decrease the resting and threshold potential, V_r and V_t by the same amount as V_{reset}. The full and reduced system of the resultant tonic bursting neurons does not perfectly agree, but it accurately reproduces the oscillatory behavior of the population. In other words, when the system receives a big enough external input I_{ext}, both the full and reduced system show damped oscillations but with different frequencies. Therefore, the mean-field description may still be useful to study certain features of a population of bursting neurons and qualitative behavior. However, it is important to note that the approach taken for the case of the bursting neurons presents some fundamentals problems. Namely, it implies that both the reset, resting and threshold potential are set to $-\infty$. An alternative solution is to consider the two-dimensional theta neuron model with a slow recovery variable, which with the appropriate choice of parameters can produce bursting (Ermentrout and Kopell, 1986), and apply the steps as for the derivation of a two-dimensional QIF. In the theta neuron model, the system evolves along a circle and $V \in [-\infty, +\infty]$ maps to $\theta \in [0, 2\pi]$. A deeper analysis of this approach is necessary to prove its validity.

In the following chapter, we show how the exact mean-field model here derived can be applied to study the generation and expression of macroscopic oscillations in an entorhinal and hippocampal network.

A Validity of the Lorentzian ansatz

Previous work by Montbrió et al. (2015) shows how the dynamics of a class of QIF neurons generally converges to the Ott-Antonsen ansatz (OA) manifold. This is known has the Lorentzian ansatz (LA). In this section, we clarify why the Lorentzian ansatz holds for the ensembles of QIF neurons here considered.

We start by introducing the following transformation:

$$V_i^W = tan\frac{\theta_i^W}{2} \tag{25}$$

Then, Equation 3.1a transforms into:

$$C_m\frac{d\theta_i^W}{dt} = a(1-cos\theta_i^W)+(c-u^W+\eta_i+\sum_Z s_{WZ}E_r^Z+I_{ext})+(b-\sum_Z s_{WZ})sin\theta_i^W \tag{26}$$

Note that $V = \pm\infty$ corresponds to $\theta = \pm\pi$.

According to the Ott-Antonsen ansatz (Ott and Antonsen, 2008), in the thermodynamic limit, the dynamics of a class of systems

$$\frac{d\theta}{dt} = \Omega(\eta,t) + Im(H(\eta,t)e^{-i\theta}) \tag{27}$$

converges to the OA manifold

$$\tilde{\rho}(\theta|\eta,t) = \frac{1}{2\pi}Re[\frac{1+\alpha(\eta,t)e^{i\theta}}{1-\alpha(\eta,t)e^{i\theta}}] \tag{28}$$

where the function $\alpha(\eta,t)$ is related to $w(\eta,t) = x(\eta,t) + iy(\eta,t)$ as

$$\alpha(\eta,t) = \frac{1-w(\eta,t)}{1+w(\eta,t)} \tag{29}$$

Noticing that in the new variable θ^W our system belongs to the class 27 with $\Omega(\eta,t) = a + c + \sum_Z s_{WZ}E_r^Z + I_{ext} + \eta - u^W$ and $H(\eta,t) = (-b + \sum_Z s_{WZ}) + i(a -$

$c - \sum_Z s_{WZ} E_r^Z - I_{ext} - \eta + u^W)$, we infer that it converges to:

$$\tilde{\rho}(\theta|\eta, t) = \frac{1}{\pi} Re[\frac{1 + xtan^2(\frac{\theta}{2}) + ytan(\frac{\theta}{2}) + i(ytan^2(\frac{\theta}{2}) + (1-x)tan(\frac{\theta}{2}))}{tan^2(\frac{\theta}{2}) + x - ytan(\frac{\theta}{2}) + i(y - (1-x)tan(\frac{\theta}{2}))}] \tag{30}$$

Therefore, in the original variable V^X, our system converges to:

$$\rho(V^W|\eta, t) = \frac{1}{\pi} Re[\frac{1 + x(V^W)^2 + yV^W + i(y(V^W)^2 + (1-x)V^W)}{(V^W)^2 + x - yV^W + i(y - (1-x)V^W)}] \tag{31}$$

After some algebraic manipulations, we recover the LA (3.9)

$$\rho(V^W|\eta, t) = \frac{1}{\pi} \frac{x(\eta, t)}{(V^W - y(\eta, t))^2 + x(\eta, t)^2} \tag{32}$$

The LA ansatz solves the continuity equation exactly, making the system amenable to theoretical analysis. In section 3.3.4, we show that these solutions agree with the numerical simulations of the original QIF neurons, further validating the application of the LA.

4 | The Entorhinal Cortex as a theta rhythm generator

4.1 Introduction

Local field potentials in the entorhinal cortex (EC) show theta oscillations under different conditions. A regular prominent theta rhythm is observed in the EC during voluntary movements and REM sleep (Alonso and García-Austt, 1987), as well as under anesthesia (Mitchell and Ranck Jr., 1980). Early work suggested that the medial septum may be enforcing the theta rhythm into which the EC network is entrained (Gogolák et al., 1968; Stewart and Fox, 1990). This view is challenged by experimental work showing that lesions in the medial septum reduce but do not terminate theta rhythms in the hippocampal formation (Colgin, 2013; Winson, 1978) and that rhythmic activity seems to be originating in the medial entorhinal cortex (Mitchell and Ranck Jr., 1980; Gu and Yakel, 2017). The EC is believed to provide the major excitatory rhythmic drive to hippocampal theta oscillations (Buzsáki, 2002; Kamondi et al., 1998; Brankack et al., 1993). Therefore, a thorough knowledge of the intrinsic circuit properties of the EC is essential to understanding the origins of hippocampal theta and how the entorhinal structure modulates the rhythm's power and frequency.

The EC is organized into layers that can be characterized by different input-output connectivity and constituent neuron types. The deep layers (V/VI) are made of a heterogeneous population of excitatory pyramidal cells selectively targetted by outputs from the hippocampal CA1 region and project locally to the deep and superficial (II/III) layers of the EC. The superficial layers comprise fast-spiking PV+

interneurons, excitatory pyramidal cells, and stellate cells, with the stellate cells making up the largest group of principal cells (Witter et al., 2017). So far, there is no anatomical evidence that they form synaptic connections between themselves. *In vitro* studies revealed that stellate cells form strong reciprocal connections with PV+ interneurons and sparse connections with pyramidal cells of the superficial layers (Couey et al., 2013; Pastoll et al., 2012). Despite conflicting reports concerning stellate cells' projections to deep layers, it is well-established that they constitute the primary excitatory input of the hippocampus (Surmeli et al., 2015; Ohara et al., 2018; Tamamaki and Nojyo, 1993; Klink and Alonso, 1998; Buckmaster et al., 2004b; Canto et al., 2008).

Principal stellate cells have long been considered a key contributor to the entorhinal theta rhythm. They are endowed with slow hyperpolarizing currents that give them the ability to generate persistent rhythmic subthreshold oscillatory activity with a theta frequency when depolarized (Alonso and Klink, 1993; Rowland et al., 2018).

This chapter proposes a circuit model of the EC to study its intrinsic properties that allow external excitatory inputs to drive the system into an oscillatory regime. Firstly, we use Izhikevich's QIF neuron model with an adaptation variable to describe the entorhinal pyramidal cells, stellate cells, and fast-spiking interneurons and apply the exact reduction formalism presented in chapter 3 to obtain a macroscopic description of the entorhinal network. Then, to study how synchronized theta oscillations can arise in such a network, we infer the space of connectivity parameters that generate coherent theta rhythm. Our results suggest that the EC may utilize distinct subnetworks to generate low-frequency theta oscillations (type 2) and high-frequency theta oscillations (type 1).

4.2 Methods

4.2.1 Network of QIF neurons

In this study, we use a minimal spiking neural network model to represent the entorhinal cortex region. We consider a population of regular spiking pyramidal cells (E) - as found in the deep layers of the EC -, and a population of stellate cells (S) and fast-spiking interneurons (I) - as observed in the superficial layers. Note that although you can also find pyramidal cells in the superficial layers of the EC, we do not consider this population in our model since, contrarily to stellate cells, it is not clear if they play a role in the generation of the theta rhythm. In addition, they only form sparse connections with stellate cells (Witter et al., 2017; Couey et al., 2013; Pastoll et al., 2012). For similar reasons, we do not take into account the activity of other types of interneurons found in the superficial layers of the EC, such as CCK-expressing interneurons, since they are less abundant than PV+ cells and do not form connections with stellate cells (Witter et al., 2017).

Each cell i of each population W is described by the modified version of the Izhikevich QIF neuron model:

$$C_m \frac{dV_i^W}{dt} = aV_i^W + b(V_i^W)^2 + c - u^W + \eta_i + I_{ext} + I_{syn,i} \tag{4.1}$$

$$\frac{du^W}{dt} = \alpha(\beta(\langle V \rangle^W - V_r) - u^W) + u_{jump} \sum_{k=1}^{N_W} \sum_f \delta(t - t_f^k) \tag{4.2}$$

where V_i is the membrane potential of neuron i, and u the slow recovery variable of population W. The parameters C_m, a, b, c, V_r α, β and u_{jump} determine the dynamics of the neuron (see Chapter 3, section 3.2 for a more detailed explanation). The function δ is the Dirac mass measure and t_f^k is the firing time of neuron k. The parameter η_i represents a background current randomly drawn from a Lorentzian distribution that accounts for the network's heterogeneity, I_{ext} is an external current acting on all the neurons of the population, and $I_{syn,i}$ is the total synaptic current acting on neuron i.

The parameters C_m, a, b, c, V_r α, β and u_{jump} are chosen such as to reproduce the electrophysiological profile of the three neuron types: stellate cells with intrinsic subtreshold oscillations (S), class 1 pyramidal cells (E), and fast-spiking PV+ interneurons (I). All the parameters used are described in Table 4.1.

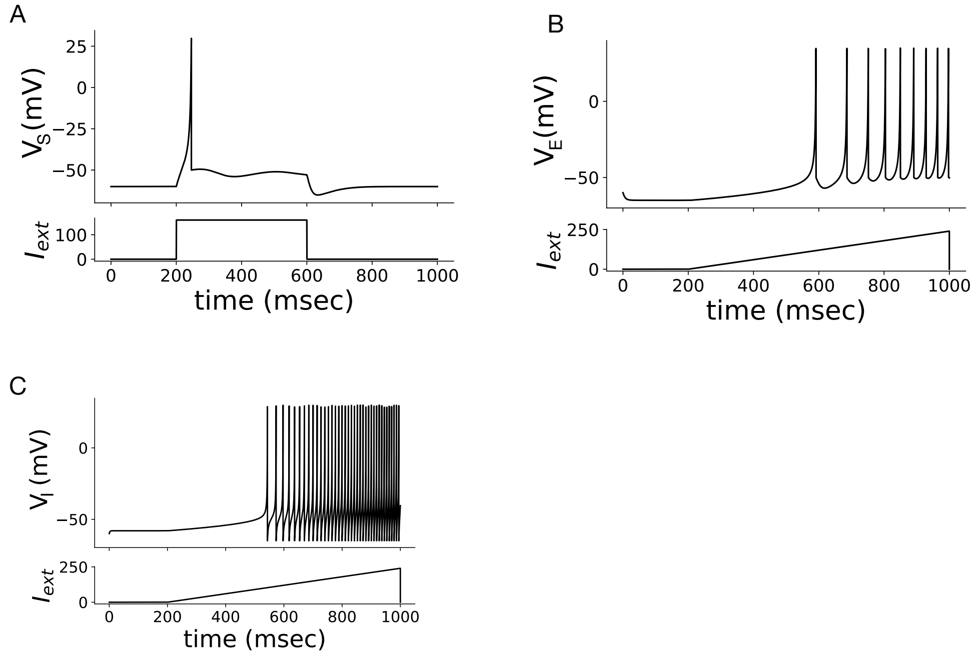

Figure 4.1: Dynamics of neurons in the enthorinal cortex. **(A)** Membrane potential of stellate cells using the Izhikevich's QIF with recovery variable model. Parameters taken from Izhikevich (2007e). **(B)** Membrane potential of regular spiking pyramidal cells using the Izhikevich's QIF with recovery variable model. Parameters taken from Izhikevich (2007c) **(C)** Membrane potential of fast-spiking interneurons using the Izhikevich QIF with recovery variable model. Parameters taken from Izhikevich (2007a). All parameters are described in Table 4.1

.

To our knowledge, there are no anatomical studies that determine precisely what is the relative size of each population of neurons in the EC. Therefore, we consider the three populations (S, I and E) to have the same size, similar to what is done in Neru and Assisi (2021). We assume that each population is made of 3000 neurons. We find that this is enough to get a reasonable estimate of the population's firing rates.

	S-cells	**I-cells**	**E-cells**
a (nS/mV)	0.75	1	0.7
b (nS)	78.75	98	73.5
c (nS/mV)	2025	2320	1820
C_m (pF)	200	40	100
V_r (mV)	-60	-58	-65
α $(msec^{-1})$	0.01	0.11	0.02
β (nS)	15	1.2	-2
u_{jump} (pA)	0	0	100
V_{peak} (mV)	30	30	30
V_{reset} (mV)	-50	-65	-60

Table 4.1: Parameter values of two-dimensional QIF neuron model for entorhinal stellate cells (S), fast-spiking interneurons (I), and pyramidal cells (E). Parameters adapted from Izhikevich (2007e), Izhikevich (2007a) and Izhikevich (2007c), respectively.

4.2.2 Synaptic model

In vitro studies show that pyramidal cells in the deep layers of the EC receive external excitatory inputs from the hippocampal CA1 region and project to interneurons and stellate cells in the superficial layers (Witter et al., 2017; Alonso and Klink, 1993; Hamam et al., 2000). Some studies also suggest the existence of reciprocal connections from stellate cells to pyramidal cells in the deep layers (Surmeli et al., 2015). Fast-spiking interneurons, in turn, form strong bi-directional connections with stellate cells (Witter et al., 2017; Alonso and Klink, 1993; Hamam et al., 2000). That being said, we consider the S-E-I network connected as schematically shown in Figure 5.1, where all populations are recurrently connected through gap junctions except for S-cells that do not form monosynaptic connections between themselves (Witter et al., 2017; Winterer et al., 2017) [1].

---

[1] Adding S-S connections in our model did not significantly alter the posterior of the remaining connectivity parameters (Figure S2)

The synaptic currents were modeled as follows:

$$I_{syn,i} = \sum_{Y} s_{WZ}(E_r^Z - V_i^W) \tag{4.3}$$

where E_r^Z is the reversal potential of the synapse, and s_{WZ} the synaptic conductance. The reversal potential depends on the nature of the synapse. If the synapse originates on an inhibitory cell population Z, $E_r^Z = -80$ mV; if it originates on an excitatory population $E_r^Z = 0$ mV. The synaptic conductance s_{WZ} is given by:

$$\frac{ds_{WZ}}{dt} = -\frac{s_{WZ}}{\tau_s} + \frac{p_{WZ}}{N_Z}\sum_{k=1}^{N_Z}\sum_{f}\delta(t - t_f^k) \tag{4.4}$$

where the parameter τ_s represents the synaptic time constant, N_Z is the number of neurons of population Z, and p_{WZ} is the coupling strength of population Z onto population W.

4.2.3 Mean-field description of the EC

We take advantage of the exact mean-field reduction system derived in chapter 3 to obtain a macroscopic description of the EC neural network. For simplicity, we consider instantaneous synapses ($s_{WZ} = p_{WZ}r_Z$) [2]. We then have that the following reduced system describes our network

For the S-cells:

$$C_m\frac{dr_S}{dt} = (b - p_{SI}r_I - p_{SE}r_E)r_S + 2ar_Sv_S + \frac{\Delta a}{\pi C_m} \tag{4.5a}$$

$$\begin{aligned} C_m\frac{dv_S}{dt} &= -\frac{(\pi r_S Cm)^2}{a} + av_S^2 + (b - p_{SI}r_I - p_{SE}r_E)v_S + c \\ &\quad - 80p_{SI}r_I - u^S + I_{ext} + \overline{\eta} \end{aligned} \tag{4.5b}$$

$$\frac{du^S}{dt} = \alpha(\beta(v_S - V_r) - u^S) + u_{jump}r_S \tag{4.5c}$$

For the I-cells:

---

[2] We later investigate how adding synapses with a slow dynamics affects our results (section 4.3.3).

$$
\begin{aligned}
C_m\frac{dr_I}{dt} &= (b - p_{II}r_I - p_{IS}r_S - p_{IE}r_E)r_I + 2ar_Iv_I + \frac{\Delta a}{\pi C_m} && \text{(4.6a)}\\
C_m\frac{dv_I}{dt} &= -\frac{(\pi r_I Cm)^2}{a} + av_I^2 + (b - p_{II}r_I - p_{IS}r_S - p_{IE}r_E)v_I + c && \text{(4.6b)}\\
&\quad - 80p_{II}r_I - u^I + I_{ext} + \overline{\eta}\\
\frac{du^I}{dt} &= \alpha(\beta(v_I - V_r) - u^I) + u_{jump}r_I && \text{(4.6c)}
\end{aligned}
$$

For the E-cells:

$$
\begin{aligned}
C_m\frac{dr_E}{dt} &= (b - p_{EE}r_E - p_{ES}r_S - p_{EI}r_I)r_E + 2ar_Ev_E + \frac{\Delta a}{\pi C_m} && \text{(4.7a)}\\
C_m\frac{dv_E}{dt} &= -\frac{(\pi r_E Cm)^2}{a} + av_E^2 + (b - p_{EE}r_E - p_{ES}r_S - p_{EI}r_I)v_E + c && \text{(4.7b)}\\
&\quad - 80p_{EI}r_I - u^E + I_{ext} + \overline{\eta}\\
\frac{du^E}{dt} &= \alpha(\beta(v_E - V_r) - u^E) + u_{jump}r_E && \text{(4.7c)}
\end{aligned}
$$

Figure 5.1 illustrates a comparison of the dynamics of the full network with the low-dimensional reduced system. It shows the time evolution of the external stimulus acting on all three populations (Figure 5.1 (a)), the spiking activity obtained from simulations of the full network, and the firing rates of the three populations given by the reduced description ((4.5a), (5.6a) and (5.7a) for the S, I and E-cells, respectively) and calculated from the full network simulations ($r_W = \frac{1}{N_W}\sum_{k=1}^{N_W}\sum_f \delta(t - t_f^k)$).

The reduced description captures the shape of the firing activity of the full network. This confirms that we can safely employ the reduced mean-field model to interpret the phenomena observed on the spiking network and to obtain theoretical predictions for its dynamics.

4.2.4 Bayesian inference algorithm for model parameter identification

In Bayesian inference, one can infer the parameters of interest θ from observed data x_0 given a model of their statistical relationship. In other words, given an estimation of the parameter distribution, which we call prior, and a likelihood (or sampling function) $p(x_0|\theta)$ we can compute the a posterior distribution $p(\theta|x_0) = p(x_0|\theta)p(\theta)$

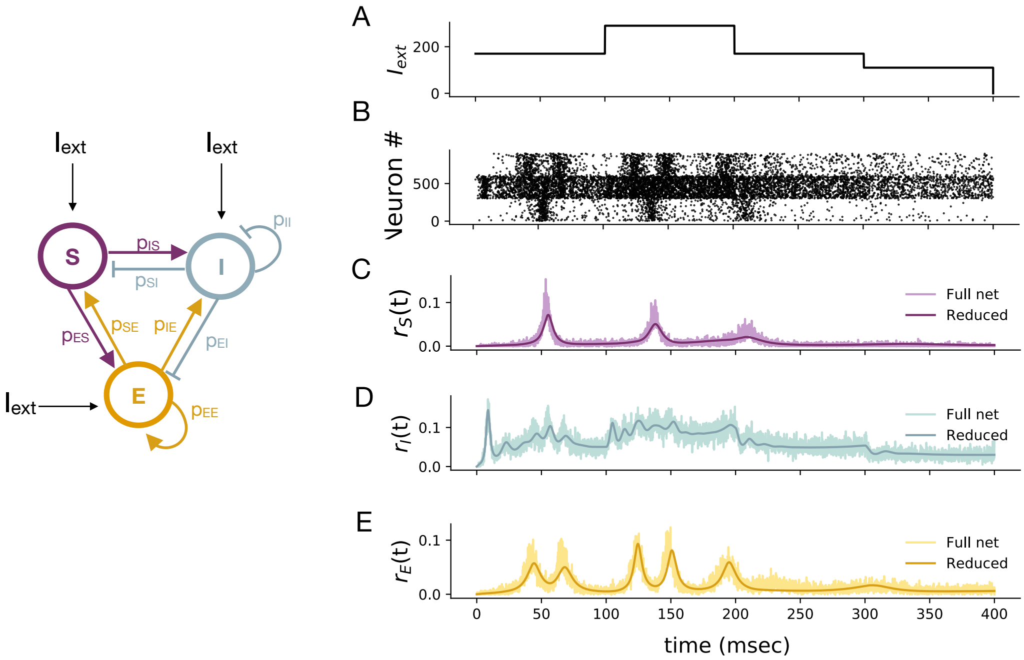

Figure 4.2: Comparison between the full network dynamics and the reduced system. Left panel: Schematic illustration of the neural network. The parameter p_{ij} denotes the connectivity strength of the population j onto the population i. The external current a acting on the different populations is denoted by I_{ext}. Right panel: **(A)** Time evolution of the stimulus I_{ext}. **(B)** Spiking activity obtained from simulations of the full network. The first 300 neurons are stellate cells (S); the following 300 are inhibitory (I); the last 300 are excitatory (E). **(C)** Firing rate of the SC obtained from simulations of the full and reduced system. **(D)** Firing rate of the I-cells obtained from simulations of the full and reduced system. **(E)** Firing rate of the E-cells obtained from simulations of the full and reduced system. Parameters: $N = 3000$; $\Delta = 15$; $\overline{\eta} = 25$; $p_{SI} = p_{IS} = 50$; $p_{SE} = p_{ES} = 90$; $p_{IE} = p_{EI} = 40$; $p_{II} = 55$; $p_{EE} = 40$.

which is high for parameters θ consistent with the data x_0, and it approaches zero as discrepancies increase. However, the likelihood function of most mechanistic models is untractable. In that case, one can use likelihood-free inference methods, such as Sequential Neural Posterior Estimation (SNPE), that compute posterior beliefs over parameters using simulations from the model rather than likelihood evaluations (Leuckmann et al., 2017).

We use a simulation-based inference algorithm that implements SNPE (Gonçalves et al., 2020) to infer the connectivity parameters of the S-E-I network that enable the generation of theta rhythm.

SNPE is a machine learning tool that identifies all the parameters of a mechanistic model that reproduce the target data (or selected data features). Given the data (or selected data features) x_0, a mechanistic model with parameters θ, and a prior distributions of the parameters $p(\theta)$, it returns a posterior distribution $p(\theta|x_0)$. Contrarily to other likelihood-free methods, SNPE uses all simulations to train an artificial network to identify all admissible parameters instead of filtering out simulations, i.e., it finds not only the best but all parameters consistent with the data.

The SNPE algorithm runs N simulations for a range of parameter values and trains an artificial neural network to map any simulation result onto a range of possible parameters. Parameter samples θ_n are drawn from the prior $p(\theta)$. A simulated response of the mechanistic model is obtained for each parameter sample, and a summary statistic x_n is computed. This results in N pairs of parameters and summary statistics (θ_n, x_n). At the end, the network is trained to find a mapping from summary statistics to parameter distributions by minimizing a loss function:

$$\mathcal{L} = -log(q_\phi(\theta_n|x_n)) \tag{4.8}$$

where $q_\phi(\theta_n|x_n)$ is the weighted posterior distribution (the network weights ϕ are adjusted based on the simulations results and inference settings). In other words, the network is trained to find a mapping from summary statistics to parameter distributions. Suppose a single round of inference is not sufficient for results to converge. In that case, SNPE can be run in multiple rounds, in which samples are drawn from the distribution $q_\phi(\theta_n|x_n)$ obtained at the end of the previous round instead of from the prior distribution $p(\theta)$. After the last round, $q_\phi(\theta_n|x_n)$ is returned as the inferred posterior distribution on parameters θ (Gonçalves et al., 2020).

We use a SNPE framework to identify the connectivity parameters of the network (p_{IS}, p_{SI}, p_{EI}, p_{IE}, p_{SE}, p_{ES}, p_{EE},p_{II}) for which each population of the S-E-I network is synchronized at theta frequency. We simulated the network's firing rates when an excitatory external current I_{ext} acts on the E-cells. This follows anatomical studies of the EC showing that excitatory hippocampal inputs target pyramidal cells in the deep layers of the EC (Witter et al., 2017). We define the frequency and amplitude of the firing rates of the three populations as the model output used for inference. More specifically, we consider firing rates with a frequency between 4 and 12 Hz and constant amplitude throughout 3000 msec as the desired simulated feature. We find that a simulation period of 3000 msec is long enough to accurately calculate the frequency of oscillations of the firing rates and detect a potential decrease in amplitude while not being too computationally expensive.

We based our algorithm on the Python code available at `https://www.mackelab.org/sbi/`. Inference is calculated after one round of 500 simulations. We chose uniform distributions for all priors. These simulation specifications proved to be enough for the system to converge to a solution.

4.3 Results

4.3.1 Estimating the EC network connectivity

Despite the progress made in the last years in mapping the entorhinal connectivity, it is still not clear what synaptic connections in the EC are enabling this structure to generate sustained theta oscillations. We use a Bayesian inference machine learning tool, SNPE, to derive the posterior distribution of the connectivity parameters (p_{SI}, p_{IS}, p_{ES}, p_{SE}, p_{IE}, p_{EI}, p_{II}, p_{EE}) for which the EC network model produces sustained rhythmic activity with theta frequency. We look at the network's response when an excitatory external current I_{ext} acts on the E-population. More precisely, we use a frequency of the firing rates r_S, r_E and r_I between 4 and 12 Hz as the target feature that the model needs to reproduce. This follows anatomical studies showing that hippocampal CA1 pyramidal cells target pyramidal cells on the deep layers of the EC (Witter et al., 2017), and experimental results showing that the EC is not an independent generator and it needs excitatory hippocampal inputs to generate theta oscillations (Gu and Yakel, 2017). For simplicity, we consider symmetric connections between the populations, i.e. $p_{WZ} = p_{ZW}$. For a first approach, we consider that this simplification can still give us an estimated idea of how the activity of each populations constraints the generation of oscillations. Moreover, by considering symmetric connections we reduce the number of parameters to explore which increases the efficiency and speed of the inference algorithm. Regarding the prior distribution of the connectivity parameters, we consider the uniforms distributions $p_{SI}, p_{IS} \in \mathcal{U}(0{,}100)$, $p_{SE}, p_{ES} \in \mathcal{U}(0{,}190)$, $p_{IE}, p_{EI} \in \mathcal{U}(0{,}100)$, $p_{II} \in \mathcal{U}(0{,}100)$,

$p_{EE} \in \mathcal{U}(0{,}100)$. Despite the lack of data to support our choice of priors, we find that the system converged to a solution in the chosen prior interval.

Initially, we infer both the connectivity parameters p_{WZ} and the external current I_{ext} to get an estimation of the magnitude that I_{ext} needs to have for the network to oscillate. From the resulting posteriors, we estimate that with an external current I_{ext}=100 pA, there is a connectivity configuration for which the system will generate theta (see Figure S1). We then adopt this value for the current and re-optimize the posteriors of the connectivity parameters. By doing so, we get a more accurate estimation of the parameters p_{WZ}, since the system needs to learn how to represent theta oscillations by sampling from a smaller number of parameters.

The posteriors distributions of the connectivity parameters are shown in Figure 4.3 (A). We select connectivity parameter values given by the mean of the posteriors, indicated by the violet lines/points in Figure 4.3 (A) (p_{IS},p_{SI}=43.9714, p_{SE}, p_{ES}=160.2503, p_{IE}, p_{EI}=34.4222, p_{II}=55.4267, p_{EE}=84.4322). By doing so, we obtain a set of parameters sampled from the high probability region. As we can see in Figure 4.3 (B) and (C), these parameters lead to simulations with the selected features. In other words, the populations firing rates obtained show sustained oscillations with a frequency in the theta range (6.3 Hz).

We next study the behavior of the network when its parameters are in the high probability posterior region. For that, we adopt the mean values of the parameters posterior distribution defined before and examine the system's dynamics when the external current changes. Namely, we plot the bifurcation diagram of the populations firing rates, r_E, r_S and r_I, with the external current I_{ext} as a bifurcation parameter (Figure 4.3 (D)). The three populations' firing rates exhibit two Hopf bifurcation points, at I_{ext} = 55.42 pA and I_{ext} = 129.7. This indicates the system is in an oscillatory regime for 55.42 < I_{ext} < 129.7. Notably, for I_{ext} > 69 pA the frequency of the oscillations are in the theta range (Figure 4.3 (E))

We notice that the connectivity of the S-E subnetwork ,p_{SE}, p_{ES} and p_{EE}, is more constrained (with a standard deviation of 15 and 12, respectively) and has a higher mean value (160.2503 and 84.4322, respectively) than the other parameters p_{SI}, p_{IS}, p_{IE}, p_{EI} and p_{II} (with mean values 43.9714, 34.4222 and 55.4267 and standard deviations 22, 18 and 24, respectively). In other words, the high posterior probability region is highly constrained by high values of S-E and E-E connections.

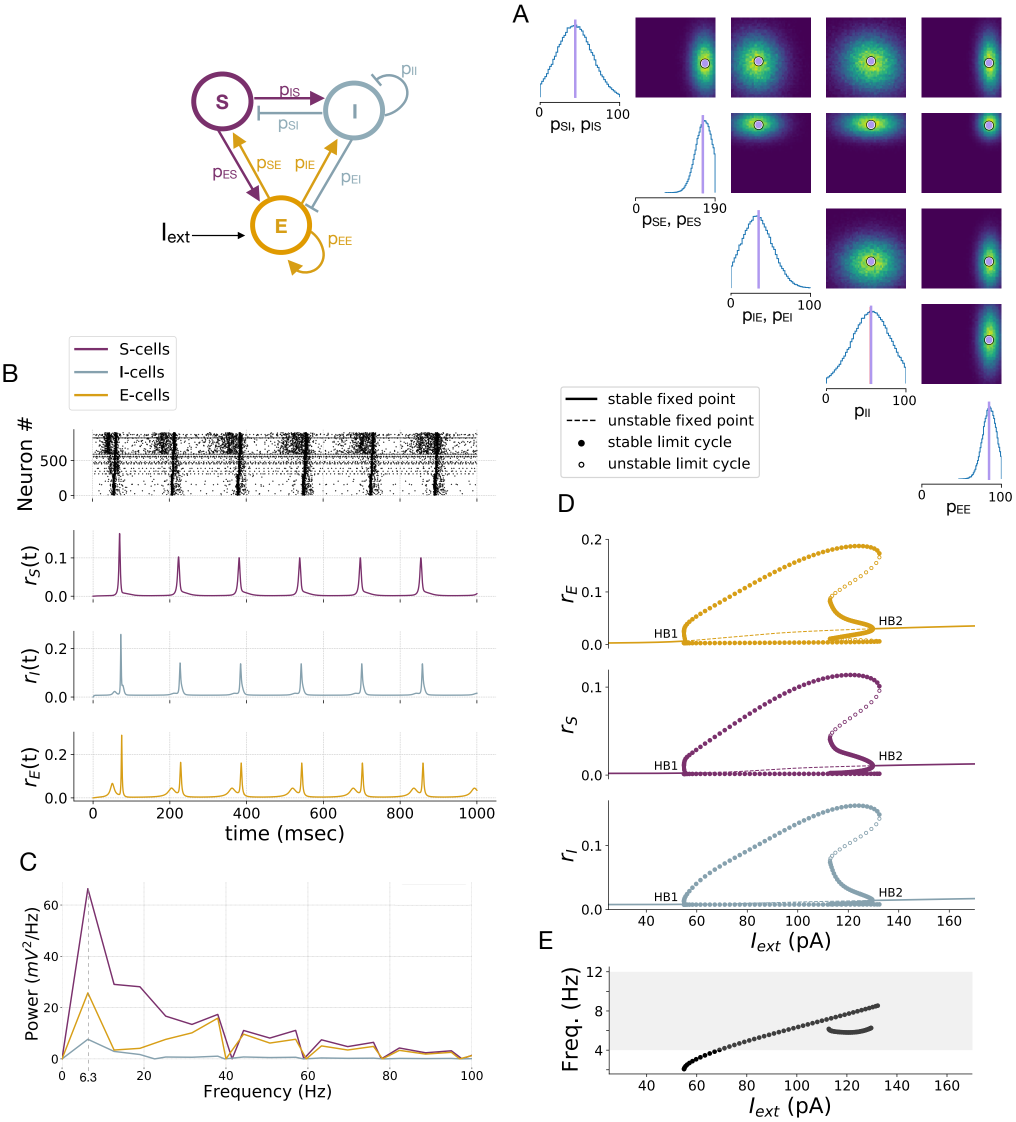

Figure 4.3: Estimating network connectivity for theta generation in a mean-field model of the EC network using statistical inference. Top left panel: Schematic illustration of neural network with stellate cells (S), fast-spiking interneurons (I), and pyramidal cells (E). **(A)** Posterior distribution over 5 connectivity parameters, with I_{ext}=100 pA. Mean of parameters posterior distribution represent high probability parameters (in purple): p_{IS},p_{SI}=43.9714; p_{SE}, p_{ES}=160.2503; p_{IE}, p_{EI}=34.4222; p_{II}=55.4267; p_{EE}=84.4322. **(B)** Network activity generated by posterior samples from a high probability region (in purple, in (A)). Top panel: Spiking activity obtained from simulations of the full network. We look at the activity of 300 random neurons of each population. The first 300 neurons are stellate cells (S); the following 300 are inhibitory (I); the last 300 are pyramidal cells (E). Bottom panel: Firing rates of S, I and E-cells population obtained from simulations of the reduced mean-field system. (*caption continues on next page*)

(C) Power spectrum of the activity of the S, I and E population's firing rate calculated over 10 seconds. The power spectrum of all populations shows a maximum at 6.3 Hz. **(D)** Bifurcation diagrams of the firing rates of the 3 neural populations. System is in an oscillatory regime for HB1 $< I_{ext} <$ HB2, with HB1=55.42 pA and HB2=129.7 pA. HB: Hopf bifurcation. **(E)** Frequency of oscillations of the network in the stable limit cycle regime (HB1 $< I_{ext} <$ HB2). For $I_{ext} > 69 Hz$, the system oscillates with a frequency between 4 and 8.5 Hz, which is in the theta range (grey area).

These observations may indicate that the network is utilizing more the S-E sub-network to generate theta rhythm than the full S-E-I network. To explore this hypothesis, we start by examining changes in the firing rates of the S and E-cells populations when we change the strength of connection of these two populations with the I-cells, p_{IE}, p_{EI} and p_{SI}, p_{IS}.

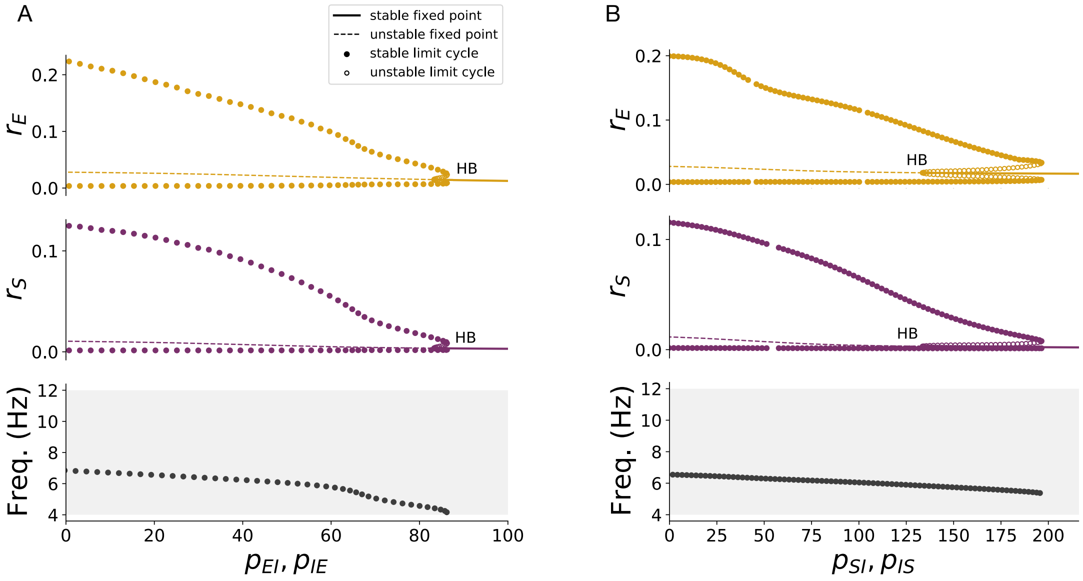

Figure 4.4: System dynamics for changing S-I and E-I connectivities. **(A)** Bifurcation diagram of S and E firing rates with the connectivity between the E and I population, p_{IE}, p_{EI}, as a bifurcation parameter. The system is in an oscillatory regime for $p_{IE}, p_{EI} = 83.26$. Bottom panel: Frequency of the network's stable limit cycle ($83.26 < p_{IE}, p_{EI}$) as a function of the I-E connectivity. Stable limit cycle is always in the theta range frequency of oscillations (grey area). **(B)** Bifurcation diagram of S and E firing rates with the connectivity between the S and I population, p_{SI}, p_{IS}, as a bifurcation parameter. The system is in an oscillatory regime for $p_{SI}, p_{IS} = 133.6$. Bottom panel: Frequency of the network's stable limit cycle ($133.6 < p_{SI}, p_{IS}$) as a function of the I-S connectivity. Stable limit cycle is always in the theta range frequency of oscillations (grey area). Remaining parameters from high probability region (from Figure 4.3 (A), in purple). HB: Hopf bifurcation.

When plotting a bifurcation diagram using p_{IE}, p_{EI} and p_{SI}, p_{IS} as the bifurcation parameters, we see that oscillations with a theta frequency persist when these parameters are zero and cease to exist when we increase them beyond an Hopf bifurcation parameter at $p_{IE}, p_{EI} = 83.26$ and $p_{IE}, p_{EI} = 133.6$ (see Figure 4.4). It is important to note, however, that the E-I connection, although not necessary to generate oscillations, can modulate its frequency. Increasing p_{IE}, p_{EI} decreases the frequency of oscillations (Figure 4.4 (C)). The S-I connection, on the other hand, does not modulate significantly the frequency of the network (Figure 4.4 (D)). These results indicate that removing the S-I or E-I connections from the circuit does not impair its ability to generate theta rhythm.

4.3.2 S-E circuit as a theta rhythm generator

To further explore the role of the I-cell and the S-E subnetwork in the generation of theta oscillations, we test the ability of the S-E circuit to act as a theta rhythm generator.

Removing the I population while keeping the same values for the p_{SE}, p_{ES} and p_{EE} connectivity parameters ($p_{SE}, p_{ES} = 160.2503$ and $p_{EE} = 84.4322$) did not prevent the generation of theta in the S-E circuit (Figure 4.5). Furthermore, it did not significantly change the bifurcation diagrams of the S and E populations firing rates. For $44.77 < I_{ext} < 110.3$ pA, the system is in an oscillatory regime with approximately the same amplitude as the one generated by the S-E-I network (Figure 4.5 (C)). Similarly, the stable limit cycles generated in the S-E network are primarily in the theta range (Figure 4.5 (D)). This is in agreement with previous studies showing that model stellate cells synchronize with fast excitatory synapses (Acker et al., 2003).

Next, we focused on the potential functional role of the S-E network connectivity parameters in network dynamics. From Figure 4.6 we see that the recurrent connections in the E population are not necessary to obtain sustained oscillations in our population model. When $p_{EE} = 0$, the system is still in an oscillatory regime for $172 < p_{SE}, p_{ES} < 247$ However, increasing the value of p_{EE} value inside the region of oscillatory regime (grey area in Figure 4.6, left panel), the power of the firing rate of both S and E increases (see Figure 4.6, right panel). Hence, a recurrently connected E population, although not necessary, increases the power of the oscillations. Re-

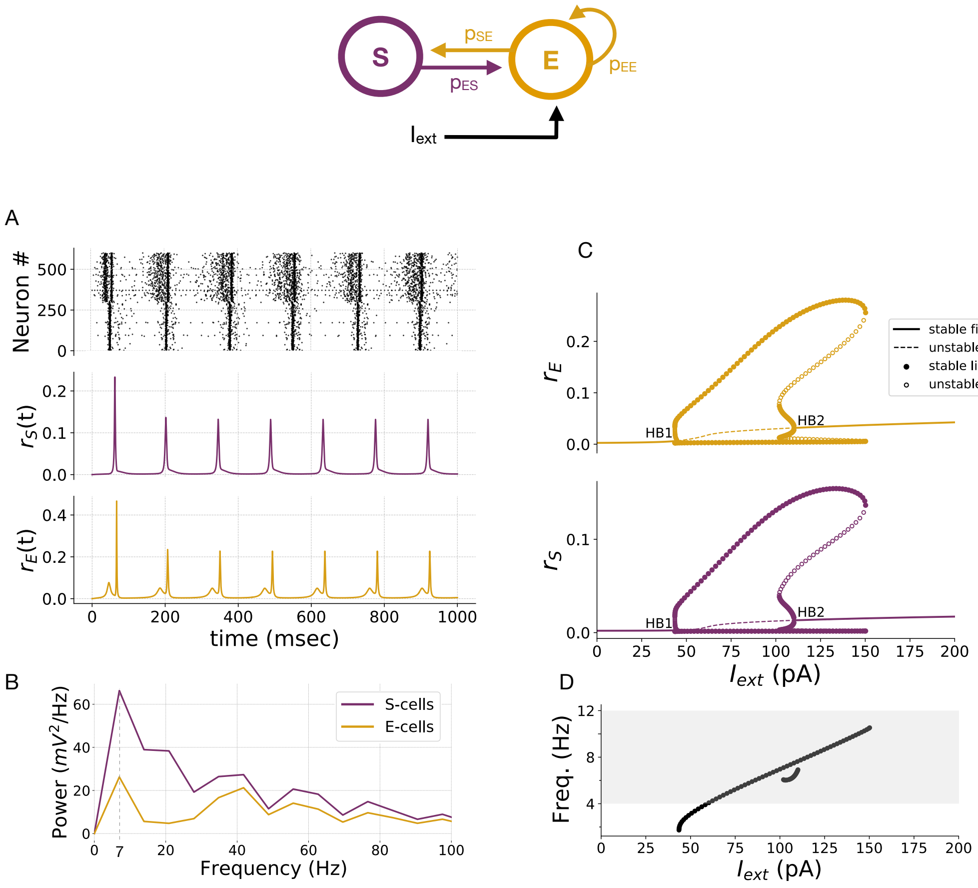

Figure 4.5: Dynamical analysis of the reduced S-E network. Top panel: Schematic illustration of the S-E sub-network. **(A)** Network activity generated by posterior samples from a high probability region of Figure 4.3 (A) (in purple): $p_{SE}, p_{ES} = 160.2503$ and $p_{EE} = 84.4322$), with $p_{SI}, p_{IS} = p_{EI}, p_{IE} = p_{II} = 0$ and $I_{ext} = 100$ pA. Top panel: Spiking activity obtained from simulations of the full network. We look at the activity of 300 random neurons of the S and E population. The first 300 neurons are stellate cells (S); the last 300 are pyramidal cells (E). Bottom panel: Firing rates of S and E-cells population obtained from simulations of the reduced mean-field system. **(B)** Power spectrum of the activity of the S and E populations firing rate calculated over 10 seconds. The power spectrum of both populations shows a maximum at 7 Hz. **(C)** Bifurcation diagrams of the firing rates of the S and E populations. System is in oscillatory regime for HB1 $< I_{ext} <$ HB2, with HB1=44.77 pA and HB2=110.3 pA (HB: Hopf bifurcation). **(D)** Frequency of oscillations of the network in the stable limit cycle regime (HB1 $< I_{ext} <$ HB2). For $I_{ext} > 58Hz$ the system oscillates with a frequency in the theta range (grey area).

garding the frequency of the oscillations, even though it seems that overall increasing p_{EE} or p_{SE}, p_{ES} increases the frequencies of oscillations, this effect is small.

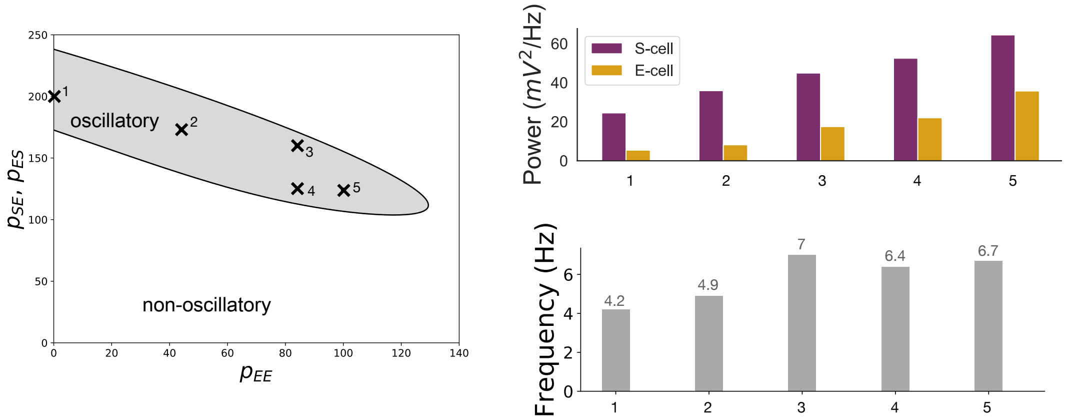

Figure 4.6: Exploring reduced EC network dependence on connectivity parameters. Stability region of the S-E subnetwork for I_{ext}=100 pA, constrained by the S-E and E-E connections (grey area). Power and frequency of oscillations produced change as we move inside the stability region. Coordinates: (1) $p_{EE} = 0$ and $p_{SE}, p_{ES} = 200$; (2) $p_{EE} = 44$ and $p_{SE}, p_{ES} = 173$; (3) $p_{EE} = 84$ and $p_{SE}, p_{ES} = 160$; (4) $p_{EE} = 84$ and $p_{SE}, p_{ES} = 125$; (5) $p_{EE} = 100$ and $p_{SE}, p_{ES} = 124$.

4.3.3 Entorhinal mechanisms of type 1 and type 2 theta generation

The theta rhythm can be classified into type 1 or type 2, according to its frequency and behavioral correlates. Type 1 theta has a frequency of 8-12 Hz and it is typically observed during exploratory behavior and REM sleep; type 2 has a lower frequency of 4-7 Hz and it appears during states of alert immobility and under anesthesia. Experimental studies suggest that the EC may be modulating the two types of theta differently; namely, while lesions to the EC can abolish type 1 theta, they disrupt behavioral and sensory correlates of both type 1 and type 2 (Montoya and Sainsbury, 1985; Buzsáki, 2002). We hypothesize that the EC is utilizing different subnetworks to generate type 1 and type 2 theta oscillations. We suggest that while the S-E network can efficiently generate type 1 oscillations, under certain conditions, we may need to utilize the full S-E-I network to generate type 2 theta oscillations, in particular when I_{ext} is very high. The main observations leading to this hypothesis were the fact that the frequency of oscillations increases rapidly with I_{ext} in the S-E circuit (Figure 4.5 (D)) while increasing slowly in the S-E-I network (Figure 4.3 (E)). Additionally, increasing the strength of the E-I connection decreases the network frequency of oscillations, as already mentioned (see Figure 4.4 (A)).

To further explore this hypothesis, we repeat the method used in section 4.3.1 to infer the posterior distribution of the S-E-I network connectivity that generates sustained oscillations with a frequency of 8-12 Hz or 4-7 Hz (type 1 and type 2 rhythm, respectively) when it receives an external input $I_{ext} = 100$ pA. We consider the prior distributions $p_{SI}, p_{IS} \in \mathcal{U}(0{,}100)$, $p_{SE}, p_{ES} \in \mathcal{U}(0{,}190)$, $p_{IE}, p_{EI} \in \mathcal{U}(0{,}100)$, $p_{II} \in \mathcal{U}(0{,}190)$, $p_{EE} \in \mathcal{U}(0{,}100)$. For these prior intervals, our model converges to a solution (Figure 4.7).

To generate low-frequency theta rhythm, the system is making use of the E-I connection more than to generate high-frequency theta, i.e. the mean value of the posterior distribution of p_{EI}, p_{IE} and p_{II} is higher than for the high-frequency case. The opposite is true for the recurrent connections p_{EE}. The posteriors of p_{SE}, p_{ES} and p_{SI}, p_{IS} are identical in for both type 1 and type 2 theta generation. This seems to indicate that I-cells became more relevant in the generation of low-frequency theta rhythm. Please note that the posterior parameter distributions represent the probability of parameters taken from the distribution reproducing the target feature, reproducing high-frequency and low-frequency theta. That being said, it does not mean that the S-E subnetwork cannot reproduce low-frequency theta oscillations. In fact, the S-E subnetwork considered in section 4.3.2 is reproducing theta oscillations in the low-frequency range (4-7 Hz).

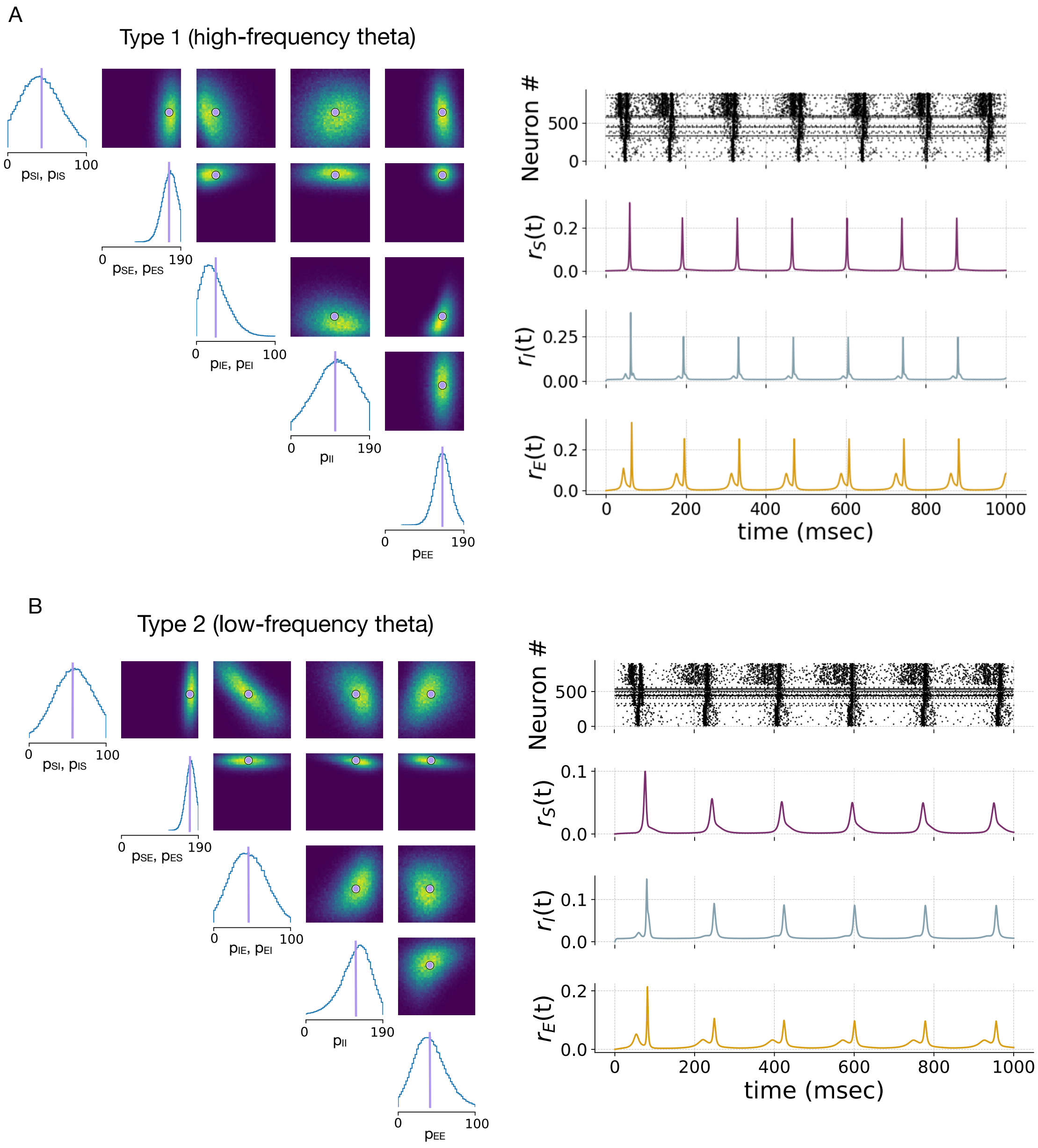

Figure 4.7: Estimating the connectivity of the EC network using statisticial inference for the generation of type 1 (8-12 Hz) and type 2 (4-7 Hz) theta oscillations with I_{ext}=100 pA. (A) Posterior distribution over the S-E-I network connectivity parameters for the generation of type 1 theta rhythm. High probability parameters (in purple): $p_{SI}, p_{IS} = 46.0033$, $p_{SE}, p_{ES} = 161.6447$, $p_{IE}, p_{EI} = 30.5906$, $p_{II} = 97.5407$, $p_{EE} = 139.4172$. **(B)** Posterior distribution over the S-E-I network connectivity parameters for the generation of type 2 theta rhythm. High probability parameters (in purple): $p_{SI}, p_{IS} = 46.8981$, $p_{SE}, p_{ES} = 156.8319$, $p_{IE}, p_{EI} = 40.3033$, $p_{II} = 55.3938$, $p_{EE} = 69.4229$.

For a S-E network receiving a current I_{ext}=150 pA, the SNPE algorithm could not find a connectivity configuration capable of generating type 2 oscillations, while for a S-E-I network, the system converged to a plausible solution (see Figure 4.8) if we incorporate a slow connection between the S and I-cell populations ($\frac{dg_{IS_{slow}}}{dt} = -\frac{g_{IS_{slow}}}{100} + p_{IS_{slow}} r_S$).

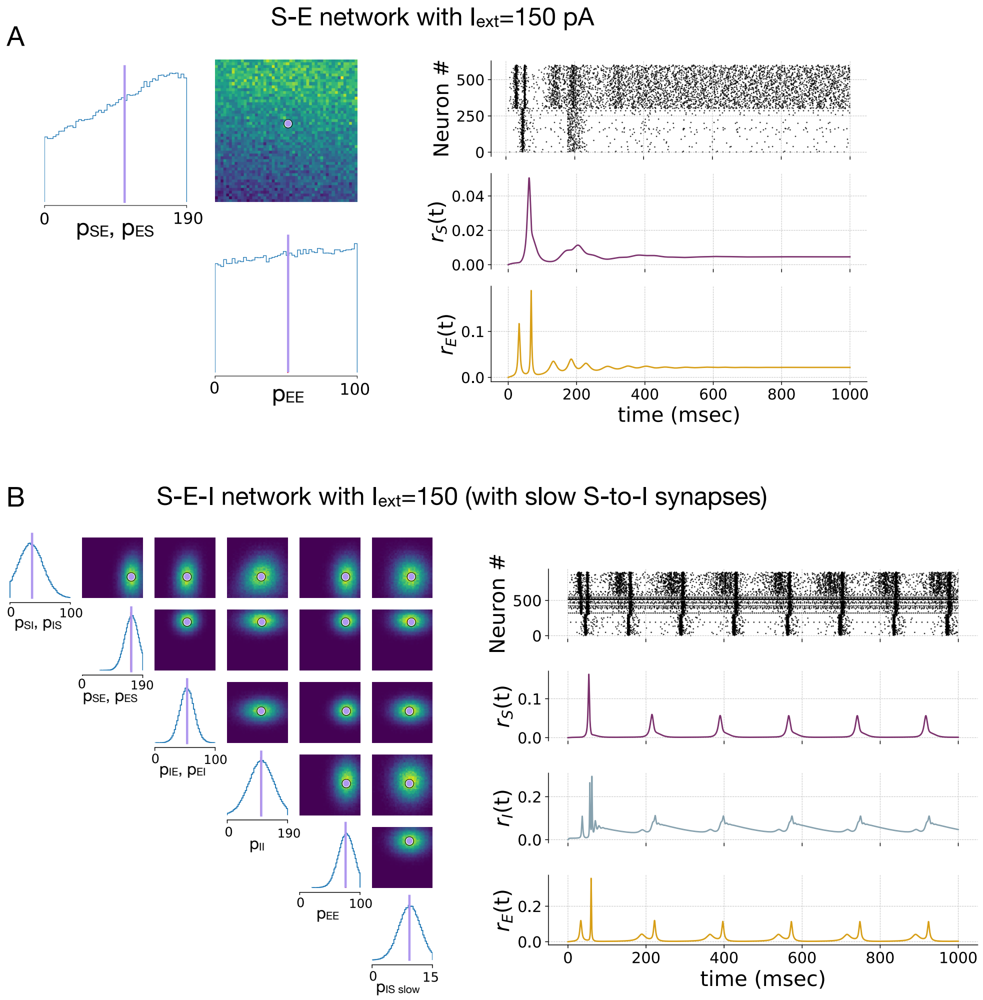

Figure 4.8: Inference of connectivity parameters that enable the generation of type 2 theta for different EC subnetwork configurations. (A) Left panel: Posterior distributions of connectivity parameters of S-E subnetwork. Even though the high probability region is not well defined, we consider the following parameter samples (in purple): p_{SE}, p_{ES} = 106.7219 and p_{EE} = 51.1498. Right panel: Spiking activity from simulations of the full network (first 300 neurons are pyramidal cells, and last 300 neurons are stellate cells), and firing rates of the S and E populations from simulations of the reduced mean-field model, with parameters from the high probability region. (*caption continues on next page*)

(B) Left panel: Posterior distributions of connectivity parameters of S-E-I subnetwork with slow S-to-I synapses ($\tau_s = 100$ msec). We consider parameter samples from the high probability region (in purple): $p_{SI}, p_{IS} = 36.3320$; $p_{SE}, p_{ES} = 152.7230$; $p_{IE}, p_{EI} = 53.3772$; $p_{II} = 105.9564$; $p_{EE} = 76.2192$; $p_{IS_{slow}} = 9.2546$. Right panel: Spiking activity from simulations of the full network, and firing rates of the S,I and E populations from simulations of the reduced mean-field model, with parameters from the high probability region.

Bear in mind that so far, we had only considered instantaneous synapses. Adding a slow synapse only improved convergence to a solution in the S-E-I network. More specifically, adding slow synapses between S and E cells on the S-E network did not lead to the generation of the low-frequency theta.

In summary, if the external current I_{ext} is small enough (for example, 100 pA), both the S-E and S-E-I network are capable of generating low-frequency oscillations with similar power (Figure 4.9 (A) and (B)). However, as we increase I_{ext} to 150 pA, only the S-E-I can generate low-frequency theta oscillations.

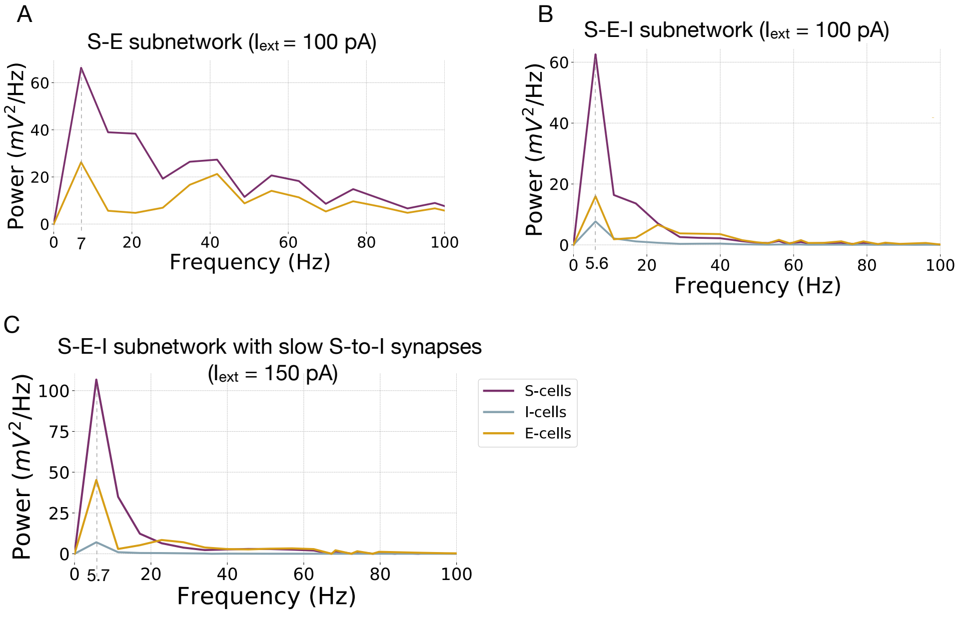

Figure 4.9: Power spectrum of type 2 theta oscillations produced with different subnetwork and configurations. **(A)** Power spectrum produced by the S-E subnetwork with I_{ext}=100 pA, instantaneous synapses, and connectivity parameters p_{SE}, p_{ES} and p_{EE} sampled from high probability region of Figure 4.3 (A). Figure reproduced from 4.3 (C). **(B)** Power spectrum produced by the S-E-I subnetwork with I_{ext}=100 pA, instantaneous synapses, and connectivity paremeters sampled from high probability region of Figure 4.7 (B). (*caption continues on next page*)

(C) Power spectrum produced by the S-E-I subnetwork with I_{ext}=150 pA, instantaneous synapses and a slow S-to-I synapse (τ_s = 100 msec), and connectivity paremeters sampled from high probability region of Figure 4.8 (B).

These results indicate that there are different entorhinal network configurations for which an external current (originating, for example, in the hippocampal CA1 region) gives rise to type 2 theta oscillations. For low values of external current, both an S-E and S-E-I network with instantaneous synapses can generate type 2 oscillations with identical power; for high values of external current, only an S-E-I network with a slow S-to-I synapse can reproduce type 2 theta. Also, a strong external input in a S-E-I network produces type 2 theta with the highest power (see Figure 4.9).

Next, we explore the different subnetworks capable of generating type 1 theta oscillations and under which conditions. We found that both an S-E and S-E-I subnetwork under different conditions (with or without slow synapses, and with low or high external currents) generates type 1 theta, with different frequencies and power. The connectivity parameters of a S-E network with I_{ext}=100 pA or 150 pA, as well as a network of S-E-I with I_{ext}=150 pA with or without slow S-to-I synapses, and with I_{ext}=100 pA all converge to a solution (see Figures 4.7 and 4.10). From Figure 4.11, we see that out of all the network configurations considered, a S-E-I network with I_{ext}=150 pA produces type 1 oscillations with the highest power. In comparison, the S-E subnetwork with I_{ext}=150 pA produces oscillations with the highest frequency. On the other hand, the S-E-I network with I_{ext}=100 pA produces type 1 oscillations with the lowest power and frequency.

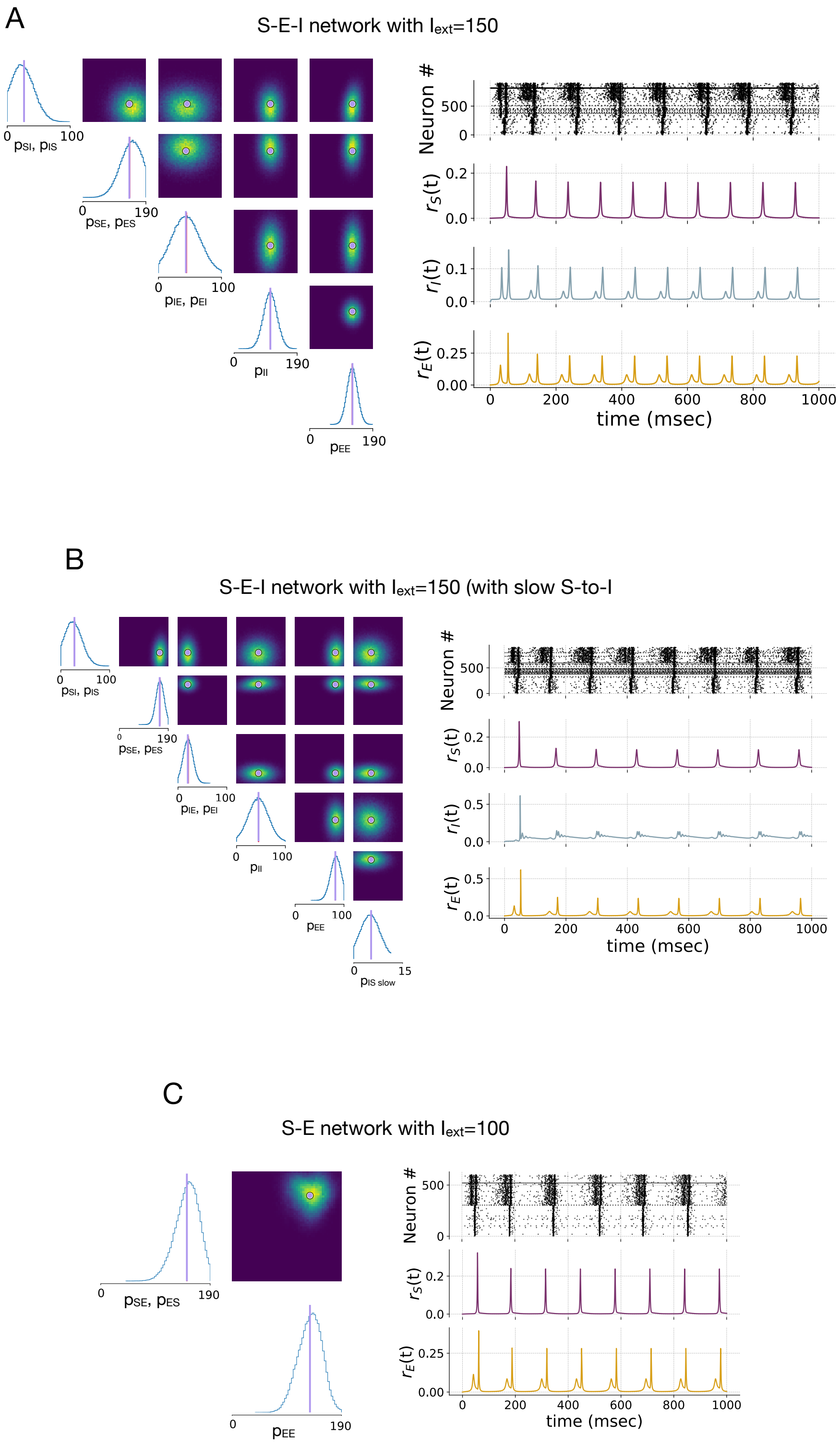
A
S-E-I network with Iext=150
0 100 pSI, pIS
0 190 pSE, pES
0 100 pIE, pEI
0 190 pII
0 190 pEE
Neuron #
500
0
rS(t)
0.2
0.0
rI(t)
0.1
0.0
rE(t)
0.25
0.00
0 200 400 600 800 1000
time (msec)
B
S-E-I network with Iext=150 (with slow S-to-I
0 100 pSI, pIS
0 190 pSE, pES
0 100 pIE, pEI
0 100 pII
0 100 pEE
0 15 pIS slow
Neuron #
500
0
rS(t)
0.2
0.0
rI(t)
0.5
0.0
rE(t)
0.5
0.0
0 200 400 600 800 1000
time (msec)
C
S-E network with Iext=100
0 190 pSE, pES
0 190 pEE
Neuron #
500
0
rS(t)
0.2
0.0
rE(t)
0.25
0.00
0 200 400 600 800 1000
time (msec)

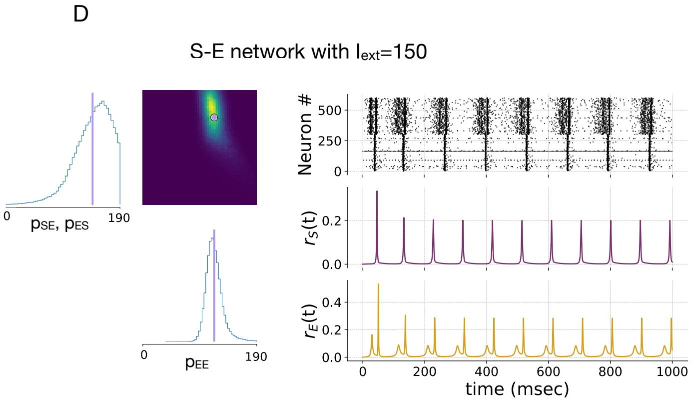

Figure 4.10: Inference of connectivity parameters that enable the generation of type 1 theta, for different configurations of the EC network. **(A)** Inference of the connectivity parameters of a S-E-I network with instantaneous synapses, subjected to an external current $I_{ext} = 150$ pA. We consider parameters sampled from the high probability region (in purple): p_{IS},p_{SI}=27.0279; p_{SE}, p_{ES}=141.1522; p_{IE}, p_{EI}=44.3601; p_{II}=109.0740; p_{EE}=128.0583 **(B)** Inference of the connectivity parameters of a S-E-I network with instantaneous synapses and a slow S-to-I synapse (τ_s = 100 msec), subjected to an external current $I_{ext} = 150$ pA. We consider parameters sampled from the high probability region (in purple): p_{IS},p_{SI}=27.8001; p_{SE}, p_{ES}=157.5060; p_{IE}, p_{EI}=21.0786; p_{II}=45.0699; p_{EE}=82.0658; $p_{IS_{slow}} = 5.3456$. **(C)** Inference of the connectivity parameters of a S-E network with instantaneous synapses, subjected to an external current $I_{ext} = 100$ pA. We consider parameters sampled from the high probability region (in purple): p_{SE}, p_{ES}=149.6219; p_{EE}=135.3354. **(D)** Inference of the connectivity parameters of a S-E network with instantaneous synapses, subjected to an external current $I_{ext} = 150$ pA. p_{SE}, p_{ES}=144.0672; p_{EE}=119.2519.

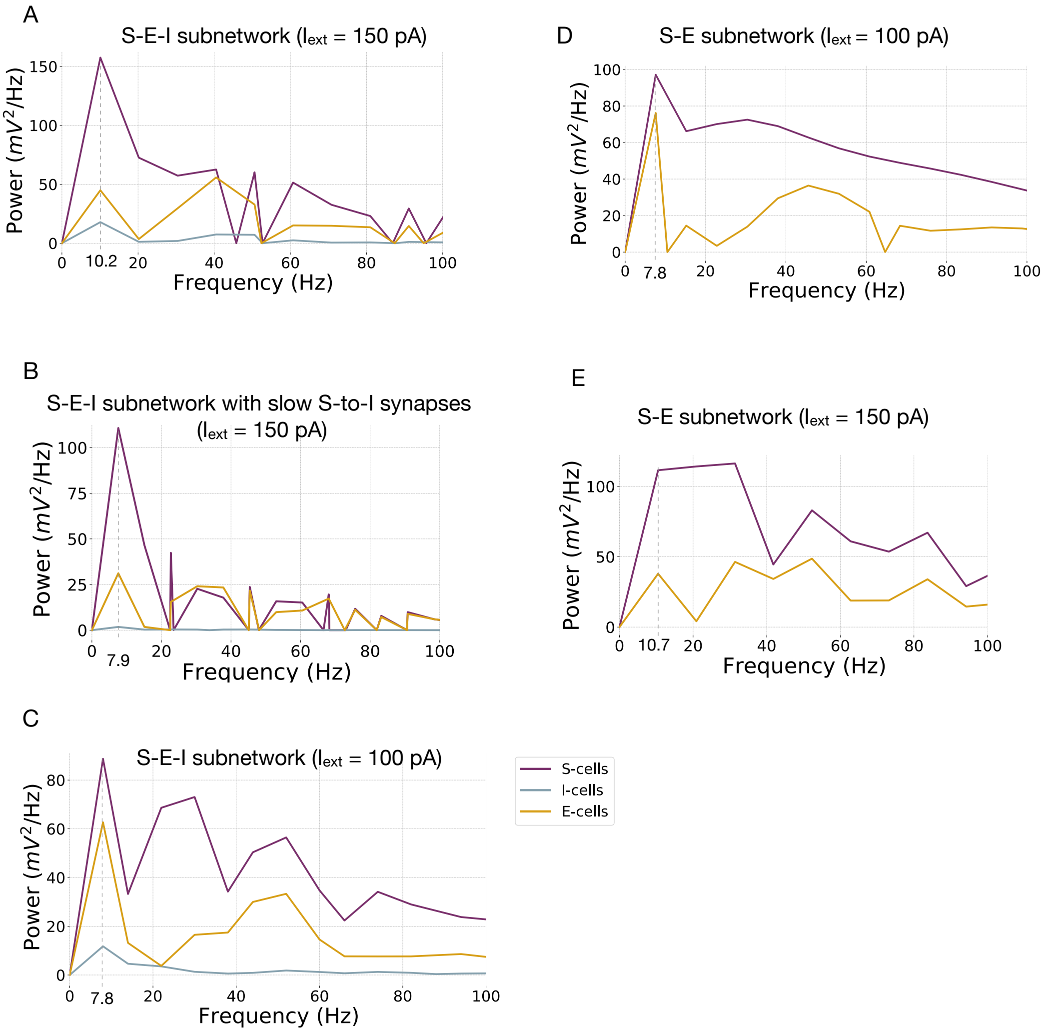

Figure 4.11: Power spectrum of type 1 theta oscillations produced with different subnetwork. For each subnetwork, we used the parameters sampled from the respective high probability posteriors. Power was calculated over 10 seconds. **(A)** Power spectrum produced by the S-E-I subnetwork with instantaneous synapses and I_{ext} = 150 pA. Connectivity parameters used sampled from Figure 4.10 (A). **(B)** Power spectrum produced by the S-E-I subnetwork with instantaneous synapses and a slow S-to-I synapse (τ_s = 100 msec) and I_{ext} = 150 pA. Connectivity parameters used sampled from Figure 4.10 (B). **(C)** Power spectrum produced by the S-E-I subnetwork with instantaneous synapses and I_{ext} = 100 pA. Connectivity parameters used sampled from Figure 4.7 (A). **(D)** Power spectrum produced by the S-E subnetwork with instantaneous synapses and I_{ext} = 100 pA. Connectivity parameters used sampled from Figure 4.10 (C). **(E)** Power spectrum produced by the S-E subnetwork with instantaneous synapses and I_{ext} = 150 pA. Connectivity parameters used sampled from Figure 4.10 (D).

4.4 Discussion

Despite being well established that the EC is a necessary structure for the generation of theta oscillations, its role in the induction and maintenance of theta is poorly understood. Previous work suggests that the EC is simply responding to external theta inputs from the medial septum since inactivation of the medial septum disrupts the receptive field of grid cells in the EC (Koenig et al., 2011). Recent studies challenge this view by suggesting that the EC circuit may be intrinsically generating theta rhythm as a response to excitatory hippocampal inputs (Gu and Yakel, 2017). However, it is still unclear what intrinsic neuronal properties and network mechanisms enable the entorhinal circuit to generate theta rhythm.

In this chapter, we used a computational model framework to investigate the intrinsic properties of the entorhinal circuitry that give rise to theta oscillations. We used a mean-field description of the entorhinal network, composed of pyramidal cells, stellate cells, and fast-spiking interneurons, to study the connectivity requirements for coherent theta oscillations to arise. Our results suggest that the EC may be utilizing distinct subnetworks under different conditions to generate type 1 and type 2 theta rhythm. If the entorhinal network receives a small excitatory current (for example, I_{ext}= 100 pA), both the S-E and S-E-I subnetwork can generate type 2 theta oscillations with identical power and frequency. However, if the EC receives a strong external excitatory input (for example, I_{ext} = 150 pA), the S-E subnetwork is not capable of generating type 2 oscillations; the system requires synaptic connections with I-cells. Interestingly, it requires the existence of a slow excitatory synapse between the S and I cells (with τ_s=100 msec).

Concerning the generation of type 1 oscillations (8-12 Hz), the EC circuit can generate oscillations more robustly; meaning, both an S-E and S-E-I network (with or without slow synapses) produce type 1 theta rhythm with similar powers (powers vary between 100 and 150 mV^2/Hz) for different values of I_{ext}. These observations suggest that blocking the PV+ activity should impact type 1 and type 2 theta oscillations differently.

In all the subnetworks and theta subtypes considered, an excitatory drive acting on the E-cell population is necessary for the system to enter into an oscillatory regime. This agrees with experimental results showing that the EC is not an independent rhythm generator and needs hippocampal excitatory inputs to generate theta. Interestingly, our modeling work suggests that fast synapses between S and E cells are crucial to achieving synchrony, given that the high probability posterior of p_{SE}, p_{ES} has a high value and was highly constrained for the generation of both type 1 and type 2 theta oscillations, where synchrony is defined as sustained oscillations of the populations firing rates. Synaptic connections between the I-cells and the other populations (S and E) are likely to also be playing a role in synchronizing the activity of the full network, given that abolishing the I-cell population from our network can change the power of the oscillations. In some cases, it can even eradicate theta oscillations. For example, an EC network without I-cells cannot generate type 2 oscillations when the excitatory input acting on the network is high. Also, suppressing the I population considerably decreases the power of type 1 theta. However, due to the different effects eliminating the I-cell population can have on the generation of the different types of theta, it isn't easy to access what role the I-cells are playing in the synchronization of the network. Moreover, both the p_{SI}, p_{IS} and p_{EI}, p_{IE} parameters have strained posterior distributions. Therefore, it is not possible to conclude from our results how I-connections modulate synchrony in the network.

Several studies indicate that NMDAR activation is crucial for the generation of hippocampal theta oscillations (Buzsáki, 2002; Leung and Desborough, 1988; Leung and Shen, 2004; Korotkova et al., 2010). Some even suggest that the EC uses NMDAR-dependent mechanisms to generate theta rhythm (Gu et al., 2017). According to our modeling work, adding a slow excitatory synapse between the S and I cell population is, in some cases, crucial for the generation of theta oscillations, in particular for the generation of type 2 theta. Our results are consistent with experiments showing that theta oscillations are impaired in mice with selective NMDAR knockout in PV interneurons during anesthesia (Korotkova et al., 2010). Adding a slow synapse between the other populations (S and E) did not change our results. However, a more accurate description of the NMDAR dynamics is necessary to judge the role of NMDAR on the S-E and E-E synapses. Namely, include a voltage-dependent term in the description of the NMDA-mediated synapse (in our study, we generally consider a synapse with a decay time of 100 msec). Furthermore, NMDARs are known to present a high calcium permeability (Burnashev et al., 1995).

Therefore, NMDAR can potentially regulate the neurons' excitability and enhance neurotransmitter release by triggering calcium-induced cascades. Taking that into account, it might be valuable to consider these effects of the NMDAR activation to address their role in the modulation of the EC circuit and the generation of theta.

A Supplementary Figures

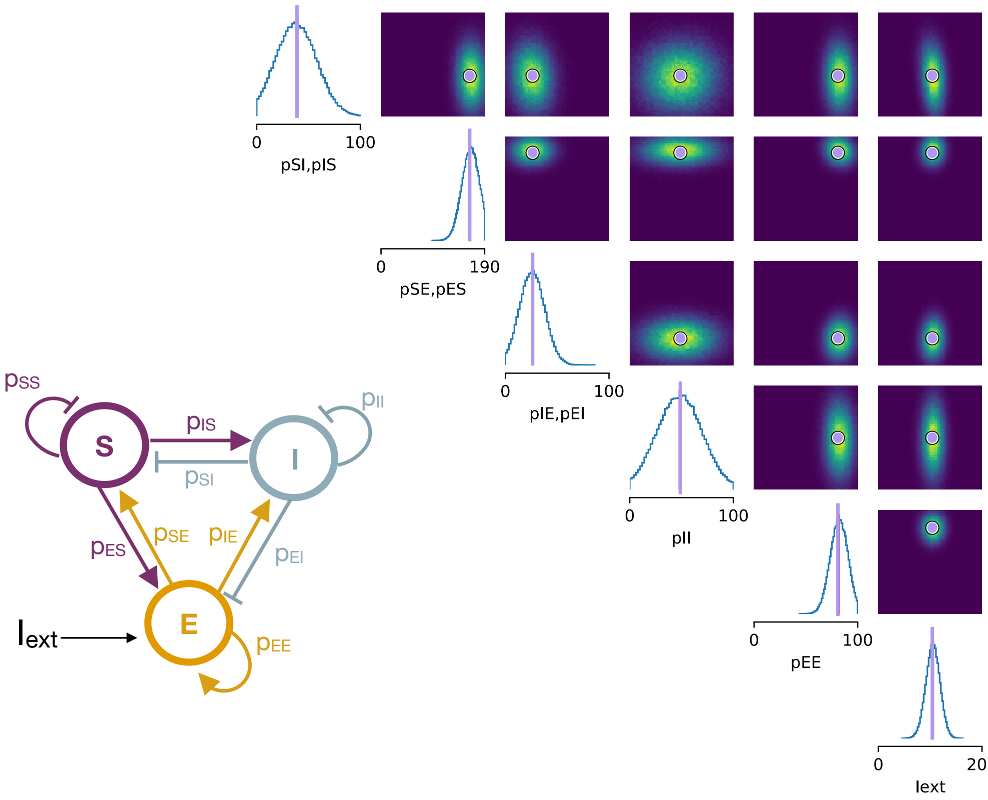

Figure S1: Estimating network connectivity and external current magnitude in mean-field model of EC network using statistical inference. Left panel: Schematic illustration of neural network. Right panel: Posterior distribution over 6 parameters. Mean of parameters posterior distribution: p_{IS},p_{SI}=39.1196; p_{SE}, p_{ES}=162.6039; p_{IE}, p_{EI}=26.2234; p_{II}=48.2827; p_{EE}=81.7969; I_{ext}=105.2518.

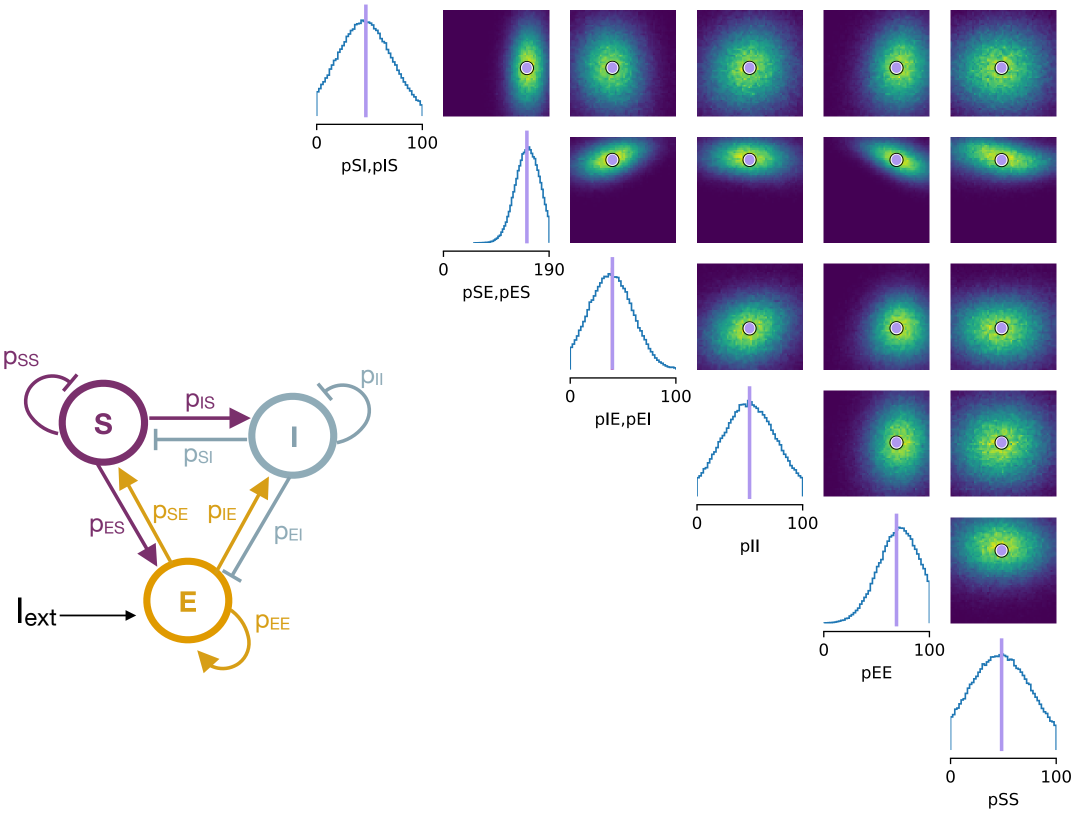

Figure S2: Estimating network connectivity in mean-field model of EC network using statistical inference (with recurrent S-S connections). Left panel: Schematic illustration of neural network. Right panel: Posterior distribution over 6 parameters, with I_{ext}=100. Mean of parameters posterior distribution: p_{IS},p_{SI}=46.3876; p_{SE}, p_{ES}=149.9954; p_{IE}, p_{EI}=39.5836; p_{II}=49.6283; p_{EE}=68.8112; p_{SS}=48.1571. Adding recurrent S-S connections (p_{SS}) did not significantly change the posterior distribution of the remaining connectivity parameters (see Figure 4.3 (A) for comparison)

5 The hippocampus as a theta rhythm resonator

5.1 Introduction

Hippocampal theta oscillations are a prominent 4-12 Hz rhythm observed in the hippocampus and associated structures. It has been linked to spatial and episodic memories, and its malfunction is strongly correlated with cognitive dysfunction such as memory deficits (Colgin, 2013, 2016; Hinman et al., 2018).

Studies indicate that the hippocampus contains the necessary circuitry to generate and maintain theta oscillations without any extrinsic inputs. Goutagny and colleagues measured a spontaneous theta rhythm in the CA1 region of an intact *in vitro* hippocampus preparation (Goutagny et al., 2009). Moreover, several modeling studies confirm that a CA1 microcircuit can produce oscillations with a theta frequency (Ferguson et al., 2017; Chatzikalymniou and Skinner, 2018; Kopell et al., 2010; Giovannini et al., 2017; Chatzikalymniou et al., 2020). While some assume that OLM cells play a crucial role in the generation of theta rhythm (Kopell et al., 2010; White et al., 2000), others suggest that a microcircuit of CA1 fast-spiking and pyramidal cells is capable of robustly generating oscillations with a theta rhythm (Giovannini et al., 2017; Ferguson et al., 2017; Chatzikalymniou et al., 2020).

Besides the hippocampus, two other brain regions are known to be essential for the generation and maintenance of hippocampal theta rhythm *in vivo*: the medial septum (MS) and the entorhinal cortex (EC). Still, the origins of *in vivo* theta remain elusive, partly due to the difficulty in recording the activity from all the three essential regions (hippocampus, MS, and EC) simultaneously. To address this question, Gu and Yakel established an *in vitro* tri-culture preparation of the septal-entorhinal-hippocampal circuit (Gu and Yakel, 2017). Their study indicates that theta originates in the EC and then propagates to the hippocampus, namely to the CA1 region, through the temporoammonic pathway. The generation of theta in the septo-entorhinal-hippocampal circuit was firstly dependent on the co-activation of septal cholinergic inputs acting on OLM cells and SC inputs. However, after performing co-paired activation several times, hippocampal PYR-OLM and SC-PYR synapses were potentiated, and theta could be induced by SC stimulation alone. In light of these results, in this chapter, we use a network model to examine CA1 hippocampal responses to theta oscillatory inputs from the EC when cholinergic co-paired activation is being performed and when only the SC is stimulated.

We use the mean-field framework presented in chapter 3 to build a network model of OLM cells, fast-spiking neurons, and pyramidal cells. We then access the role of each neural population and the connections they form in the modulation of the network's behavior. More specifically, we examine the connectivity configurations for which the network resonates to external rhythmic inputs with theta frequency under different conditions - when the network receives SC glutamatergic inputs paired or not with cholinergic inputs. We start by introducing the CA1 network model, composed of OLM cells (O), fast-spiking interneurons (I), and pyramidal cells (E). We then use a statistical inference algorithm (Gonçalves et al., 2020) to derive the distribution of the network's connectivity parameters that permit the O-I-E system (submitted to glutamatergic inputs paired with or without cholinergic inputs) to resonate to theta inputs. Finally, we study how potentiation of the hippocampal PYR-OLM and SC-PYR synapses that results from cholinergic pairing changes the hippocampal mechanisms of theta induction and expression.

5.2 Methods

5.2.1 CA1 network of QIF neurons

We use a minimal spiking neural network model to represent the hippocampal CA1 region. We consider a population of OLM cells (O), fast-spiking interneurons (I), and pyramidal cells (E).

Each cell i of each population W is described by a modified version of the Izhikevich QIF neuron model:

$$C_m \frac{dV_i^W}{dt} = aV_i^W + b(V_i^W)^2 + c - u^W + \eta_i + I_{ext} + I_{syn,i} \tag{5.1}$$

$$\frac{du^W}{dt} = \alpha(\beta(\langle V \rangle^W - V_r) - u^W) + u_{jump} \sum_{k=1}^{N_W} \sum_{f} \delta(t - t_f^k) \tag{5.2}$$

where V_i is the membrane potential of neuron i, and u the slow recovery variable acting on population W. The parameters C_m, a, b, c, V_r α, β and u_{jump} determine the dynamics of the neuron (see Chapter 3, section 3.2 for a more detailed explanation). The function δ is the Dirac mass measure and t_f^k is the firing time of neuron k. The parameter η_i represents a background current randomly drawn from a Lorentzian distribution that accounts for the network's heterogeneity, I_{ext} is an external current acting on all the neurons of the population, and $I_{syn,i}$ is the total synaptic current acting on neuron i.

The parameters C_m, a, b, c, V_r α, β and u_{jump} that describe each neuron type (OLM, fast-spiking and pyramidal cells) were adapted from previous models used to describe neurons with similar dynamics. Namely, the E-cells are described by the Izhikevich's model of non-bursting CA1 pyramidal neuron (Izhikevich, 2007b), and the I-cells by the Izhikevich's fast-spiking interneurons model (Izhikevich, 2007a). Given that the hippocampal OLM and EC stellate cells have a similar electrophysiological profile and synchronization properties (Kopell et al., 2010), we use the S-cell model described in the previous chapter to describe the dynamics of the O-cells (see chapter 4, section 4.2). You can find a summary of all the parameters in Table 5.1.

	O-cells	**I-cells**	**E-cells**
a (nS/mV)	0.75	1	0.5
b (nS)	78.75	98	52.5
c (nS/mV)	2025	2320	1350
C_m (pF)	200	40	50
V_r (mV)	-60	-58	-60
α $(msec^{-1})$	0.01	0.11	0.02
β (nS)	15	1.2	0.5
u_{jump} (pA)	0	0	50
V_{peak} (mV)	30	30	30
V_{reset} (mV)	-50	-65	-60

Table 5.1: Parameter values of the two-dimensional QIF neuron model for CA1 hippocampal OLM cells (O), fast-spiking interneurons (I), and pyramidal cells (E). Parameters adapted from Izhikevich (2007e), Izhikevich (2007a), and Izhikevich (2007b), respectively.

5.2.2 Synaptic model

We consider bidirectional synaptic connections among all populations of our network (O, I, and E), as schematically shown in Figure 5.1. We also consider self-connections among the neurons of each population, except for the O-cells, given that previous studies show that recurrent connections among OLM cells do not contribute to the production of theta (Kopell et al., 2010). The synaptic currents were modeled as follow:

$$I_{syn,i} = \sum_{Y} s_{WZ}(E_r^Z - V_i^W) \tag{5.3}$$

where E_r^Z is the reversal potential of the synapse, and s_{WZ} is the synaptic conductance. If the synaptic connections originate on a population of inhibitory cells, the reversal potential is -80 mV; if they originate in a population of excitatory cells, the reversal potential is 0 mV. Similar to what has been done in previous work, we do not consider slow NMDA and $GABA_B$ synapses (Kopell et al., 2010; Aussel, 2018). Moreover, experimental studies showing that NMDARs in the hippocampus are not necessary for the generation of theta rhythm in an EC-hippocampal circuit support the decision of not considering slow synapses (Gu et al., 2017). Instead, we consider instantaneous synapses, i.e. whenever a pre-synaptic neuron in Z spikes, the conductance s_{WZ} is instantaneously increased:

$$s_{WZ} = \frac{p_{WZ}}{N_Z} \sum_{k=1}^{N_Z} \sum_{f} \delta(t - t_f^k) \tag{5.4}$$

where N_Z is the number of neurons of population Z, and p_{WZ} is the coupling strength of population Z on population W.

5.2.3 Network input

When studying the hippocampal responses submitted to paired cholinergic and SC inputs, we do not explicitly model cholinergic activation of the O-cells in a timely manner and instead consider an external current $I_{ext} = 50$ pA acting on the O-cells. Similarly, SC inputs are modeled as an external current I_{ext}=50 pA acting on the I and E-cells. Even though cholinergic activation of O-cells typically results in excitatory currents of smaller amplitude than SC stimulation of I and E-cells, taking a smaller current I_{ext} acting on the O-cells did not significantly change our results (simulations not shown). As we have seen in chapter 2, cholinergic activation of OLM cells results in the inhibition of the I-cells. Therefore, during the simulation of the pairing protocol, we fixate the synaptic connection from the O to the I population to a high value ($p_{OI} = 70$).

When studying the hippocampal responses during SC stimulation alone, the O-cells are not activated by any external current, while E and I populations receive an external input $I_{ext} = 50$ pA.

5.2.4 Mean-field description of the CA1 network

Similar to what was done in the previous sections, we use the exact mean-field reduction model derived in Chapter 3 to obtain the macroscopic description of the CA1 neural network. The low dimensional system reads as follows:

For the O-cells:

$$C_m\frac{dr_O}{dt} = (b - p_{OI}r_I - p_{OE}r_E)r_O + 2ar_Ov_O + \frac{\Delta a}{\pi C_m} \tag{5.5a}$$

$$C_m\frac{dv_O}{dt} = -\frac{(\pi r_O Cm)^2}{a} + av_O^2 + (b - p_{OI}r_I - p_{OE}r_E)v_O + c \tag{5.5b}$$

$$- p_{OI}r_I 80 - u^O + I_{ext} + \overline{\eta} \tag{5.5c}$$

$$\frac{du^O}{dt} = \alpha(\beta(v_O - V_r) - u^O) + u_{jump}r_O \tag{5.5d}$$

For the I-cells:

$$C_m\frac{dr_I}{dt} = (b - p_{II}r_I - p_{IO}r_O - p_{IE}r_E)r_I + 2ar_Iv_I + \frac{\Delta a}{\pi C_m} \tag{5.6a}$$

$$C_m\frac{dv_I}{dt} = -\frac{(\pi r_I Cm)^2}{a} + av_I^2 + (b - p_{II}r_I - p_{IO}r_O - p_{IE}r_E)v_I + c \tag{5.6b}$$

$$- p_{II}r_I 80 - u^I + I_{ext} + \overline{\eta} \tag{5.6c}$$

$$\frac{du^I}{dt} = \alpha(\beta(v_I - V_r) - u^I) + u_{jump}r_I \tag{5.6d}$$

For the E-cells:

$$C_m\frac{dr_E}{dt} = (b - p_{EE}r_E - p_{EO}r_O - p_{EI}r_I)r_E + 2ar_Ev_E + \frac{\Delta a}{\pi C_m} \tag{5.7a}$$

$$C_m\frac{dv_E}{dt} = -\frac{(\pi r_E Cm)^2}{a_E} + a_Ev_E^2 + (b - p_{EE}r_E - p_{EO}r_O - p_{EI}r_I)v_E + c \tag{5.7b}$$

$$- p_{EI}r_I 80 - u^E + I_{ext} + \overline{\eta} \tag{5.7c}$$

$$\frac{du^E}{dt} = \alpha(\beta(v_E - V_r) - u^E) + u_{jump}r_E \tag{5.7d}$$

Figure 5.1 illustrates a comparison of the dynamics of the full network with the low-dimensional reduced system. It shows the time evolution of the external stimulus acting on all three populations (Figure 5.1 (a)), the spiking activity obtained from simulations of the full network, and the firing rates of the three populations given by the reduced description ((5.5a), (5.6a) and (5.7a) for the O, I and E-cells, respectively) and calculated from the full network simulations ($r_W = \frac{1}{N_W}\sum_{k=1}^{N_W}\sum_f \delta(t - t_f^k)$). We assume that each population is made of 3000 neurons. Although populations of

OLM cells, fast-spiking interneurons, and pyramidal cells in CA1 do not have the same size (Jinno and Kosaka, 2010; Ferguson et al., 2017; Chatzikalymniou et al., 2020), the mean-field model presumes neural populations with $N \to \infty$. The reduced description accurately captures the shape of the spiking activity of the full QIF neural network, meaning we can safely employ the reduced mean-field model to study the dynamics of the O, I, and E-cell populations.

5.2.5 Bayesian inference of connectivity parameters

We use a simulation-based inference algorithm that implements SNPE (Sequential Neural Posterior Estimation) to infer the connectivity parameters of the O-I-E network (p_{OI}, p_{IO}, p_{OE}, p_{EO}, p_{IE}, p_{EI}, p_{II}, p_{EE}) that enables it to resonate to entorhinal oscillatory theta inputs. You can find a detailed description of the inference algorithm used in Chapter 4, section 4.2.

Excitatory entorhinal inputs arrive in the CA1 region through the temporoammonic pathway, targetting the distal dendrites of pyramidal cells (Amaral and Lavenex, 2007). Therefore, we presume that the CA1 network will resonate if the E population has a natural frequency in the theta range. Bearing that in mind, we infer the connectivity parameters of the O-I-E network for which the imaginary part of the eigenvalues of the E is between 0.02512 rad/msec and 0.07539 rad/msec, which corresponds to a natural frequency between 4 and 12 Hz.

One question that has been disputed in the past few years is the contribution of OLM cells for the induction and expression of hippocampal theta rhythm (Kopell et al., 2010; White et al., 2000; Chatzikalymniou and Skinner, 2018; Giovannini et al., 2017). To address this question, we start by analyzing the posterior of p_{EI}, p_{IE},p_{II} and p_{EE} parameters while the other parameters were fixed. For the pairing stimulation protocol, we considered $p_{OE} = p_{EO} = p_{OI} = 0$, and $p_{IO} = 70$. For the no-pairing protocol, we consider $p_{OE} = p_{EO} = p_{OI} = p_{IO} = 0$. We then sampled a set of parameters from the low probability distribution, i.e. for which the network cannot resonate to theta inputs, and inferred the previously fixed O-connectivity parameters. By doing so, we investigate how OLM cells modulate the CA1 network; more specifically, how they change the robustness and power of the produced rhythm.

Inference is calculated after one round of 500 simulations. We chose uniform

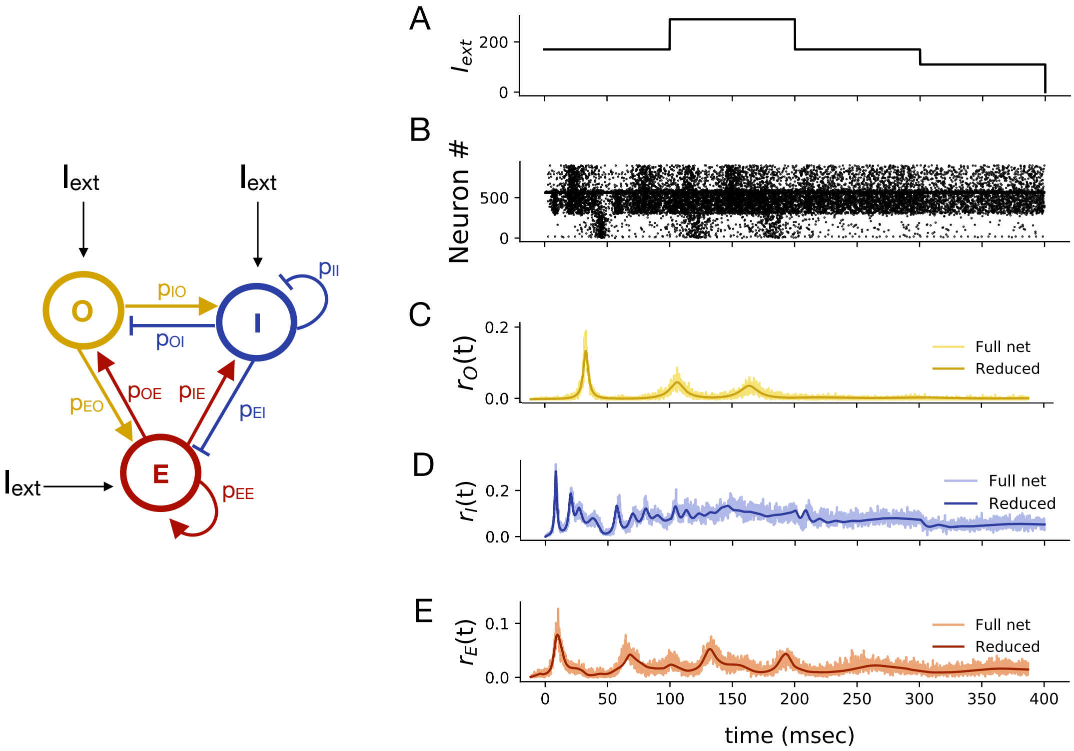

Figure 5.1: Comparison between the full network dynamics and the reduced system. Left panel: Schematic illustration of the neural network. The parameter p_{ij} denotes the connectivity strength of the population j onto the population i. The external current a acting on the different populations is denoted by I_{ext}. Right panel: **(A)** Time evolution of the stimulus I_{ext}. **(B)** Spiking activity obtained from simulations of the full network, where we randomly selected 300 neurons from each population. The first 300 neurons are OLM cells (O); the following 300 are fast-spiking inhibitory cells (I); the last 300 are pyramidal cells (E). **(C)** Firing rate of the O-cells obtained from simulations of the full and reduced system. **(D)** Firing rate of the I-cells obtained from simulations of the full and reduced system. **(E)** Firing rate of the E-cells obtained from simulations of the full and reduced system. Parameters: $N = 3000$; $\Delta = 15$; $\bar{\eta} = 25$; $p_{OI} = p_{IO} = 50$; $p_{OE} = p_{EO} = 90$; $p_{IE} = p_{EI} = 60$; $p_{II} = 30$; $p_{EE} = 60$.

distributions for all connectivity priors. These simulation specifications proved to be enough for the learning algorithm to converge to a solution.

5.3 Results

5.3.1 Estimating CA1 network connectivity

To estimate the CA1 neural populations that modulate the hippocampal response to extrinsic rhythmic inputs, we use a statistical inference tool, SNPE, to infer the posteriors of the synaptic connections of the O-I-E network that turn the network into a theta resonator. To perform inference of the posteriors, we only evaluate the behavior (natural frequency and power) of the E-cell populations, given that they are the target of the rhythmic entorhinal inputs as well as the source of current into the EC, i.e. they form the population that links the EC and CA1 region and closes the entorhinal-hippocampal loop.

We are interested in assessing the role of the OLM cells in the modulation of the natural frequency of the E-cells and power of theta oscillations during the cholinergic pairing protocol (cholinergic activation of the O-cells paired with glutamatergic activation of the I and E-cells) and during the no-pairing protocol (glutamatergic activation of I and E-cells). We start by focusing on the pairing protocol.

To simulate the state of the O-I-E network during the pairing protocol, all three populations receive an external current I_{ext} = 50 pA, and the O-to-I connection is fixed to p_{IO}=70. This follows the results obtained in chapter 2 showing that cholinergic pairing activates OLM cells, which results in strong inhibition from the O to the I-cells. First, we focus on the contributions of the E-I subnetwork, i.e. we set all connections with the O-populations (except p_{IO}) to zero, and infer the posterior distributions of p_{II}, p_{EI}, p_{IE} and p_{EE} for which the E-cells have a natural frequency in the theta range (Figure 5.2 (A)). From the resultant posteriors, we extract the mean value, which puts us in the high probability region: p_{IE} = 20.2821, p_{EI} = 64.578830, p_{II} = 45.3345, p_{EE} = 28.8861. We confirm our results by calculating the power of the network's oscillatory activity when the E-cells are submitted to a periodic input with different frequencies (Figure 5.2 (A), right panel). We see that there is a peak in power for periodic inputs with a frequency in the theta range (Figure 5.2 (A)). When we chose parameters in the low probability region ($p_{IE} = 20.2821$, $p_{EI} = 30$, $p_{II} = 45.3345$, $p_{EE} = 28.8861$), the peak of the power spectrum falls outside the theta range (grey area). These observations indicate that the network will selectively respond to oscillatory inputs with a theta frequency for connectivity parameters in the high probability region. From the inferred posteriors, we can estimate the relative contribution of the different synaptic connections to this selective response. The network's response to oscillatory theta inputs is mainly constrained by p_{EE}, p_{EI} and p_{IE}. While the posterior of p_{EE} and p_{IE} are skewed towards low values, the posterior of p_{EI} is skewed towards high values. This indicates that the bidirectional interactions between I and E-cells modulate the network's response to external rhythmic inputs differently.

We then fixed the parameters p_{IE}, p_{EI}, p_{II} and p_{EE} to its low probability regions values, and inferred the remained connectivity parameters p_{OI}, p_{OE}, p_{EO}. The learning algorithm converged to a solution. This means that adding E-O, O-E and I-O connections modulates the network in such a way that enables resonance to theta inputs (Figure 5.2 (B)). To confirm these findings, we drawn the mean values of the posterior ($p_{OI} = 51.8445$, $p_{OE} = 47.0968$, $p_{EO} = 49.0425$) and used these parameters to study the power spectrum of the network as a function of the frequency of a periodic input. We see that now the system resonates to theta inputs with parameters p_{IE}, p_{EI}, p_{II} and p_{EE} from the low probability region (Figure 5.2 (B), right panel). This result indicates that the O-cells increase the robustness of the hippocampal response to theta inputs. In other words, the O-cells increase the range of connectivity values for which the system resonates to theta inputs.

We repeated the process for the no-pairing protocol. The I and E-cells receive an external current $I_{ext} = 50$ pA, while the O-cells don't receive any external inputs. Initially, we study the contributions of the E-I subnetwork by setting all connections with the O-populations to zero. We infer the posterior distributions of p_{II}, p_{EI}, p_{IE} and p_{EE} for which the E-cells have a natural frequency in the theta range, and extract the mean value of the posterior distributions of the connectivity parameters ($p_{IE} = 30.5809$, $p_{EI} = 71.5955$, $p_{II} = 49.8003$, $p_{EE} = 34.7191$) (Figure 5.3 (A)). To confirm our results, we calculate the power spectrum of the E population when in the high and low probability region. We confirm that for parameters from the posterior high probability region (Figure 5.3 (A), purple line), the system resonates

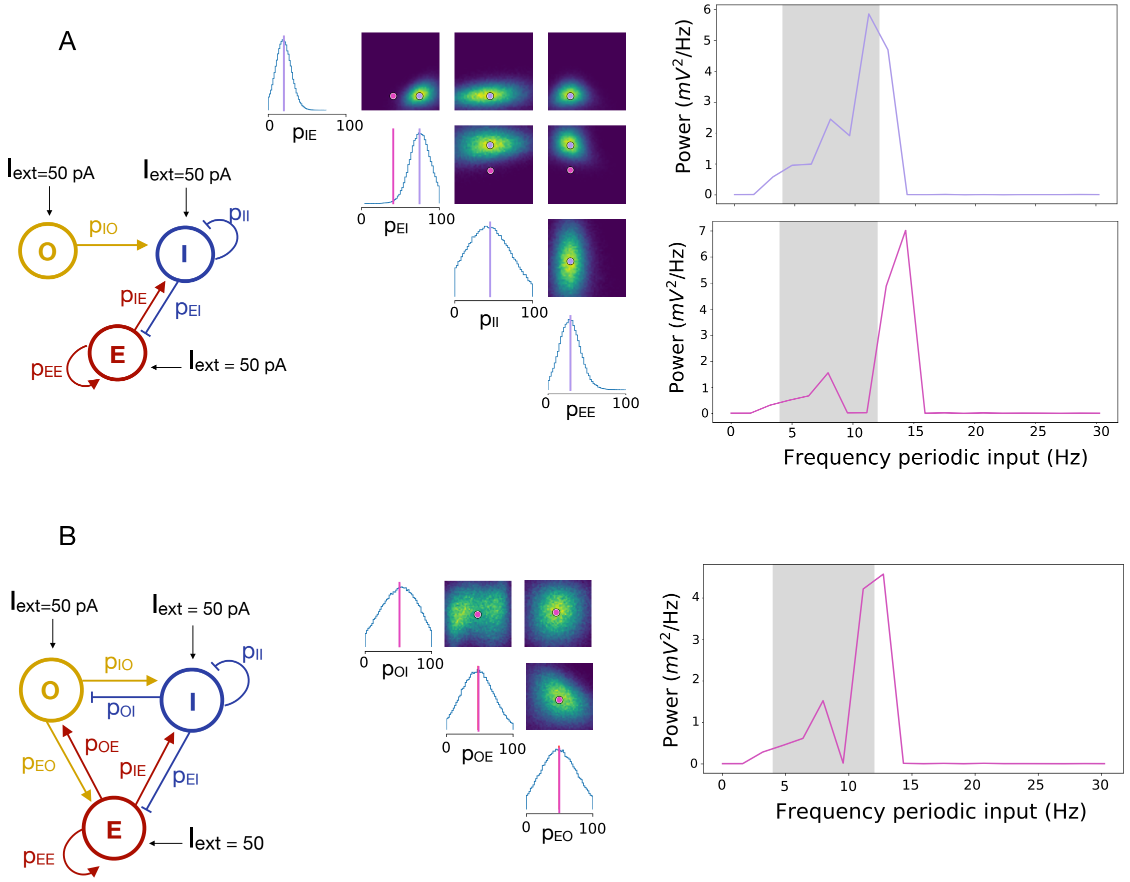

Figure 5.2: Inference of the connectivity parameters that enable resonance to periodic input with theta frequency when the hippocampal network is subjected to the pairing protocol. During pairing, all three populations (O, I and E) receive an external current I_{ext}. We fix the O-I connection p_{IO} to a high value (70). This follows the results obtained in Chapter 2 **(A)** Posterior distribution over 4 connectivity parameters (p_{IE}, p_{EI}, p_{II} and p_{EE}). We sampled parameters from the high (purple line) and low (pink line) probability region: $p_{IE} = 20.2821$, $p_{EI} = 64.578830$ (purple line) or 30 (pink line), $p_{II} = 45.3345$, $p_{EE} = 28.8861$. Using a periodic input $I_{per} = 8sin(wt) + 8$, where w defines the frequency of the input, we estimated the power spectrum of the E-cells activity obtained using parameters from the high and low probability region. **(B)** Posterior distribution over 3 connectivity parameters (p_{OI}, p_{OE} and p_{EO}). The remaining connectivity parameters were fixed to the values sampled from their low probability region ($p_{IE} = 20.2821$, $p_{EI} = 30$, $p_{II} = 45.3345$, $p_{EE} = 28.8861$). We sampled from their posterior the parameters from the high probability region $p_{OI} = 51.8445$, $p_{OE} = 47.0968$ and $p_{EO} = 49.0425$ (pink line), and calculated the respective power spectrum.

to theta inputs. For parameters from the low probability region (Figure 5.3 (A), pink line), the system resonates to inputs with a frequency outside the theta range. We then fixed the parameters p_{IE}, p_{EI}, p_{II} and p_{EE} in their low probability region, and infer the connectivity parameters involving the O-cells (p_{OI}, p_{IO}, p_{OE}, and p_{EO}). Similarly, as for the pairing case, adding connections with the O-cells makes the system resonate at theta frequencies (Figure 5.3 (B)).

5.3.2 The hippocampus as a theta rhythm generator

It is well established that the CA1 region contains the circuitry necessary for the generation of theta oscillations (Goutagny et al., 2009; Ferguson et al., 2017; Chatzikalymniou et al., 2020; Giovannini et al., 2017). Yet, recent *in vitro* studies indicate that, in a septal-entorhinal-hippocampal network*in vitro*, theta rhythm induced by co-pairing septal cholinergic and SC inputs originates in the EC structure (Gu and Yakel, 2017), and not in the hippocampal region. Furthermore, it was also shown that repeated co-pairing of cholinergic and SC inputs potentiates SC-PYR and PYR-OLM synapses (Gu et al., 2020).

In this section, we inquire if changes in the SC-PYR and PYR-OLM synapses can change the mechanisms of theta generation in the septal-entorhinal-hippocampal circuit. In particular, we test the possibility of changes in the mentioned synapses enabling the CA1 region to generate theta oscillations when the co-pairing stimulation protocol is performed. For that, we consider that the potentiation of the SC-PYR and PYR-OLM synapses translates into an increase of the magnitude of the external current acting on the E-cell and of the connectivity parameter p_{OE}, respectively. For the remaining connectivity parameters, we adopt the values inferred in the previous section, i.e. the parameters for which the CA1 network resonates to theta inputs ($p_{IE} = 20.2821$, $p_{EI} = 30$, $p_{II} = 45.3345$, $p_{EE} = 28.8861$, $p_{OI} = 51.8445$, $p_{IO} = 70$, $p_{OE} = 47.0968$, $p_{EO} = 49.0425$).

We plot a two-parameter bifurcation diagram of the E-I-O system when all the populations of the network receive an external current I_{ext}=50 pA (see section 5.2 for justification). We see that if the magnitude of the external current acting on E and the strength of the E-O synapse p_{OE} increase, the hippocampal network enters an oscillatory regime without the need for external periodic inputs (Figure 5.4 (B)).

Suppose the system is in the non-oscillatory region. In that case, it will only produce theta oscillations if, besides an external current acting on the O, I and E-cells, the E-cells receive a periodic input $I_{per} = 8sin(wt) + 8$ with a frequency w in

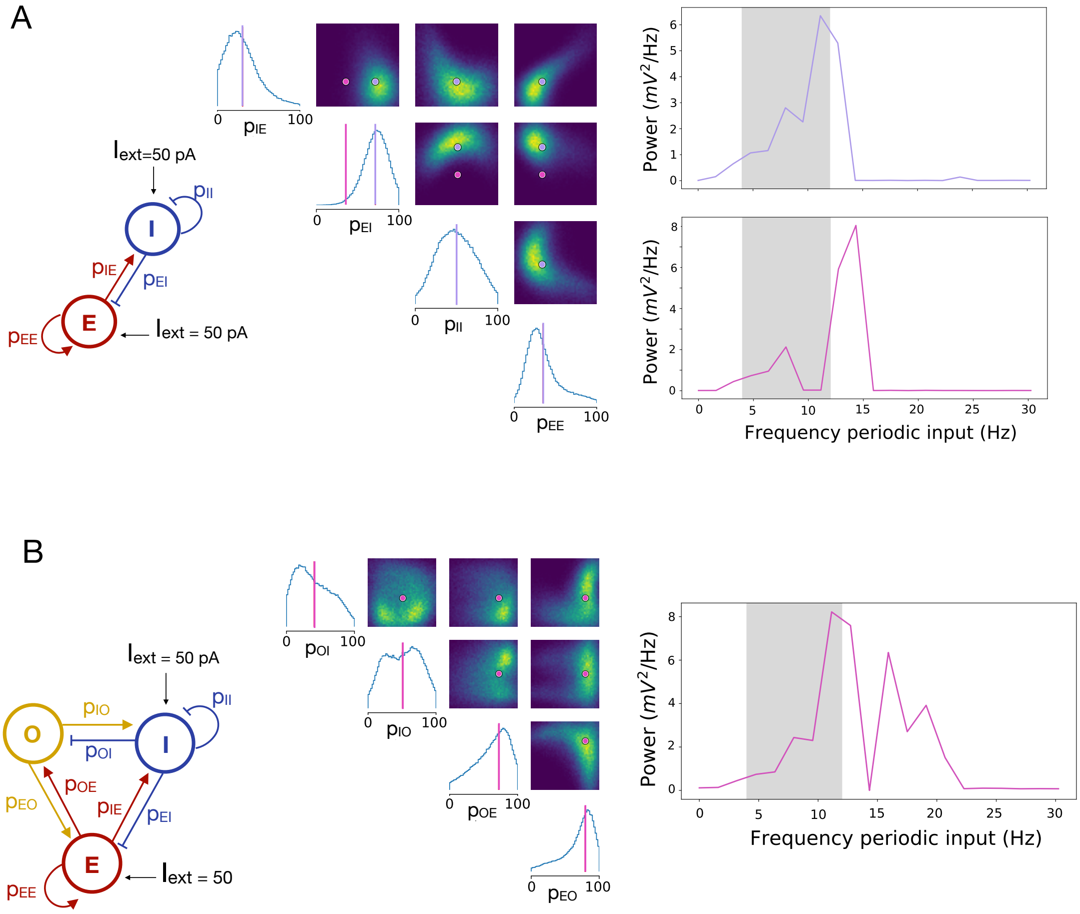

Figure 5.3: Inference of the connectivity parameters that enable resonance to periodic input with theta frequency when the hippocampal network is subjected to the no-pairing protocol. During the no-pairing protocol, the E and I populations receive an external current I_{ext}, while the O-cell do not receive any extrinsic stimulus. **(A)** Posterior distribution over 4 connectivity parameters (p_{IE}, p_{EI}, p_{II} and p_{EE}). We sampled parameters from the high (purple line) and low (pink line) probability region: $p_{IE} = 30.5809$, $p_{EI} = 71.5955$ (purple line) or 35 (pink line); $p_{II} = 49.8003$; $p_{EE} = 34.7191$. Using a periodic input $I_{per} = 8sin(wt) + 8$, we estimated the power spectrum of the E-cells activity obtained using parameters from the high and low probability region. **(B)** Posterior distribution over 4 connectivity parameters (p_{OI}, p_{IO}, p_{OE} and p_{EO}). The remaining connectivity parameters were fixed to the values sampled from their low probability region ($p_{IE} = 30.5809$, $p_{EI} = 35$; $p_{II} = 49.8003$; $p_{EE} = 34.7191$). We sampled from their posterior the parameters from the high probability region, $p_{OI} = 40.7411$, $p_{IO} = 50.9074$ $p_{OE} = 72.2952$, $p_{EO} = 79.4703$ (pink line), and calculated the resultant power spectrum.

the theta range. The oscillations generated have the same frequency as the periodic input (11 Hz) and a power of 8.7 mV^2/Hz. On the other hand, if the system is in the oscillatory regime, it will produce oscillations of similar power independently of receiving periodic input or not (see Figure 5.4 (B)). However, if the system is in the oscillatory regime, pairing I_{ext} with a periodic theta input I_{per} produced oscillations outside the theta range (Figure 5.4 (B), right panel 1). These results indicate that the mechanisms for the generation of theta in a septo-entorhinal-hippocampal circuit might differ before and after inducing potentiation of the SC-PYR and PYR-OLM synapses.

Gu and Yakel also observed that after repeatedly inducing theta in a septo-entorhinal-hippocampal circuit using the co-pairing protocol and inducing potentiation of the mentioned hippocampal synapses, they could generate theta by activating the SC pathway alone (Gu and Yakel, 2017). To further examine how potentiation of the hippocampal synapses is altering the mechanisms of theta generation, we repeated the previous analysis considering that the system is being subjected to the no-pairing protocol. That is, we plot a two-bifurcation diagram of the E-I-O system when the E and I populations receive an external input $I_{ext} = 50$ pA and the O population does not receive any external input. Once again, if the magnitude of the external current acting on E and the strength of the E-O synapse p_{OE} increase, the network generates oscillations without any external periodic drive (Figure 5.5).

If the system in the non-oscillatory region, it will only produce theta oscillations if the E-cells receive a periodic input $I_{per} = 8sin(wt) + 8$ with a frequency w in the theta range (see Figure 5.5 (B)). The oscillations generated have the same frequency as the periodic input (11 Hz) and a power of 8.2 mV^2/Hz. If the system is in the oscillatory regime, it can autonomously generate oscillations with a frequency of 11.1 Hz, i.e. in the theta range; if besides the external current acting on the E and I-cells, the E-cells receive a periodic input with a frequency of 12 Hz, it produces oscillations with the same frequency. Regarding the power of the oscillations generated, this is bigger when the system does not receive oscillatory inputs I_{per} (14.4 mV^2/HZ) than when it does (11.2 mV^2/Hz). These results confirm that induction of plasticity in the hippocampal region can change the mechanisms of theta generation in a septo-entorhinal-hippocampal circuit.

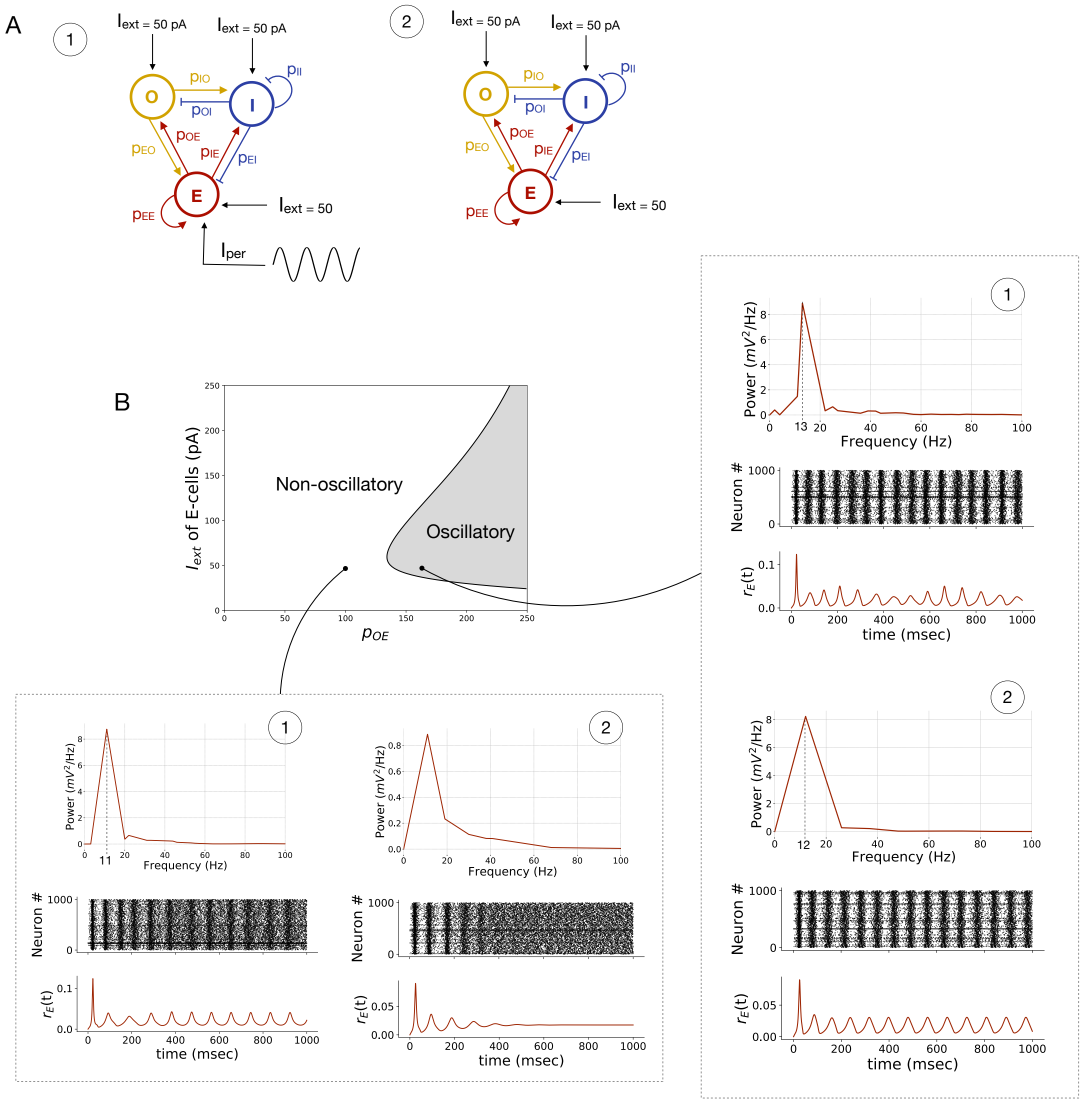

Figure 5.4: Evaluating the effect that an increase of I_{ext} acting on the E-cell and of p_{OE} has on the mechanisms of hippocampal theta rhythm generation when the hippocampal network is subjected to the co-activation protocol. (A) Schematic illustration of the O-I-E network when subjected to the co-activation protocol paired (1) or not (2) with a periodic input with theta frequency acting on the E-cells. **(B)** Two-parameter bifurcation diagram of the E-I-O system, with the external current acting on the E-cells, I_{ext}, and the strength of the connection between the O and E population, p_{OE} as bifurcation parameters. We simulate the activity of the E-cells when the system is in the non-oscillatory or oscillatory region, with or without paired periodic inputs.

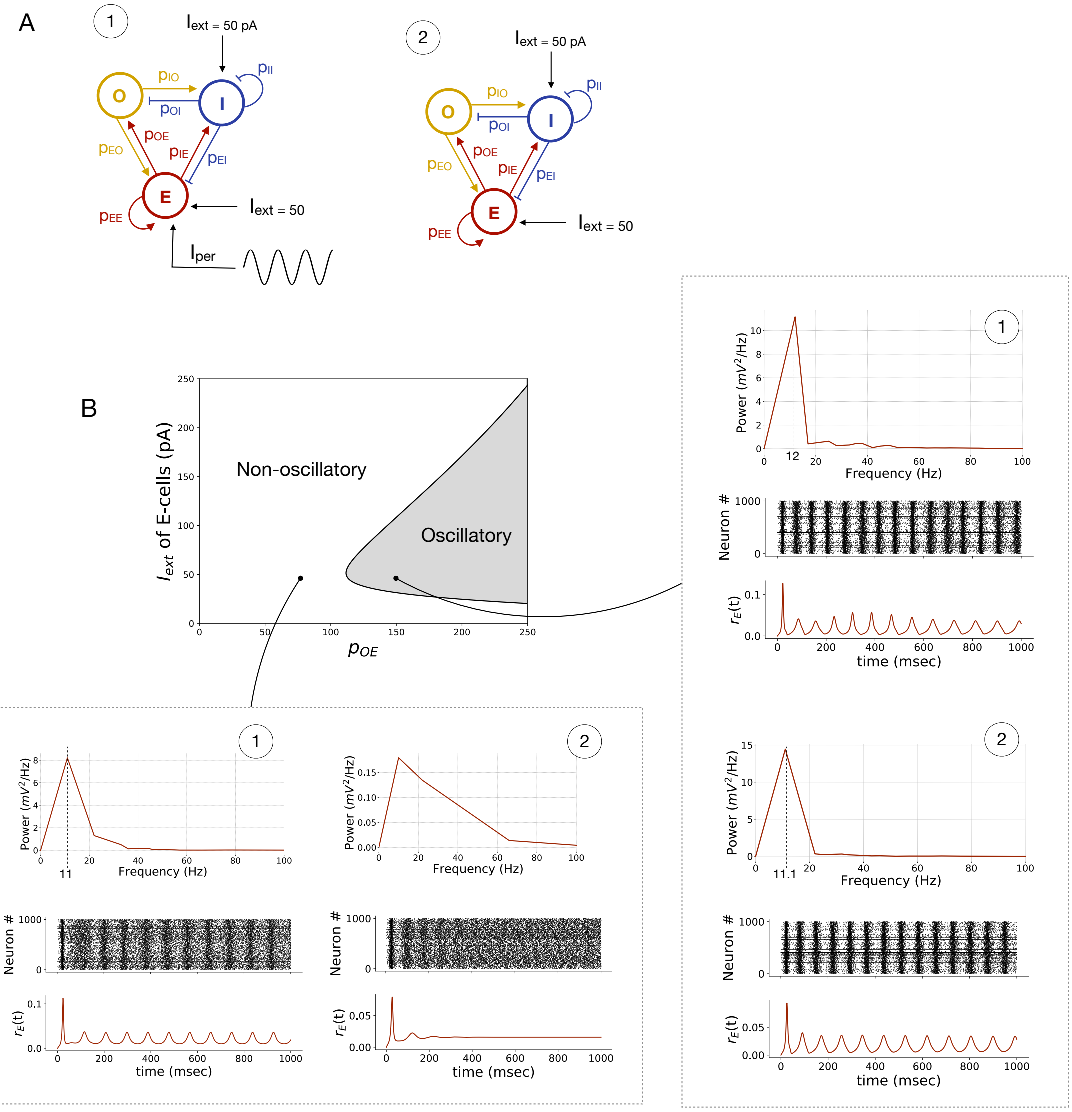

Figure 5.5: Evaluating the effect that an increase of I_{ext} acting on the E-cell and of p_{OE} has on the mechanisms of hippocampal theta rhythm generation when the O-cells do not receive any extrinsic input. (A) Schematic illustration of the O-I-E network when subjected to the co-activation protocol paired (1) or not (2) with a periodic input with theta frequency acting on the E-cells. **(B)** Two-parameter bifurcation diagram of the E-I-O system, with the external current acting on the E-cells, I_{ext}^{E}, and the strength of the connection between the O and E population, p_{OE} as bifurcation parameters. We simulate the activity of the E-cells when the system is in the non-oscillatory or oscillatory region, with or without paired periodic inputs.

5.4 Discussion

In this chapter, we used a network model of the hippocampal CA1 region to study how its connectivity modulates the hippocampal responses to external periodic inputs. This is particularly important in light of recent experimental work suggesting that in a septal-hippocampal-entorhinal circuit, rhythmic activity is not being generated in the hippocampus and that instead, it originates in the intrinsic entorhinal circuit and is fed back to the hippocampus, probably through the temporoammonic pathway (Gu and Yakel, 2017). Moreover, the same study indicates that induction of theta in the tri-culture preparation requires co-paired activation of cholinergic and SC inputs and that SC stimulation alone is not sufficient to induce theta.

Assuming that the theta rhythm is not originating in the hippocampus and that the CA1 region receives rhythmic theta inputs from the EC, we analyze the connectivity parameters of a CA1 network composed of OLM cells (O), fast-spiking interneurons (I), and pyramidal cells (E) for which the network resonates to rhythmic theta inputs. Given that the EC rhythmic inputs target the CA1 E-cells and that, in turn, the E-cells project back to the EC network closing the entorhinal-hippocampal circuit, we assume that the E-cells must resonate to the rhythmic entorhinal inputs for theta to be maintained in the full circuit. Generally speaking, a given system will resonate under the influence of an external force if its natural frequency is equal to the frequency of the external input. Therefore, we were interested in finding the different connectivity configurations of the network for which the E-cells have a natural frequency in the theta range.

We consider two distinct situations: when the hippocampal circuit is subjected to paired activation of cholinergic and SC inputs and when subjected to SC inputs alone. Given the contrasting ideas regarding the role of OLM cells in the generation and maintenance of the hippocampal theta rhythm (Kopell et al., 2010; White et al., 2000; Chatzikalymniou and Skinner, 2018), for each of the mentioned situations, we ascertain the role of the O-cells by considering the E-I subnetwork and seeing how adding connections with the O-populations changes the behavior of the network.

Our results show that while the E-I subnetwork can resonate with rhythmic inputs with theta frequency, adding connections with the O-cells increases the robustness of the network. This is true when we subjugate the network to paired activation of the O-cells and the E and I cells or activation of the E and I cells alone. Such observations indicate that cholinergic activation of the O-cells is unnecessary for the CA1 region to resonate with extrinsic theta inputs. Instead, we hypothesize that they might only play a role in the modulation of the hippocampal excitability (see chapter 2) that gates the generation of theta rhythm in the EC.

Experimental and theoretical studies have shown that the CA1 region has the necessary circuitry to generate theta oscillations intrinsically (Goutagny et al., 2009; Ferguson et al., 2017; Chatzikalymniou et al., 2020; Giovannini et al., 2017). Yet, Gu and colleagues observations indicate that in a septo-entorhinal-hippocampal circuit, theta is originating in the EC and not the hippocampal region, and that the hippocampus is responding to theta inputs coming through the temporoammonic pathway (Gu and Yakel, 2017). We confirm that if the connectivity of the CA1 O-I-E network is such that the network resonates to entorhinal theta inputs, paired cholinergic and SC inputs (or SC inputs alone) do not initiate theta oscillations in the CA1 region. Furthermore, we investigate how changes in the magnitude of the external current acting on the E-cells and the E-O connection, p_{OE}, modify the mechanisms of theta generation. This follows experimental results showing that repeated paired activation of cholinergic and SC inputs potentiates the SC-PYR and PYR-OLM hippocampal synapses (Gu and Yakel, 2017; Gu et al., 2020). According to our model, potentiation of the hippocampal synapses enables the generation of oscillations in the hippocampal region. In other words, if the external current acting on the E-cells and/or the connectivity p_{OE} increase, paired co-activation of O cells and E and I cells (or activation of the E and I cells alone) generates theta rhythm in the E-I-O network, without the need of extrinsic periodic inputs.

Note that these are preliminary results, and supplementary simulations are required for a complete analysis. For example, when inferring the connectivity parameters that enable the E-cell with theta resonant properties, we did not consider the effects of potentiation of the hippocampal SC-PYR and OLM-PYR synapses. Additional simulations are required to verify how changes in the strength of these synapses alter the resonant properties of the network. Moreover, we did not consider the different coupling strengths that the different external inputs, I_{ext} and I_{per}, can have on the network.

Overall, our results indicate that the mechanisms for the generation of theta in a septo-entorhinal-hippocampal circuit differ before and after potentiation of the SC-PYR and PYR-OLM synapses is induced. Before the hippocampal synapses are potentiated, paired cholinergic and SC inputs (or SC inputs alone) cannot initiate theta in the local hippocampal circuit, and CA1 merely responds to rhythmic inputs from the EC. However, if the strength of the E-O synapse and/or the external current acting on the E-cells increase, co-pairing or SC activation alone can drive the system into an oscillatory regime with theta frequency.

6 | Conclusion and future perspectives

This thesis was set out to investigate the mechanisms of theta induction and expression in a septal-hippocampal-entorhinal circuitry. We use computational models to study the intrinsic properties of each region and how they can contribute to the generation and maintenance of theta rhythm in the hippocampal formation.

Despite being known that three brain regions - septum, hippocampus, and entorhinal cortex - are necessary for the generation of theta rhythm in the hippocampal formation, it is not clear what role each of them plays in the interplay that gives rise to synchronous activity with a theta frequency. Thanks to the groundbreaking experimental work of Gu and Yakel (2017), where they established an *in vitro* septal-entorhinal-hippocampal brain co-culture preparation, it was possible to study how theta is generated and how the activity flows among the three regions during theta generation and propagation. It was found that while activation of septal cholinergic inputs or activation of SC inputs alone could not induce theta, tightly paired co-activation of the two pathways could readily induce theta in the circuit. Repeated pairing of cholinergic and SC inputs potentiated the EPSCs of CA1 OLM and pyramidal cells in the deep layers of the EC. Moreover, SC stimulation alone could then give rise to theta oscillations in the hippocampal-entorhinal circuit. Experiments also revealed that the generation of theta oscillations depends on the activation of $\alpha7$ nAChRs and mAChRs in the hippocampus (on OLM$\alpha2$ and CA1 pyramidal neurons, respectively), and NMDARs on the EC. In contrast, re-expression only depends on the activation of the NMDARs. Experiments also show that theta rhythmic inputs first appear in the deep layers of the EC, then spread to the superficial layers, and finally to the hippocampal slm layer and to hippocampal pyramidal neurons, which project back to the deep layers of the EC and close the hippocampal-entorhinal circuit (Gu and Yakel, 2017, 2011; Gu et al., 2017, 2020). Several questions arise from these results. First, how the pairing of acetylcholine and glutamatergic hippocampal inputs gates local plasticity and facilitate theta rhythm generation. Second, what are the intrinsic properties of the entorhinal circuit that permit theta oscillations to arise. And finally, how do entorhinal rhythmic inputs drive the hippocampus into an oscillatory regime. To answer these questions, we used a combination of local biophysical and network models.

We started by using a biophysical model to study how cholinergic inputs paired with SC stimulation modulate synaptic strength in the hippocampus. We constructed a minimal circuit with a single compartment spiking OLM cells with $\alpha7$ nAChRs, a fast-spiking interneuron with AMPA and $GABA_A$ receptors, and the pyramidal cell proximal dendritic compartment with AMPA, NMDA, and $GABA_A$ receptors. Our results show that recurrent cholinergic activation of $\alpha7$ nAChR expressed in OLM$\alpha2$ interneurons can potentiate SC-evoked CA1 pyramidal EPSCs by inhibiting fast-spiking interneurons that provide feedforward inhibition onto CA1 pyramidal cells. These results suggest that septal cholinergic inputs regulate hippocampal plasticity, promoting the generation of theta oscillations instead of pacing theta frequency. This is in accordance with optogenetic studies showing that changes in the firing frequency of septal cholinergic inputs do not significantly change the frequency of hippocampal theta (Dannenberg et al., 2015; Vandecasteele et al., 2014), and that after blockade of septal inputs to the hippocampus, the *in vivo* hippocampus was still able to generate theta with simultaneous excitation and disinhibition of the hippocampus (Colom et al., 1991).

In our modeling work, we did not consider the action of mAChR on the CA1 pyramidal cell in our model. The dynamics of these receptors is challenging to modulate due to the multitude of different outcomes and protein kinase cascades that their activation entails. We believe that cholinergic activation of mAChR mainly affects the pyramidal cell's excitability, enhancing the induction of plasticity. Still, more experimental and computational results are necessary to confirm this hypothesis. Future work also includes expanding our pyramidal cell model to include more dendritic compartment, namely a distal dendritic compartment, and the spiking soma to study how direct inhibitory inputs from the OLM interneurons into slm affects the induction of plasticity at the proximal dendritic compartment and the firing activity of the pyramidal cell and consequent neurotransmitter release into EC. It would also be interesting to include a PYR-OLM connection and model plasticity induction at this synapse, which is also potentiated following repeated cholinergic and SC inputs pairing. In particular, we would like to study how plasticity at this site is induced and how it affects the induction of plasticity in the SC-PYR synapse.

Based on the results obtained, we hypothesize that the pairing of septal cholinergic and SC inputs promotes the generation of hippocampal theta rhythm by increasing the hippocampal excitability, which presumably results in an increased excitation onto the deep layers of the EC.

We next built a network model of the entorhinal circuit to study how an increase in the hippocampal excitatory drive can trigger synchronous activity with a theta frequency in this brain region. Our results suggest that connections between stellate cells and pyramidal cells can synchronize the activity of the network. Additionally, connections between pyramidal cells and fast-spiking interneurons modulate the frequency of oscillations. The stellate cells are endowed with currents that give rise to subthreshold oscillations with theta frequency. Therefore, they may also indirectly control the frequency of theta rhythm in the EC by selectively resonating to inputs with a theta frequency. Our model also argues that slow S-to-I excitatory synapses can promote the generation of theta oscillation in the EC. Although this observation agrees with previous experimental results indicating that NMDARs in the EC play a crucial role in the generation of theta in the hippocampal formation (Gu and Yakel, 2017; Gu et al., 2017), a more detailed and accurate description of these receptors is necessary to take any further conclusions from our model.

Finally, we built a network model of the CA1 region that included inhibitory OLM and fast-spiking interneurons and excitatory pyramidal cells. We inferred the connectivity for which the system has a natural frequency in the theta range. This allowed us to study how the connectivity of the hippocampal neurons modulates the network's response to entorhinal rhythmic inputs. According to our results, a minimal network of pyramidal cells and fast-spiking interneurons can amplify external rhythmic inputs with theta frequency. Connections from fast-spiking interneurons to pyramidal cells seem to be particularly important in modulating this response.

The OLM cells increase the robustness of the network, i.e., with configurations of the E-I network that would not resonate at theta, we can make the system resonate by including connections with the O-cells. We also found that if the hippocampal connectivity is such that it will resonate to inputs with theta frequency, it cannot intrinsically generate theta oscillations as a response to the pairing of cholinergic and SC inputs (or to SC inputs alone) unless the E-O synapse is strong enough. This seems to indicate that the mechanisms of induction and expression of hippocampal theta rhythm are different. For the induction of hippocampal theta, the rhythmic activities are generated in the EC circuit as a response to increased excitatory hippocampal inputs, which then feedback to the hippocampus driving the hippocampal circuit into a resonant regime. When it comes to the expression, the hippocampal formation may be using a similar mechanism, or the hippocampus might be generating theta rhythm intrinsically as a response to SC inputs. This oscillatory activity can then propagate to the EC, or the hippocampus and EC can function as two coupled oscillators. To explore these ideas, one would need to couple the entorhinal and hippocampus network described in chapters 4 and 5, respectively, and study how rhythmic activity flows in the entire circuit. Another possible approach is to study the macroscopic Phase-Response Curve (mPRC) of the different populations involved.

PRCs illustrate transient changes in an oscillatory system's period induced by small perturbations as a function of the phase at which the perturbation is induced. In other words, it quantifies by how much a spike of a regular spiking neuron is advanced/delayed as a function of the timing of a small perturbation delivered to that neuron. From PRCs, we can extract useful information regarding the excitability type and synchronization properties of different neuron types. For example, a biphasic PRC indicates that an excitatory input can delay or advance the firing of the next spike, depending on the phase at which it's delivered to the neuron. Neurons that present this type of PRC curves are known to synchronize with fast excitatory synapses (Acker et al., 2003; Hansel et al., 1995; Stiefel and Ermentrout, 2016).

Similarly, we can derive the mPRC of a population of identical neurons to determine how the phase of the global oscillation of a macroscopic system respond to incoming perturbations acting on a population of neurons (Dumont et al., 2017) Preliminary results show that populations of entorhinal stellate (S) and pyramidal

(E) cells both have biphasic mPRCs (Figure 6.1), which suggests that they can synchronize with external rhythmic excitatory inputs. This indicates that two intercoupled populations of oscillating S and E-cells can synchronize with each other, as we have seen in chapter 4. Moreover, it suggests that external excitatory inputs acting on the E-cells, presumably from the hippocampal region, can synchronize a population of pyramidal entorhinal cells. Still, it does not give us any information about the phase shifts that arise when we couple the hippocampus and EC. The mPRC has been used to study the phase shifts that occur in a system of identical intercoupled networks (Dumont and Gutkin, 2019). However, to our knowledge, no methods have yet been developed that allow us to quantify the phase shifts that arise in intercoupled populations of non-identical neurons. Understanding how regularly firing neural hippocampal and entorhinal populations synchronize with each other is a crucial step towards studying the maintenance of theta rhythm in a closed hippocampal-entorhinal loop.

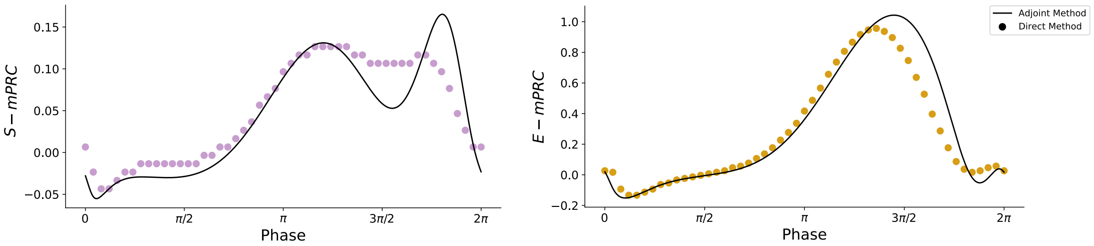

Figure 6.1: Macroscopic phase-response curve (mPRC) of the stellate cells (S) and pyramidal cells (E) population using direct simulations and the adjoint method. Both population have a mPRC with a biphasic phase, indicating that periodic excitatory inputs into the S and E-cells facilitates the entrainment of the circuit (Acker et al., 2003)

The present study sheds light on the underlying mechanisms of hippocampal theta rhythm generation. To our knowledge, this is the first computational study that addresses the role of all three brain regions (medial septum, hippocampus, and entorhinal cortex) involved in the induction and expression of hippocampal theta rhythm. We combined minimal, detailed models to establish a cellular basis for how cholinergic action can modulate the hippocampal network and promote the induction of theta, with network models that put into evidence the intrinsic properties of the hippocampus and entorhinal cortex that foster theta generation and maintenance, thus establishing a link between single neuron computation and computation at the network level.

Bibliography

Abarbanel, H., Gibb, L., Huerta, R., and Rabinovich, M. (2003). Biophysical model of synaptic plasticity dynamics. *Biological Cybernetics*, 89(3):214–226.

Acker, C., Kopell, N., and White, J. (2003). Synchronization of strongly coupled excitatory neurons: relating network behavior to biophysics. *Journal of Computational Neuroscience*, 15:71–90.

Ali, A. B., Deuchars, J., Pawelzik, H., and Thomson, A. M. (1998). Ca1 pyramidal to basket and bistratified cell epsps: dual intracellular recordings in rat hippocampal slices. *The Journal of Physiology*, 507(1):201–217.

Alonso, A. and García-Austt, E. (1987). Neuronal sources of theta rhythm in the entorhinal cortex of the rat. i. laminar distribution of theta field potentials. *Experimental Brain Research*, 67(3):493–501.

Alonso, A. and Klink, R. (1993). Differential electroresponsiveness of stellate and pyramidal-like cells of medial entorhinal cortex layer ii. *Journal of Neurophysiology*, 70(1):128–143.

Amaral, D. and Kurz, J. (1985). An analysis of the origins of the cholinergic and noncholinergic septal projections to the hippocampal formation of the rat. *The Journal of Comparative Neurology*, 240(1):37–59.

Amaral, D. and Lavenex, P. (2007). Hippocampal neuroanatomy. In Andersen, P., Morris, R., Amaral, D., Bliss, T., and O'Keefe, J., editors, *The hippocampus book*, chapter 3, pages 37–55.

Amaral, D. and Witter, M. P. (1989). The three-dimensional organization of the hippocampal formation: a review of anatomical data. *Neuroscience*, 31(3):571–91.

Andrásfalvy, B. K., Smith, M. A., Borchardt, T., Sprengel, R., and Magee, J. C. (2003). Impaired regulation of synaptic strength in hippocampal neurons from glur1-deficient mice. *The Journal of Physiology*, 552(1):35–45.

Ang, G. W. Y., Tang, C. S., Hay, Y. A., Zannone, S., Paulsen, O., and Clopath, C. (2021). The functional role of sequentially neuromodulated synaptic plasticity in behavioural learning. *PLoS Computational Biology*, 17(6):e1009017.

Appleby, P. A. and Elliott, T. (2005). Synaptic and temporal ensemble interpretation of spike-timing-dependent plasticity. *Neural Computation*, 17(11):2316–2336.

Arriagada, P., Growdown, J. H., Hedley-Whyre, E., and Hyman, B. (1992). Neurofibrillary tangles but not senile plaques parallel duration and severity of alzheimer's disease. *Neurology*, 42(3):631–639.

Artola, A. and Singer, W. (1993). Long-term depression of excitatory synaptic transmission and its relationship to long-term potentiation. *Trends in Neuroscience*, 16(11):480–487.

Asztely, F., Wigström, H., and Gustafsson, B. (1992). The relative contribution of nmda receptor channels in the expression of long-term potentiation in the hippocampal ca1 region. *European Journal of Neuroscience*, 4(8):681–690.

Aussel, A. (2018). A detailed anatomical and mathematical model of the hippocampal formation for the generation of sharp-wave ripples and theta-nested gamma oscillations. *Journal of Computational Neuroscience*, 45(3):207–221.

Badoual, M., Zou, Q., Davison, A. P., Rudolph, M., Bal, T., Frégnac, Y., and Destexhe, A. (2006). Biophysical and phenomenological models of multiple spike interactions in spike-timing dependent plasticity. *International Journal of Neural Systems*, 16(2):79–97.

Barria, A., Muller, D., Derkach, V., Griffith, L. C., and Soderling, T. R. (1997). Regulatory phosphorylation of ampa-type glutamate receptors by cam-kii during long-term potentiation. *Science*, 276(5321):2042–2045.

Bartsch, T., Schonfeld, R., Muller, F. J., Alfke, K., Leplow, B., Aldenhoff, J., Deuschl, G., and Koch, J. M. (2010). Focal lesions of human hippocampal ca1 neurons in transient global amnesia impair place memory. *Science*, 328(5984):1412–5.

Bear, M. F. and Malenka, R. C. (1994). Synaptic plasticity: Ltp and ltd. *Current Opinion in Neurobiology*, 4(3):389–399.

Berg, D. K. and Conroy, W. (2002). Nicotinic alpha 7 receptors: synaptic options and downstream signaling in neurons. *Journal of Neurobiology*, 53(4):512–23.

Berry, S. D. and Thompson, R. F. (1978). Prediction of learning rate from the hippocampal electroencephalogram. *Science*, 200(4347):1298–300.

Bezaire, M. and Soltesz, I. (2013). Quantitative assessment of ca1 local circuits: knowledge base for interneuron-pyramidal cell connectivity. *Hippocampus*, 23:751–785.

Bezaire, M. J., Raikov, I., Burk, K., Vyas, D., and Soltesz, I. (2016). Interneuronal mechanisms of hippocampal theta oscillations in a full-scale model of the rodent ca1 circuit. *eLife*, 5:e18566.

Bi, G.-Q. and Wang, H.-X. (2002). Temporal adymmetry in spike timing-dependent synaptic plasticity. *Physiology and Behavior*, 77(4-5):551–555.

Bliss, T. and Lømo, T. (1973). Long-lasting potentiation of synaptic transmission in the dentate area of the anaesthetized rabbit following stimulation of the perforant path. *Journal of Physiology*, 232:331–356.

Booker, S. A. and Vida, I. (2018). Morphological diversity and connectivity of hippocampal interneurons. *Cell and Tissue Research*, 373(3):619–641.

Brandon, M. P., Koenig, J., Leutgeb, J. K., and Leutgeb, S. (2014). New and distinct hippocampal place codes are generated in a new environment during septal inactivation. *Neuron*, 82(4):789–796.

Brankack, J., Stewart, M., and Fox, S. E. (1993). Current source density analysis of the hippocampal theta rhythm: associated sustained potentials and candidate synaptic generators. *Brain Research*, 615:310–327.

Buckmaster, C. A., Eichenbaum, H., Amaral, D. G., Suzuki, W. A., and Rapp, P. R. (2004a). Entorhinal cortex lesions disrupt the relational organization of memory in monkeys. *Journal of Neuroscience*, 24(44):9811–9825.

Buckmaster, P., Alonso, A., Canfield, D., and Amaral, D. (2004b). Dendritic morphology, local circuitry, and intrinsic electrophysiology of principal neurons in the entorhinal cortex of macaque monkeys. *The Journal of Comparative Neurology*, 470(3):317–329.

Buhler, A. and Dunwiddie, T. (2001). Regulation of the activity of hippocampal stratum oriens interneurons by $\alpha 7$ nicotinic acetylcholine receptors. *Neuroscience*, 106(1):55–67.

Burkitt, A. N., Gilson, M., and van Hemmen, J. L. (2007). Spike-timing-dependent plasticity for neurons with recurrent connections. *Biological Cybernetics*, 95:533–546.

Burnashev, N., Zhou, Z., Neher, E., and Sakmann, B. (1995). Fractional calcium currents through recombinant glur channels of the nmda, ampa and kainate receptor subtypes. *The Journal of Physiology*, 485(2):403–418.

Buzsáki, G. (2002). Theta oscillations in the hippocampus. *Neuron*, 33(3):325–340.

Buzsáki, G., Leung, L., and Vanderwolf, C. (1983). Cellular bases of hippocampal eeg in the behaving rat. *Brain Research Reviews*, 6(2):139–171.

Canto, C. B., Wouterlood, F. G., and Witter, M. P. (2008). What does the anatomical organization of the entorhinal cortex tell us? *Neural Plasticity*, 2008:18.

Castro, N. G. and Albuquerque, E. (1995). alpha-bungarotoxin-sensitive hippocampal nicotinic receptor channel has a high calcium permeability. *Biophysical Journal*, 68(2):516–524.

Chatzikalymniou, A. P., Gumus, M., Lunyov, A., Rich, S., Lefebvre, J., and Skinner, F. K. (2020). Linking minimal and detailed models of ca1 microcircuits reveals how theta rhythms emerge and how their frequencies are controlled. *bioRxiv*.

Chatzikalymniou, A. P. and Skinner, F. K. (2018). Deciphering the contribution of oriens-lacunosum/moleculare (olm) cells to intrinsic θ rhythms using biophysical local field potential (lfp) models. *eNeuro*, 5(4).

Chenani, A., Schlesiger, M. S. M. I., Leutgeb, J., Leutgeb, S., and Leibold, C. (2019). Hippocampal ca1 replay becomes less prominent but more rigid without inputs from medial entorhinal cortex. *Nature Communications*, 10:1341.

Chevaleyre, V. and Piskorowski, R. (2014). Modulating excitation through plasticity at inhibitory synapses. *Frontiers in Cellular Neuroscience*, 8.

Cole, A. and Nicoll, R. (1983). Acetylcholine mediates a slow synaptic potential in hippocampal pyramidal cells. *Science*, 221(4617):1299–301.

Colgin, L. (2013). Mechanisms and functions of theta rhythms. *Annual Review of Neuroscience*, 36:295–312.

Colgin, L. (2016). Rhythms of the hippocampal network. *Nature Reviews Neuroscience*, 17(4):239–249.

Collingridge, G., Kehl, S., and McLennan, H. (1983). Excitatory amino acids in synaptic transmission in the schaffer collateral-commissural pathway of the rat hippocampus. *The Journal of Physiology*, 334(1):33–46.

Colom, L., Nassif-Caudarella, S., Dickson, C. T., Smythe, J., and Bland, B. (1991). In vivo intrahippocampal microinfusion of carbachol and bicuculline induces theta-like oscillations in the septally deafferented hippocampus. *Hippocampus*, 1(4):381–390.

Couey, J., Witoelar, A., Zhang, S., Zheng, K., Ye, J., Dunn, B., Czajkowski, R., Moser, M.-B., Moser, E., Roudi, Y., and Witter, M. (2013). Recurrent inhibitory circuitry as a mechanism for grid formation. *Nature Neuroscience*, 16:318–324.

Cummings, J. A., Mulkey, R. M., Nicoll, R. A., and Malenka, R. C. (1996). ca^{2+} signalling requirements for long-term depression in the hippocampus. *Neuron*, 16(4):825–833.

Dajas-Bailador, F. A., Mogg, A. J., and Wonnacott, S. (2002). Intracellular ca2+ signals evoked by stimulation of nicotinic acetylcholine receptors in sh-sy5y cells: contribution of voltage-operated ca2+ channels and ca2+ stores. *Journal of Neurochemistry*, 81(3):606–14.

Dan, Y. and Poo, M.-M. (2004). Spike timing-dependent plasticity of neural circuits. *Neuron*, 44(1):23–30.

Dannenberg, H., Pabst, M., Braganza, O., Schoch, S., Niediek, J., Bayraktar, M., Mormann, F., and Beck, H. (2015). Synergy of direct and indirect cholinergic septo-hippocampal pathways coordinates firing in hippocampal networks. *Journal of Neuroscience*, 35(22):8394–8410.

Davies, C. H., Starkey, S. J., Pozza, M. F., and Collingridge, G. L. (1991). $gaba_b$ autoreceptors regulate the induction of ltp. *Nature*, 349(6310):609–611.

Davis, A., Gimenez, A., and Therrien, B. (2001). Effects of entorhinal cortex lesions on sensory integration and spatial learning. *Nursing Research*, 50(2):77–85.

Denham, M. and Borisyuk, R. (2000). A model of theta rhythm production in the septal-hippocampal system and its modulation by ascending brain stem pathways. *Hippocampus*, 10:698–716.

Destexhe, A., Mainen, Z. F., and Sejnowski, T. J. (1998). Kinetic models of synaptic transmission. In Koch, C. and Segev, I., editors, *Methods in neuronal modeling: from ions to networks*, chapter 1, pages 1–25. The MIT Press.

di Volo, M., Romagnoni, A., Capone, C., and Destexhe, A. (2019). Biologically realistic mean-field models of conductance-based networks of spiking neurons with adaptation. *Neural Computation*, 31(4):653–680.

Dickson, C., Magistretti, J., Shalinsky, M., E.Fransén, Hasselmo, M., and Alonso, A. (2000). Properties and role of i_h in the pacing of subthreshold oscillations in entorhinal cortex layer ii neurons. *Journal of Neurophysiology*, 83(5):2562–2579.

Dragoi, G. and Buzsaki, G. (2006). Temporal encoding of place sequences by hippocampal cell assemblies. *Neuron*, 50(1):145–157.

Dudek, S. and Bear, M. (1991). Homosynaptic long-term depression in area ca1 of hippocampus and effects of n-methyl-d-aspartate receptor blockade. *Proceedings of the National Academy of Sciences of the United States of America*, 89(10):4363–4367.

Dumont, G., Ermentrout, G. B., and Gutkin, B. (2017). Macroscopic phase-resetting curves for spiking neural networks. *Physical Review E*, 96(4):042311.

Dumont, G. and Gutkin, B. (2019). Macroscopic phase resetting-curves determine oscillatory coherence and signal transfer in inter-coupled neural circuits. *PLOS Computational Biology*, 15(5):e1007019.

Ermentrout, G. and Kopell, N. (1986). Parabolic bursting in an excitable system coupled with a slow oscillation. *SIAM Journal on Applied Mathematics*, 46(2):233–253.

Feng, T., Silva, D., and Foster, D. J. (2015). Dissociation between the experience-dependent development of hippocampal theta sequences and single-trial phase precession. *Journal of Neuroscience*, 35(12):4890–4902.

Ferguson, K. A., Chatzikalymniou, A. P., and Skinner, F. K. (2017). Combining theory, model and experiment to explain how intrinsic theta rhythms are generated in an in vitro whole hippocampus preparation without oscillatory inputs. *eNeuro*, 4(4).

Fernandez, F., Malerba, P., Bressloff, P., and White, J. (2013). Entorhinal stellate cells show preferred spike phase-locking to theta inputs that is enhanced by correlations in synaptic activity. *Journal of Neuroscience*, 33(14):6027–6040.

Foster, D. J. and Wilson, M. A. (2007). Hippocampal theta sequences. *Hippocampus*, 17(11):1093–1099.

Freund, T. and Buzsáki, G. (1996). Interneurons of the hippocampus. *Hippocampus*, 6:347–470.

Gerstner, W., Kempter, R., van Hemmen, J. L., and Wagner, H. (1996). A neuronal learning rule for sub-millisecond temporal coding. *Nature*, 383:76–78.

Giovannini, F., Knauer, B., Yoshida, M., and Buhry, L. (2017). The can-in network: A biologically inspired model for self-sustained theta oscillations and memory maintenance in the hippocampus. *Hippocampus*, 27(4):450–463.

Gogolák, G., Stumpf, C., Petsche, H., and Sterc, J. (1968). The firing pattern of septal neurons and the form of the hippocampal theta wave. *Brain Research*, 7(2):201–207.

Gonçalves, P., Luechmann, J.-M., Deistler, M., Nonnenmacher, M., Ocal, K., Bassetto, G., Chintaluri, C., Podlaski, W., Haddad, S., Vogels, T., Greenberg, D., and Macke, J. (2020). Training deep neural density estimators to identify mechanistic models of neural dynamics. *eLife*, 9:e56261.

Goutagny, R., Jackson, J., and Williams, S. (2009). Self-generated theta oscillations in the hippocampus. *Nature Neuroscience*, 12:1491–1493.

Gradinaru, V., Zhang, F., Ramakrishnan, C., Mattis, J., Prakash, R., Diester, I., Goshen, I., Thompson, K. R., and Deisseroth, K. (2010). Molecular and cellular approaches for diversifying and extending optogenetics. *Cell*, 141(1):154–165.

Graupner, M. and Brunel, N. (2005a). Stdp in a bistable synapse model based on camkii and associated signaling pathways. *PLoS Computational Biology*, (2007):e221.

Graupner, M. and Brunel, N. (2005b). Stdp in a bistable synapse model based on camkii and associated signaling pathways. *PLoS Computational Biology*, (2007):e221.

Graupner, M. and Brunel, N. (2012). Calcium-based plasticity model explains sensitivity of synaptic changes to spike pattern, rate, and dendritic location. *Proceedings of the National Academy of Sciences*, 109(10):3991–3996.

Graupner, M., Maex, R., and Gutkin, B. (2013). Endogenous cholinergic inputs and local circuit mechanisms govern the phasic mesolimbic dopamine response to nicotine. *PLoS Computational Biology*, 9(8):e1003183.

Green, J. and Arduini, A. (1954). Hippocampal electrical activity in arousal. *Journal of Neurophysiology*, 17(6):533–557.

Griffin, A. L., Asaka, Y., Darling, R. D., and Berry, S. (2004). Theta-contingent trial presentation accelerates learning rate and enhances hippocampal plasticity during trace eyeblink conditioning. *Behavioral Neuroscience*, 118(2):403–11.

Griguoli, M. and Cherubini, E. (2012). Regulation of hippocampal inhibitory circuits by nicotinic acetylcholine receptors: nachrs and inhibitory circuits in the hippocampus. *The Journal of Physiology*, 590(4):655–666.

Gu, Z., Alexander, G. M., Dudek, S., and Yakel, J. (2017). Hippocampus and entorhinal cortex recruit cholinergic and nmda receptors separately to generate hippocampal theta oscillations. *Cell Reports*, 21(12):3585–3595.

Gu, Z., Smith, K. G., Alexander, G. M., Guerreiro, I., Dudek, S. M., Gutkin, B., Jensen, P., and Yakel, J. L. (2020). Hippocampal interneuronal $\alpha 7$ nachrs modulate theta oscillations in freely moving mice. *Cell Reports*, 31(10):107740.

Gu, Z. and Yakel, J. L. (2011). Timing-dependent septal cholinergic induction of dynamic hippocampal synaptic plasticity. *Neuron*, 71(1):155–165.

Gu, Z. and Yakel, J. L. (2017). Inducing theta oscillations in the entorhinal hippocampal network in vitro. *Brain Structure and Function*, 222(2):943–955.

Guan, Z.-Z., Zhang, X., Ravid, R., and Nordberg, A. (2001). Decreased protein levels of nicotinic receptor subunits in the hippocampus and temporal cortex of patients with alzheimer's disease. *Journal of Neurochemistry*, 74(1):237–243.

Gupta, A., van der Meer, M. A., Touretzky, D., and Redish, A. (2012). Segmentation of spatial experience by hippocampal theta sequences. *Nature Neuroscience*, 15:1032–1039.

Haam, J. and Yakel, J. L. (2017). Cholinergic modulation of the hippocampal region and memory function. *Journal of Neurochemistry*, 142:111–121.

Hamam, B. N., Kennedy, T. E., Alonso, A., and Amaral, D. G. (2000). Morphological and electrophysiological characteristics of layer v neurons of the rat medial entorhinal cortex. *The Journal of Comparative Biology*, 418:457–472.

Hansel, D., Mato, G., and Meunier, C. (1995). Synchrony in excitatory neural networks. *Neural Computation*, 7(2):307–337.

Hebb, D. (1949). *The organization of behavior.* New York: Wiley.

Hinman, J., Dannenberg, H., Alexander, A., and Hasselmo, M. (2018). Neural mechanisms of navigation involving interactions of cortical and subcortical structures. *Journal of Neurophysiology*, 119(6):2007–2029.

Hodgkin, A. and Huxley, A. (1952). A quantitative description of membrane current and its application to conduction and excitation in nerve. *The Journal of Physiology*, 117(4):500–544.

Holmes, W. and Levy, W. (1990). Insights into associative long-term potentiation from computational models of nmda receptor-mediated calcium influx and intracellular calcium concentration changes. *Journal of Neurophysiology*, 63(5):1148–1168.

Hyman, J. M., Wyble, B. P., Goyal, V., Rossi, C. A., and Hasselmo, M. E. (2003). Stimulation in hippocampal region ca1 in behaving rats yields long-term potentiation when delivered to the peak of theta and long-term depression when delivered to the through. *Journal of Neuroscience*, 23(37):11725–31.

Inglebert, Y., Aljadeff, J., Brunel, N., and Debanne, D. (2020). Synaptic plasticity rules with physiological calcium levels. *Proceedings of the National Academy of Sciences of the United States of America.*

Izhikevich, E. (2003). Simple model of spiking neurons. *IEEE Transactions on Neural Networks*, 14(6):1569–1572.

Izhikevich, E. M. (2007a). Fast spiking (fs) interneurons. In Sejnowski, T. J. and Poggio, T., editors, *Dynamical Systems in Neuroscience*, chapter 8, page 298.

Izhikevich, E. M. (2007b). Hippocampal ca1 pyramidal neurons. In Sejnowski, T. J. and Poggio, T., editors, *Dynamical Systems in Neuroscience*, chapter 8, pages 308–310.

Izhikevich, E. M. (2007c). Regular spiking (rs) neurons. In Sejnowski, T. J. and Poggio, T., editors, *Dynamical Systems in Neuroscience*, chapter 8, pages 282–287.

Izhikevich, E. M. (2007d). Spiny projection neurons of neostriatum and basal ganglia. In Sejnowski, T. J. and Poggio, T., editors, *Dynamical Systems in Neuroscience*, chapter 8, pages 311–312.

Izhikevich, E. M. (2007e). Stellate cells of the entorhinal cortex. In Sejnowski, T. J. and Poggio, T., editors, *Dynamical Systems in Neuroscience*, chapter 8, pages 314–315.

Ji, D., Lape, R., and Dani, J. A. (2001). Timing and location of nicotinic activity enhances or depresses hippocampal synaptic plasticity. *Neuron*, 31(1):131–141.

Jinno, S. and Kosaka, T. (2010). Stereological estimation of numerical densities of glutamatergic principal neurons in the mouse hippocampus. *Hippocampus*, 20(7):829–840.

Kadar, T., Dachir, S., Shukitt-Hale, B., and Levy, A. (1998). Sub-regional hippocampal vulnerability in various animal models leading to cognitive dysfunction. *Journal of neural transmission*, 105:987–1004.

Kamondi, A., Acsády, L., Wang, X.-J., and Buzsáki, G. (1998). Theta oscillations in somata and dendrites of hippocampal pyramidal cells in vivo: activity-dependent phase-precession of action potentials. *Hippocampus*, 8(3):244–261.

Kempter, R., Gerstner, W., and van Hemmen, J. L. (1999). Hebbian learning and spiking neurons. *Physical Review E*, 59(4):4498.

King, C., Recce, M., and O'Keefe, J. (1998). The rhyhmicity of cells of the medial septum/diagonal band of broca in the awake freely moving rate: relationships with behaviour and hippocampal theta. *European Journal of Neuroscience*, 10(2):464–477.

Kispersky, T., Fernandez, F., Economo, M., and White, J. (2012). Spike resonance properties in hippocampal o-lm cells are dependent on refractory dynamics. *Journal of Neuroscience*, 32(11):3637–3651.

Klausberger, T. and Somogyi, P. (2008). Neuronal diversity and temporal dynamics: the unity of hippocampal circuit operations. *Science*, 321:53–57.

Klink, R. and Alonso, A. (1998). Morphological characteristics of layer ii projection neurons in the rat medial entorhinal cortex. *Hippocampus*, 7(5):571–583.

Knowles, W. and Schwartzkroin, P. (1981). Local circuit synaptic interactions in hippocampal brain slices. *Journal of Neuroscience*, 1(3):318–322.

Koenig, J., Linder, A., Leutgeb, J., and Leutgeb, S. (2011). The spatial periodicity of grid cells is not sustained during reduced theta oscillations. *Science*, 332(6029):592–595.

Konorski, J. (1948). *Conditioned reflexes and neuron organization.* Cambridge, UK: Hefner.

Kopell, N., Borgers, C., Pervouchine, D., Malerba, P., and Tort, A. (2010). Gamma and theta rhythms in biophysical models of hippocampal circuits. In Cutsuridis, V., Graham, B., Cobb, S., and Vida, I., editors, *Hippocampal Microcircuits*, pages 423–457.

Korotkova, T., Fuchs, E., Ponomarenko, A., von Engelhardt, J., and Monyer, H. (2010). Nmda receptor ablation on parvalbumin-positive interneurons impairs hippocampal synchrony, spatial representations, and working memory. *Neuron*, 68(3):557–569.

Kramis, R., Vanderwolf, C., and Bland, B. (1975). Two types of hippocampal rhythmical slow activity in both the rabitt and the rat: relations to behavior and effects of atropine diethyl ether, urethane, and pentobarbital. *Experimental Neurology*, 49(1):58–85.

Kullmann, D. (1994). Amplitude fluctuations of dual-component epscs in hippocampal pyramidal cells: implications for long-term potentiation. *Neuron*, 12:1111–1120.

Landfield, P. W., McGaugh, J. L., and Tusa, R. J. (1972). Theta rhythm: a temporal correlate of memory storage processes in the rat. *Science*, 175(4017):87–9.

Lanzafame, A., Christopoulos, A., and Mitchelson, F. (2003). Cellular signaling mechanisms for muscarinic acetylcholine receptors. *Receptors Channels*, 9:241–260.

Larson, J., Wong, D., and Lynch, G. (1986). Patterned stimulation at the theta frequency is optimal for the induction of hippocampal long-term potentiation. *Brain Research*, 368(2):347–50.

Lee, M., Chrobak, J., Sik, A., Wiley, R., and Buzsáki, G. (1994). Hippocampal theta activity following selective lesion of the septal cholinergic system. *Neuroscience*, 62(4):1033–1047.

Leuckmann, J.-M., Gonçalves, P., Bassetto, G., Ocal, K., Nonnenmacjer, M., and Macke, J. (2017). Flexible statistical inference for mechanistic models of neural dynamics. *Advances in Neural Information Processing Systems*, pages 1289–1299.

Leung, L. and Shen, B. (2004). Glutamatergic synaptic transmission participates in generating the hippocampal eeg. *Hippocampus*, 14(4):510–525.

Leung, L.-W. S. and Desborough, K. A. (1988). Apv, an n-methyl-d-aspartate receptor antagonist, blocks the hippocampal theta rhythm in behaving rats. *Brain Research*, 463(1):148–152.

Levin, E. D. (2002). Nicotinic receptor subtypes and cognitive function. *Journal of Neurobiology*, 53(4):633–640.

Li, X.-G., Somogyi, P., Ylinen, A., and Buzsáki, G. (1994). The hippocampal ca3 network: and in vivo intracellular labelin study. *The Journal of Comparative Neurology*, 339:181–208.

Lisman, J. (1989). A mechanism for the hebb and the anti-hebb processes underlying learning and memory. *Proceedings of the National Academy of Sciences*, 86:9674–9578.

Lisman, J. and Zhabotinsky, A. (2001). A model of synaptic memory: a camkii/pp1 switch that potentiates transmission by organizing an ampa receptor anchoring assembly. *Neuron*, 31(2):191–201.

López-Madrona, V. and Canals, S. (2021). Functional interactions between entorhinal cortical pathways modulate theta activity in the hippocampus. *Biology*, 10:692.

Lüscher, C. and Malenka, R. (2012). Nmda receptor-dependent long-term potentiation and long-term depression (ltp/ltd). *Cold Spring Harbor Perspectives in Biology*, 4(6):a005710–a005710.

Maccaferru, G., David, J., Roberts, B., Szucs, P., Cottingham, C. A., and Somogyi, P. (2000). Cell surface domain specific postsynaptic currents evoked by identified gabaergic neurones in rat hippocampus *in vitro*. *The Journal of Physiology*, 524(1):91–116.

Mainen, Z. F., Jia, Z., Roder, J., and Malinow, R. (1998). Use-dependent ampa receptor block in mice lacking glur2 suggests postsynaptic site for ltp expression. *Nature Neuroscience*, 1:579–586.

Maki-Marttunen, T., Iannella, N., Edwards, A. G., Einevoll, G. T., and Blackwell, K. T. (2020). A unified computational model for cortical post-synaptic plasticity. *eLife*, 9:e55714.

Markram, H. and Segal, M. (1992). The inositol 1,4,5-trisphosphate pathway mediates cholinergic potentiation of rat hippocampal neuronal responses to nmda. *Journal of Physiology*, 447:513–533.

Marr, D. (1971). Simple memory: a theory for archicortex. *Philosophical transactions of the Royal Society of London. Series B, Biological Sciences*, 262(841):23–81.

McNaughton, B. L. and Morris, R. (1987). Hippocampal synaptic enhancement and information storage within a distributed memory system. *Trends in Neuroscience*, 10(10):408–415.

Meredith, R. M., Floyer-Lea, A., and Paulsen, O. (2003). Maturation of long-term potentiation induction rules in rodent hippocampus: Role of gabaergic inhibition. *The Journal of Neuroscience*, 23(35):11142–11146.

Mikulovic, S., Restrepo, C. E., Siwani, S., Bauer, P., Pupe, S., Tort, A. B., Kullander, K., and Leão, R. N. (2018). Ventral hippocampal olm cells control type 2 theta oscillations and response to predator odor. *Nature Communications*, 9(1):3638.

Mitchell, A. and Ranck Jr., J. (1980). Generation of theta rhythm in medial entorhinal cortex of freely moving rats. *Brain Research*, 189(1):49–66.

Mizumori, S. J., Perez, G. M., Alvarado, M. C., Barnes, C. A., and McNaughton, B. L. (1990). Reversible inactivation of the medial septum differentially affects two forms of learning in rats. *Brain Research*, 528(1):12–20.

Montbrió, R., Pazó, D., and Roxin, A. (2015). Macroscopic description for networks of spiking neurons. *Physical Review X*, 5(2):021028.

Montoya, C. and Sainsbury, R. (1985). The effects of entorhinal cortex lesions on type 1 and type 2 theta. *Physiology and Behavior*, 35(1):121–126.

Moser, E. I., Kropff, E., and Moser, M.-B. (2008). Place cells, grid cells, and the brain's spatial representation system. *Annual Review of Neuroscience*, 31:69–89.

Muller, D., Arai, A., and Lynch, G. (1992). Factors governing the potentiation of nmda receptor-mediated responses in hippocampus. *Hippocampus*, 2(1):29–38.

Müller, C. and Remy, S. (2014). Dendritic inhibition mediated by o-lm and bistratified interneurons in the hippocampus. *Frontiers in Synaptic Neuroscience*, 6.

Neru, A. and Assisi, C. (2021). Theta oscillations gate the transmission of reliable sequences in the medial entorhinal cortex. *eNeuro*, 8(3):18.

Nicola, W. and Campbell, S. A. (2013). Bifurcations of large networks of two-dimensional integrate and fire neurons. *Journal of Computational Neuroscience*, 35(1):87–108.

Nuñez, A. and Buño, W. (2021). The theta rhythm of the hippocampus: from neuronal and circuit mechanisms to behavior. *Frontiers in Cellular Neuroscience*, 15:31.

Ohara, S., Onodera, M., Simonsen, O., Yoshino, R., Hioki, H., Iijima, R., Tsutsui, K.-I., and Witter, M. (2018). Intrinsic projections of layer vb neurons to layers va, iii, and ii in the lateral and medial entorhinal cortex of the rat. *Cell Reports*, 24(1):107–116.

Ormond, J. and Woodin, M. A. (2009). Disinhibition mediates a form of hippocampal long-term potentiation in area ca1. *PLoS ONE*, 4(9):e7224.

Orr, G., Rao, G., Houston, F., McNaughton, B., and Barnes, C. (2001). Hippocampal synaptic plasticity is modulated by theta rhythm in the fascia dentata of adult and aged freely behaving rats. *Hippocampus*, 11(6):647–654.

Ott, E. and Antonsen, T. M. (2008). Low dimensional behavior of large systems of globally coupled oscillators. *Chaos*, 18:037113.

Pastoll, H., Solanka, L., van Rossum, M., and Nolan, M. F. (2012). Feedback inhibition enables theta-nested gamma oscillations and grid firing fields. *Neuron*, 77:141–154.

Pedrosa, V. and Clopath, C. (2017). The role of neuromodulators in cortical plasticity. a computational perspective. *Frontiers in Synaptic Neuroscience*, 8:38.

Pelkey, K. A., Chittajallu, R., Craig, M. T., Tricoire, L., Wester, J. C., and McBain, C. J. (2017). Hippocampal gabaergic inhibitory interneurons. *Physiological Reviews*, 97(4):1619–1747.

Perkel, D. J., Petrozzino, J. J., Nicoll, R. A., and Connor, J. A. (1993). The role of ca^{2+} entry via synaptically activated nmda receptors in the induction of long-term potentiation. *Neuron*, 11:817–823.

Petsche, H., Stumpf, C., and Gogolak, G. (1962). The significance of the rabbit's septum as a relay station between the midbrain and the hippocampus i. the control of hippocampus arousal activity by the septum cells. *Electroencephalograohy and Clinical Neurophysiology*, 14(2):202–211.

Radcliffe, K. A. and Dani, J. A. (1998). Nicotinic stimulation produces multiple forms of increased glutamatergic synaptic transmission. *Journal of Neuroscience*, 18(18):7075–7083.

Raiteri, M., Leardi, R., and Marchi, M. (1984). Heterogeneity of presynaptic muscarinic receptors regulating neurotransmitter release in the rat brain. *Journal of Pharmacology and Experimental Therapeutics*, 228(1):209–214.

Rathouz, M., Vijayaraghavan, S., and Berg, D. (1996). Elevation of intracellular calcium levels in neurons by nicotinic acetylcholine receptors. *Molecular Neurobiology*, 12(2):117–31.

Riedel, G., Micheau, J., Lam, A., Roloff, E., Martin, S., Bridge, H., de Hoz, L., Poeschel, B., McCulloch, J., and Morris, R. (1999). Reversible neural inactivation reveals hippocampal participation in several memory processes. *Nature Neuroscience*, 2:898–905.

Rinzel, J. (1985). Bursting oscillations in an excitable membrane model. In *Ordinary and partial differential equations: Proceedings of the 8th Dundee Conference*, pages 304–316. Springer.

R.Leão, S.Mikulovic, K.Leão, H.Munguba, H.Gezeluis, A.Enjin, K.Patra, A.Eriksson, L.Loew, A.Tort, and K.Kullander (2012). Olm interneurons differentially modulate ca3 and entorhinal inputs to hippocampal ca1 neurons. *Nature Neuroscience*, 15(11):1524–1530.

Rotstein, H., Oppermann, T., White, J., and Kopell, N. (2005a). The dynamics structure underlying subthreshold oscillatory activity and the onset of spikes in a model of medial entorhinal cortex stellate cells. *Journal of Computational Neuroscience*, 21(3):271–292.

Rotstein, H. G., Pervouchine, D. D., Acker, C. D., Gillies, M. J., White, J. A., Buhl, E. H., Whittington, M. A., and Kopell, N. (2005b). Slow and fast inhibition and an h-current interact to create a theta rhythm in a model of ca1 interneuron network. *Journal of Neurophysiology*, 94(2):1509–1518.

Rowland, D. C., Obenhaus, H. A., Skytøen, E. R., Zhang, Q., Kentros, C. G., Moser, E., and Moser, M.-B. (2018). Functional properties of stellate cells in medial entorhinal cortex layer ii. *eLife*, 7:e36664.

Ruiz, A., Campanac, E., Scott, R. S., Rusakov, S. A., and Kullmann, D. M. (2010). Presynaptic gaba a receptors enhance transmission and ltp induction at hippocampal mossy fiber synapses. *Nature Neuroscience*, 13(4):432–438.

Sabatini, B., Oertner, T. G., and Svoboda, K. (2002). The life of cycle of ca^{2+} ions in dendritic spines. *Neuron*, 33(3):439–452.

Saudargiene, A. and Graham, B. (2015). Inhibitory control of site-specific synaptic plasticity in a model ca1 pyramidal neuron. *Biosystems*, 130:37–50.

Schmid, L. C., Mittag, M., Poll, S., Steffen, J., Wagner, J., Geis, H.-R., Schwarz, I., Schmidt, B., Schwarz, M. K., Remy, S., and Fuhrmann, M. (2016). Dysfunction of somatostatin-positive interneurons associated with memory deficits in an alzheimer's disease model. *Neuron*, 92(1):114–125.

Schulz, J. M., Knoflach, F., Hernandez, M.-C., and Bischofberger, J. (2018). Dendrite-targeting interneurons control synaptic nmda-receptor activation via nonlinear α5-gabaa receptors. *Nature Communications*, 9(1):3576.

Sharma, G. and Vijayaraghavan, S. (2001). Nicotinic cholinergic signaling in hippocampal astrocytes involves calcium-induced calcium release from intracellular stores. *Proceedings of the National Academy of Sciences of the United States of America*, 98(7):4148–4153.

Sharma, G. and Vijayaraghavan, S. (2003). Modulation of presynaptic store calcium induces release of glutamate and postsynaptic firing. *Neuron*, 38(6):929–939.

Shoop, R. D., Chang, K. T., Ellisman, M. H., and Berg, D. K. (2001). Synaptically driven calcium transients via nicotinic receptors on somatic spines. *Journal of Neuroscience*, 21(3):771–781.

Shouval, H. Z., Bear, M. F., and Cooper, L. N. (2002). A unified model of nmda receptor-dependent bidirectional synaptic plasticity. *Proceedings of the National Academy of Sciences*, 99(16):10831–10836.

Skaggs, W. E., McNaughton, B. L., Wilson, M. A., and Barnes, C. A. (1996). Theta phase precession in hippocampal neuronal populations and the compression of temporal sequences. *Hippocampus*, 6(2):149–172.

Stewart, M. and Fox, S. (1990). Do septal neurons pace the hippocampal theta rhythm? *Trends in Neuroscience*, 13(5):163–169.

Stiefel, K. M. and Ermentrout, G. B. (2016). Neurons as oscillators. *Journal of Neurophysiology*, 116(6):2950–2960.

Surmeli, G., Marcu, D., McClure, C., Garden, D., Pastoll, H., and Nolan, M. (2015). Molecularly defined circuitry reveals input-output segregation in deep layers of the medial entorhinal cortex. *Neuron*, 88:1040–1053.

Tamamaki, N. and Nojyo, Y. (1993). Projection of the entorhinal layer ii neurons in the rat as revealed by intracellular pressure-injection of neurobiotin. *Hippocampus*, 3(4):471–480.

Tang, Q., Burgalossi, A., Ebbesen, C. L., Ray, S., Naumann, R., Schmidt, H., Spicher, D., and Brecht, M. (2014). Pyramidal and stellate cells specificity of grid and border representations in layer 2 of medial entorhinal cortex. *Neuron*, 84(6):1191–1197.

Treves, A. and Rolls, E. T. (1991). What determines the capacity of autoassociative memories in the brain? *Network: Computation in Neural Systems*, 2(4):371–397.

Tsien, J. Z., Huerta, P. T., and Tonegawa, S. (1996). The essential role of hippocampal ca1 nmda receptor-dependent synaptic plasticity in spatial memory. *Cell*, 87(7):1327–1338.

Tsuneki, H., Klink, R., Léna, C., Korn, H., and Changeux, J. (2000). Calcium mobilization elicited by two types of nicotinic acetylcholine receptors in mouse substantia nigra pars compacta. *Euro J. Neuroscience*, 12(7):2475–85.

Valentino, R. and Dingledine, R. (1981). Presynaptic inhibitory effect of acetylcholine in the hippocampus. *Journal of Neuroscience*, 1(7):784–792.

Vandecasteele, M., Varga, V., Berényi, A., Papp, E., Barthó, P., Venance, L., Freund, T. F., and Buzsáki, G. (2014). Optogenetic activation of septal cholinergic neurons suppresses sharp wave ripples and enhances theta oscillations in the hippocampus. *Proceedings of the National Academy of Sciences*, 111(37):13535–13540.

Vanderwolf, C. and Baker, G. (1986). Evidence that serotonin mediates non-cholinergic neocortical low voltage fast activity, non-cholinergic hippocampal rhythmical slow activity and contributes to intelligent behavior. *Brain Research*, 374(2):342–356.

Vernino, S., Amador, M., Luetje, C., Patrick, J., and Dani, J. (1992). Calcium modulation and high calcium permeability of neuronal nicotinic acetylcholine receptors. *Neuron*, 8:127–134.

Vernino, S., Rogers, M., Radcliffe, K. A., and Dani, J. A. (1994). Quantitative measurement of calcium flux through muscle and neuronal nicotinic acetylcholine receptors. *The Journal of Neuroscience*, 14(9):5514–5524.

Volpicelli, L. and Levey, A. (2004). Muscarinic acetylcholine receptor subtypes in cerebral cortex and hippocampus. *Progress in Brain Research*, 145:59–66.

Wanaverbecq, N., Semyanov, A., Pavlov, I., Walker, M. C., and Kullmann, D. M. (2007). Cholinergic axons modulate gabaergic signaling among hippocampal interneurons via postsynaptic $\alpha 7$ nicotinic receptors. *Journal of Neuroscience*, 27(21):5683–5693.

Wang, H.-Y., Lee, D. H., D'Andrea, M. R., Peterson, P. A., Shank, R. P., and Reitz, A. B. (2000). β-amyloid$_{1-42}$ binds to $\alpha 7$ nicotinic acetylcholine receptor with high affinity-implications for alzheimer's disease pathology. *Journal of Biological Chemistry*, 275(8):5626–5632.

Wang, X.-J. (2002). Pacemaker neurons for the theta rhythm and their synchronization in the septohippocampal reciprocal loop. *Journal of Neurophysiology*, 87(2):889–900.

Wang, Y., Romani, S., Lustig, B., Leonardo, A., and Pastalkova, E. (2015). Theta sequences are essential for internally generated hippocampal firing fields. *Nature Neuroscience*, 18:282–288.

White, J., Banks, M., Pearce, R., and Kopell, N. (2000). Networks of interneurons with fast and slow γ-aminobutyric acid type a ($gaba_a$) kinetics provide substrate for mixed γ-θ rhythm. *Proceedings of the National Academy of Sciences of the United States of America*, 97:8128–33.

Wigström, H. and Gustafsson, B. (1983). Facilitated induction of hippocampal long-lasting potentiation during blockade of inhibition. *Nature*, 301:603–604.

Winson, J. (1978). Loss of hippocampal theta rhythm results in spatial memory deficit in rat. *Science*, 201(4351):160–163.

Winterer, J., Maier, N., Wozny, C., Beed, P., Breustedt, J., Peng, R. E. Y., D'Albis, T., Kempter, R., and Schmitz, D. (2017). Excitatory microcircuits within superficial layers of the medial entorhinal cortex. *Cell Reports*, 19(6):1110–1116.

Witten, I., Lin, S.-C., Bordsky, M., Prakash, R., Diester, I., Anikeeva, P., Gradinaru, V., Ramakrishnan, C., and Deisseroth, K. (2010). Cholinergic interneurons control local circuit activity and cocaine conditioning. *Science*, 330(6011):1677–1681.

Witter, M. P., Doan, T. P., Jacobsen, B., Nilssen, E. S., and Ohara, S. (2017). Architecture of the entorhinal cortex a review of entorhinal anatomy in rodents with some comparative notes. *Frontiers in Systems Neuroscience*, 11:12.

Yakel, J. L. (2012). Nicotinic ach receptors in the hippocampus: Role in excitability and plasticity. *Nicotine & Tobacco Research*, 14(11):1249–1257.

Yang, G. R., Murray, J. D., and Wang, X.-J. (2016). A dendritic disinhibitory circuit mechanism for pathway-specific gating. *Nature Communications*, 7(1):12815.

Yoder, R. and Pang, K. (2005). Involvement of gabaergic and cholinergic medial septal neurons in hippocampal theta rhythm. *Hippocampus*, 15(3):381–392.

Young, G. W. D. and Keizer, J. (1992). A single-pool inositol 1,4,5-trisphosphate-receptor-based model for agonist-stimulated oscillations in ca2+ concentration. *Proceedings of the National Academy of Sciences*, 89(20):9895–9899.

Zemankovics, R., Káli, S., Paulsen, O., Freund, T. F., and Hájos, N. (2010). Differences in subthreshold resonance of hippocampal pyramidal cells and interneurons: the role of h-current and passive membrane charactheristics. *Journal of Physiology*, 588(12):2109–2132.

RÉSUMÉ

Les oscillations thêta sont un rythme proéminent de 4 à 12 Hz observé dans l'hippocampe et ses structures associées chez tous les mammifères. Outre l'hippocampe, deux autres structures du cerveau sont reconnues comme essentielles à la génération *in vivo* du rythme thêta de l'hippocampe - le septum médian (MS) et le cortex entorhinal (EC). Cependant, après plusieurs décennies de recherche, les mécanismes produisant ces oscillations restent mal connus.
Dans cette thèse, on étudiera le rôle que les trois régions du cerveau citées précédemment (MS, EC et l'hippocampe) jouent dans la génération et l'entretien des oscillations thêta. Dans la première partie de cette thèse, on étudiera comment les entrées septales cholinergiques, en agissant sur les neurones hippocampaux GABAergique, contrôlent l'excitabilité et la plasticité de l'hippocampe. Dans la seconde partie, on analysera les mécanismes du circuit qui permettent la génération du rythme thêta dans le EC et la propagation de l'activité oscillatoire jusqu'à l'hippocampe. A cette fin, on commencera par étudier comment la connectivité du réseau du cortex enthorhinal, fait de cellules stellaires, de cellules pyramidales et d'interneurones à dynamique rapide, module la réponse du circuit vers les entrées excitatrices de l'hippocampe. Ensuite, on examinera comment les entrées oscillatoires enthorhinales vers un réseau de cellules OLM, d'interneurones à dynamique rapide et de cellules pyramidales, peuvent conduire le système dans un état de résonnance thêta. En résumé, on proposera un mécanisme multi-circuit pour la génération des oscillations thêta dans un réseau septal-hippocampal-entorhinal, dans lequel trois régions du cerveau jouent une rôle actif dans la production et l'expression du rythme thêta. Les entrées cholinergiques contrôlent l'excitabilité hippocampale, ce qui permet la generation des oscillations thêta dans le circuit du EC et leur propagation dans l'hippocampe, et ferme ainsi la boucle enthorhinale-hippocampale.

MOTS CLÉS

rythmes thêta; hippocampe; récepteurs cholinergiques

ABSTRACT

Hippocampal theta oscillations are a prominent 4-12 Hz rhythm observed in the hippocampal local field potential and its associated structures of all mammals. Besides the hippocampus, two other brain structures are known to be essential for *in vivo* hippocampal theta generation - the medial septum (MS) and entorhinal cortex (EC). However, after decades of research, the mechanisms through which these oscillations arise remain elusive.
In this thesis, we address the role that each of the three mentioned brain regions (MS, EC and hippocampus) play in the generation and maintenance of theta oscillations. In the first part of the dissertation, we study how septal cholinergic inputs acting on hippocampal GABAergic interneurons through $\alpha 7$ nicotinic receptors regulate the excitability and plasticity of the hippocampus. In the second part, we investigate the circuit mechanisms that enable the generation of theta oscillations in the EC and the propagation of the rhythmic activity to the hippocampus. To this aim, we start by studying how the connectivity of the entorhinal cortex network made of stellate cells, pyramidal cells and fast-spiking interneurons modulates the circuit's response to hippocampal excitatory inputs. Next, we address how entorhinal oscillatory inputs onto an hippocampal network of OLM cells, fast-spiking interneurons and pyramidal cells can drive the system into a theta resonant state.
In summary, we propose a multi-circuit mechanism for the generation of theta oscillations in a septal-hippocampal-entorhinal network, where the three brain regions play an active role in the induction and expression of the theta rhythm. Cholinergic inputs regulate hippocampal excitability, which acts as a gate that permits theta oscillations to arise in the EC circuit and spread to the hippocampus, thus closing the entorhinal-hippocampal loop.

KEYWORDS

theta-rhythm; hippocampus; cholinergic receptors